Process Optimization, Numerical Modelling, and Microstructure Control in Laser Powder Bed Fusion of Ti-5553 Parts

by

Mahyar Hasanabadi

A thesis
presented to the University of Waterloo
in fulfillment of the
thesis requirement for the degree of
Doctor of Philosophy
in
Mechanical and Mechatronics Engineering

Waterloo, Ontario, Canada, 2024

Examining Committee Membership

The following served on the Examining Committee for this thesis. The decision of the Examining Committee is by majority vote.

External Examiner	JAVAD MOSTAGHIMI, Ph.D. Professor, University of Toronto
Supervisor	EHSAN TOYSERKANI, Ph.D. Professor, University of Waterloo
Supervisor	ADRIAN GERLICH, Ph.D. Professor, University of Waterloo
Internal Member	HAMID JAHED, Ph.D. Professor, University of Waterloo
Internal Member	MUSTAFA YAVUZ, Ph.D. Professor, University of Waterloo
Internal-External Member	MICHAEL POPE, Ph.D. Professor, University of Waterloo

Author’s Declaration

This thesis consists of material all of which I authored or co-authored: see Statement of Contributions included in this thesis. This is a true copy of the thesis, including any required final revisions, as accepted by the examiners.

I understand that my thesis may be made electronically available to the public.

Statement of contributions

I would like to acknowledge my co-authors who contributed to the research described in this thesis:

Prof. Ehsan Toyserkani: Supervision the research, providing the original idea for the current thesis, editing and reviewing papers, providing experimental facilities, and providing funding.

Prof. Adrian Gerlich: Supervising the research, providing the original idea for the current thesis in the area of material characterization, editing and reviewing papers.

Dr. Ali Keshavarzkermani: Providing editorial feedback in the preparation of the individual manuscripts in Chapters 3 – 6 and technical training for carrying out the materials characterization.

Prof. Hamed Asgari: Providing editorial feedback in the preparation of the manuscript in Chapters 3,4 and 6 and technical training for carrying out the materials characterization.

Dr. Shahriar Imani Shahabad: Providing editorial feedback in the preparation of the manuscript in Chapter 5 and software training for carrying out the numerical modelling.

Ms. Nadia Azizi: Providing editorial feedback in the preparation of the individual manuscripts in Chapters 3,4, and 6.

Mr. Francis Dibia and Mr. Roger Eybel: Providing the support needed in the optimization of LPBF process for Ti-5553.

Abstract

Additive manufacturing (AM) is an advanced production technique that creates components by depositing material layer by layer. AM has been deployed industrially for producing metallic parts from alloys which pose challenges in traditional manufacturing processes like titanium alloys (Ti-alloys). While Ti-alloys are widely utilized across industries due to their exceptional strength-to-weight ratio, corrosion resistance, and toughness, machining titanium products is a complex endeavour. Laser Powder Bed Fusion (LPBF) as a metallic AM method presents an optimal solution. LPBF has been recognized as an appealing fabrication process for producing metallic parts with customized properties, however, obtaining these properties is quite challenging due to the interaction of several independent parameters. The properties of an LPBF-made product are highly dependent on the process parameters, which directly impact the melting and solidification of the molten metal. Hence, an in-depth investigation into the effect of process parameters on the melting and solidification conditions is necessary for manufacturing a high-quality product with tailored properties.

The current research deals with LPBF of a recently developed Ti-alloy, Ti-5Al-5V-5Mo-5Cr (Ti-5553). Among Ti-alloys, the β-metastable Ti-5553 offers a wide processing window, good hardenability, and excellent heat treatability, making it a preferred material in the aircraft industry. To generate an LPBF process map for Ti-5553 and assess the influence of process parameters on the properties of printed parts, an integrated single-track to multi-layer method was systematically employed. An investigation into the track morphology, melt pool geometry and melt pool microstructure composted of single-tracks was compared with a range of microscopic examinations and X-ray computed tomography measurements to multi-layer tracks to create a reliable process map. Following that, additional investigations were conducted on properties like mechanical performance and surface roughness, providing the manufacturer with additional information from each set of process parameters in order guide selection of processing parameters.

Since some aspects of solidification, such as temperature gradient and solidification rate, are not easily measurable experimentally, numerical modelling can provide an efficient solution for studying the correlation between the process parameters and the geometrical and thermal conditions of the LPBF-made melt pool. Hence, a numerical heat transfer modelling with a novel

hybrid volumetric heat source has been proposed to simulate the LPBF of Ti-5553 alloy for the first time. The developed hybrid model, with an incredibly low modelling error, can predict melt pool geometry and thermal variables, at different locations and time steps during melt pool solidification to estimate many important aspects of the microstructure formation such as grain morphology, subgrain size, and grain growth direction.

The gained knowledge from the experimental and numerical analyses of melt pool solidification under various process conditions is used to propose the "laser post-exposure treatment" as an innovative method for in-situ microstructure control during the LPBF process. The laser post-exposure (PE) treatment is a secondary laser scanning with significantly lower energy input, conducted after the completion of the main laser scanning strategy on the loose powder and before spreading the new layer of powder. This in-situ microstructure control treatment results in the development of uniform, uninterrupted, and elongated grains. A printed part utilizing post-exposure can be comparable to directionally solidified products used widely in industries for enhanced creep and fatigue resistance. It should be noted that this work is the first scientific attempt to control the grain structure via in-situ laser post-exposure.

Acknowledgements

The accomplishment of this research would not have been achievable without the assistance and support of numerous individuals, to whom I extend my sincere gratitude.

Foremost, I extend my profound appreciation to my supervisor, Prof. Ehsan Toyserkani, for his invaluable guidance, unwavering support, and patience throughout the completion of my graduate studies at the University of Waterloo. In the same vein, I extend my heartfelt appreciation to Prof. Adrian Gerlich, my co-supervisor, for his priceless guidance, encompassing friendship, and consistent assistance during this challenging journey.

I express my gratitude to my teammates in the Safran landing gear project, Prof. Hamed Asgari, Dr. Nivas Ramachandiran, Mr. Francis Dibia, and our amiable industrial partner, Mr. Roger Eybel, for their support and advice.

I would like to thank Dr. Ali Keshavarzkermani for his support and guidance on my research project. Moreover, I appreciate Dr. Shahriar Imani Shahabad for providing valuable support on LPBF modelling.

In addition, my heartfelt appreciation goes to the MSAM members who have been friendly supporters in every aspect of my studies and life, Dr. Reza Esmaeilizadeh, Ms. Nidia Azizi, Mr. Hamidreza Aghajani, Dr. Tatevik Minasyan, Dr. Esmaeil Sadeghi, Dr. Paria Karmi, Dr. Saeed Maleksaeedi, Dr. Ehsan Marzbanrad and Dr. Mazyar Ansari.

I acknowledge the support from Henry Ma, Jerry Ratthapakdee and Karl Rautenberg for helping with the tests and printing of LPBF parts.

Furthermore, I would like to acknowledge the support of the Natural Sciences and Engineering Research Council of Canada (NSERC), the Federal Economic Development Agency for Southern Ontario (FedDev Ontario), and the Safran Landing System.

Lastly, and of utmost significance, I extend my gratitude to my beloved wife and dear parents and brother, for their endless support and encouragement. I would not be in this position without their love…

Dedication

To my adored parents, who instilled in me the essence of LOVE;

to my wife, my life, who unveiled the power of LOVE;

and to my dear son, who has shown me the profound sweetness of LOVE…

Table of contents

List of Figures

List of Tables

List of Symbols

P	Laser power [W]
v	Scanning speed [mm/s]
l	Layer thickness [μm]
d	Laser spot diameter [μm]
M_a	Marangoni number
$\Delta\gamma$	Difference in surface tension within the Marangoni flow [N.m]
L	Length of the free surface [m]
μ_d	Dynamic viscosity [Pa.s]
D_c	Diffusion constant
$\boldsymbol{\sigma}_1$	Reference (initial) strength [MPa]
σ_Y	Yield stress [MPa]
E	Young's modulus [GPa]
D	Average grain size [mm]
K	Strengthening coefficient [MPa.mm$^{-1/2}$]
Q (x,y,z,t)	Internal heat generation per unit volume [W/m^3]
C_p	Specific heat [J/kg.K]
T	Temperature [K]
k	Thermal conductivity [W/m.K]
r_1	The lower radius of the heat source [μm]
q_c	Convective heat dissipation [W/m^2]
σ_{sb}	Stefan-Boltzmann coefficient [W/m^2.K^4]
λ	Thermal conductivity enhancement factors
h_c	Convection heat transfer coefficient [W/m^2.K]
H	Heat source height [μm]
q_0	The highest amount of heat intensity [W/m^3]
ε	Emissivity coefficient
r_0	The upper radius of the heat source [μm]
α	Absorption coefficient

L	Latent heat [J/Kg]
T_m	Melting temperature [K]
q_r	Radiative heat dissipation [W/m^2]
ρ	Density [Kg/m^3]
φ	The porosity of the powder bed
E_D	Deposited energy density
$D\tau$	Thermal diffusivity [m^2.s^{-1}],
σ	Laser spot size [m]
$\dot{T}$	Cooling rate [K/s]
G	Temperature gradient [K/m]
R	Solidification rate [m/s]
λ_1	Primary dendritic arm spacing (PDAS) [μm]
I_0	Maximum beam intensity [W/m^3]
r_b	Radius of the laser beam [μm]

Chapter 1

1 Introduction

1.1 Overview and motivations

Additive Manufacturing (AM), as an advanced fabrication technique, which has begun to be utilized for producing metallic components, and holds great promise for the fabrication of titanium alloys (Ti-alloys) which pose challenges for traditional manufacturing methods [1–3]. While Ti-alloys are highly valued in various industries for their impressive strength-to-weight ratio, excellent corrosion resistance, and toughness, the machining operation of Ti products can be quite challenging [4–6]. AM, by offering near-net-shape manufacturing, emerges as a promising solution for addressing this matter. Moreover, AM has enabled the fabrication of metallic parts with tailored properties [7,8]. Laser Powder Bed Fusion (LPBF) is one of the metallic AM methods, regarded as a feasible, versatile, and well-developed technique for fabricating products with custom properties [9,10]. This process involves several parameters that impact the properties of the final product. The process parameters affect the structure and microstructure of the LPBF-made parts and, consequently, their mechanical behaviour [11,12]. Therefore, avoiding possible defects and achieving the wanted microstructure and properties necessitates finding the optimized process parameters for the specific material [13,14].

In recent years, research has been done on the optimization of the LPBF process for various materials. However, there are still several unknown issues to be studied, especially for the LPBF of recently developed alloys, like Ti-5Al-5V-5Mo-5Cr (Ti-5553). As Ti-5553 is a β-metastable Ti-alloy with a two-phase microstructure (β and α phases), it offers excellent heat treatability and a wide range of mechanical properties are possible for this alloy [15,16]. A minor change in the solidification condition of molten Ti-5553 leads to a noticeable difference in its microstructure and mechanical behaviour [17,18]. Hence, alongside the identification of a reliable process window, it is crucial to have a deep understanding of how each process parameter affects the melting/solidification procedure and microstructure formation. This knowledge aids manufacturers in making more precise choices and solutions for tailored manufacturing. It should be noted that the sample fabrication in process optimization with the trial-and-error approach or

even statistical method can be costly in terms of time, money, and materials. Therefore, an effective optimization approach with minimum sample fabrication that can provide comprehensive results would be invaluable.

Since some aspects of solidification, such as temperature gradient and solidification rate, are not easily measurable experimentally, numerical modelling could be one of the most efficient ways to gain insights into the effects of process parameters on the elusive thermal variables of solidification [19–21]. Therefore, as there is no published modelling for LPBF-made Ti-5553, the development of a numerical model for LPBF of Ti-5553 is necessary. In addition to the thermal analysis, the melt pool geometry prediction is the other valuable product of the modelling. The melt pool size estimation can be used to mitigate defects like lack-of-fusion, without the need for time-consuming and expensive experimental tests [22]. It should be mentioned that various complex multi-physics phenomena engage in LPBF, including heat transfer, multi-phase transitions, Marangoni's flow, and recoil pressure. Considering all these complex physics drastically increases the computational time [23,24]. Hence, a dependable, efficient, and accurate model based on the physics of the LPBF process needs to be developed.

As mentioned above, changes in the microstructure of an LPBF-made part can cause changes in mechanical and physical properties along with enhancement in the functionality of the final product [25,26]. One of the applicable controlled microstructures is directionally solidified (DS), which exhibits an elongated grain structure along a preferred direction. A well-defined temperature gradient during the casting process results in directional alignment of grains which can impart specific mechanical, thermal, or electrical properties to the material, making it useful in various applications, particularly in aerospace and advanced engineering where controlled material properties are critical [27–30]. The DS microstructure has never been produced using the AM methods. While a comprehensive experimental and numerical analysis of LPBF solidification is essential for achieving printed parts with customized microstructure, it alone is not enough. In this regard, a systematic study is needed to gain the knowledge required to control the formation of DS microstructures, followed by the design and addition of an extra experimental step to the LPBF process.

1.2 Thesis objectives

The major goal of this research is to establish a link between LPBF process parameters and the corresponding microstructure and properties, a numerical model to fill that gap of experimental analysis, and an innovative method for in-situ microstructure control of the LPBF-made Ti-5553 parts (Fig. 1-1). To accomplish the tasks mentioned above, this thesis aims to achieve the following main objectives:

- Investigate the solidification process in the melt pool of the recently developed Ti-5553 alloy, through the fundamental “single-track” and “multi-layer” studies to establish a reliable process map.

- Explore the impact of process parameters on printed part properties, including formed microstructure and mechanical behaviour, for customized manufacturing solutions.

- Develop a new hybrid heat source model to simulate the temperature distribution in the melt pool area and extract thermal variables such as temperature gradient and solidification rate.

- Introduce an innovative "laser post-exposure treatment" for in-situ microstructure control during laser powder bed fusion.

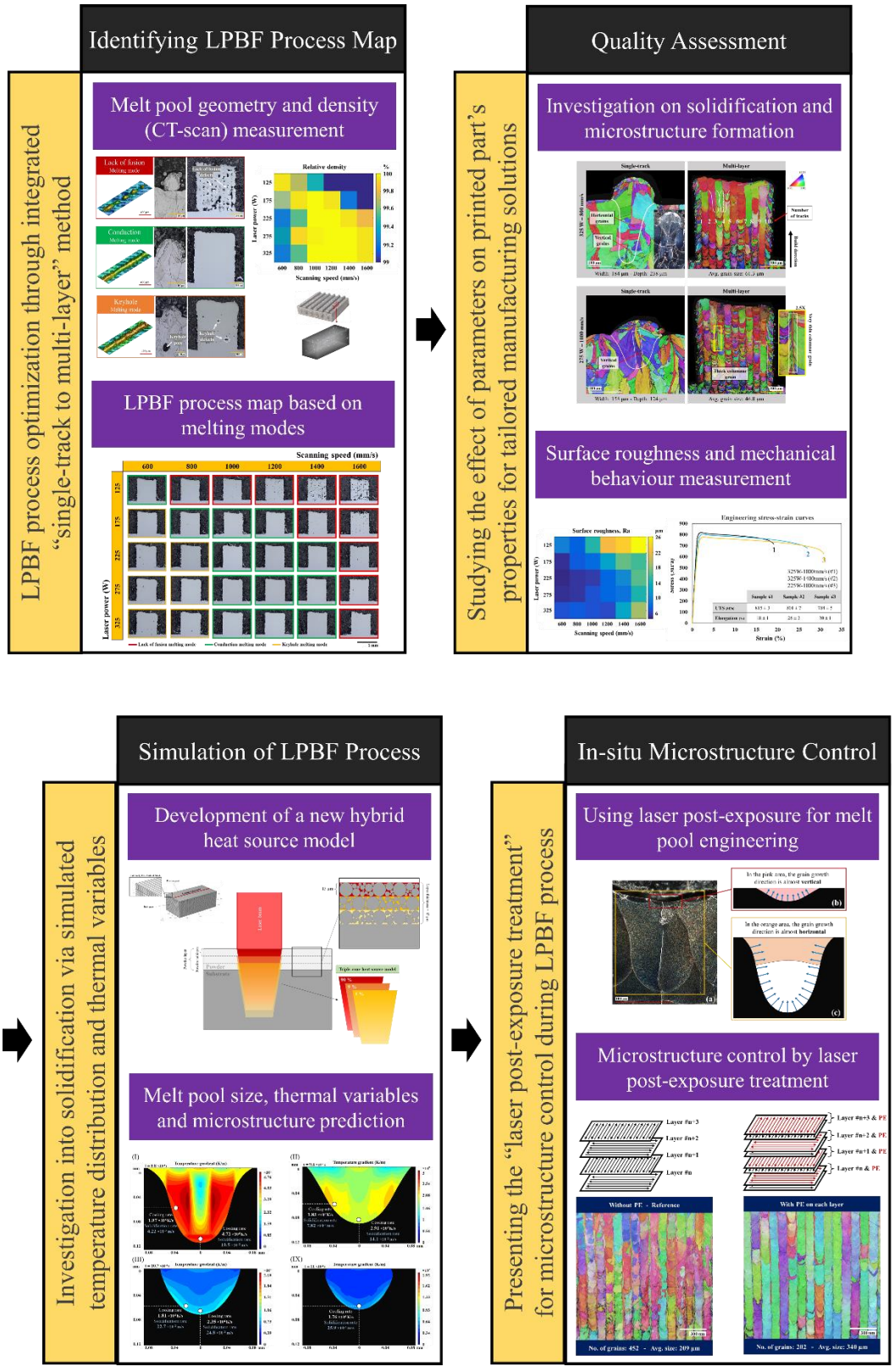

Figure 1-1: Graphical abstract of the objectives in this thesis.

1.3 Thesis outline

This thesis consists of 7 chapters which have been organized in the following way. **Chapter 1** presents a brief overview of LPBF of Ti-5553, problem definition, motivations, objective, and outline of the current research. **Chapter 2** provides a literature review on the LPBF of Ti-5553 and the relevant details about the quality of printed parts. In **Chapter 3**, a comprehensive study on LPBF-made single-track and multi-layer samples was conducted to establish a process map for Ti-5553. In addition to measuring the density of 3D-printed multi-layers, track surface morphology and melt pool geometry for each set of process parameters were thoroughly examined to ensure the reliability of the process map. Continuing from the discussions in Chapter 3 regarding LPBF process optimization, the effects of the significant process parameters on the properties of the printed parts are investigated in **Chapter 4**. Given the distinct properties and qualities associated with each set of process parameters falling within the desired process window, additional investigations, such as the assessment of microstructure and mechanical behaviour, are carried out on these sets. **Chapter 5** proposes a novel hybrid heat source model for the numerical modelling of the heat transfer in the LPBF-made melt pool of Ti-5553. The simulated melt pool geometry, temperature distribution, and thermal variables such as temperature gradient and solidification rate are extracted from the modelling to use for investigation on the solidification and microstructure formation. The gained knowledge from Chapters 3 to 5 is used in **Chapter 6** to introduce the laser post-exposure treatment as an innovative method for in-situ microstructure control during the LPBF process. The post-exposure (PE) treated microstructure is comparable with the directional solidification (DS) microstructure which can anisotropically enhance some mechanical properties such as strength and creep resistance. Finally, a summary of the important findings, conclusions, and scope for future work of the current research are outlined in **Chapter 7**. It should be mentioned that Chapters 3 - 6 are adapted from published papers or submitted manuscripts for publication.

Chapter 2

2 Background and Literature Review

2.1 Additive Manufacturing

Additive Manufacturing (AM), also known as 3D printing, creates components in a layer-by-layer procedure using a computer-aided design (CAD) file. Unlike traditional manufacturing, where a block is formed through casting or forging and then machined to create the final product, AM directly produces the desired geometry with minimal additional processing required [2,31]. One of the key aspects of AM is its ability to create complex parts in a single step, whereas in traditional manufacturing, complex components are assembled from various smaller and simpler parts in subsequent stages [3,7].

AM streamlines the manufacturing process, reducing the number of steps required to produce the final part, whether the material is plastic, concrete, or metal. Various metal AM methods are available, including Laser Powder Bed Fusion (LPBF), Electron Beam Melting (EBM), and Binder Jetting (BJ) [1]. Among these metal AM techniques, LPBF is considered a feasible fabrication method for producing final parts with tailored geometry and properties [9].

2.1.1 Laser Powder Bed Fusion

In Laser Powder Bed Fusion, a thin layer of powder is evenly spread across the build plate by the recoater system. The laser then precisely fuses designated regions on the build plate according to the cross-section defined in the layered CAD file. This cycle is repeated for successive layers until the entire part is fabricated (Fig. 2-1) [32,33]. Due to the unique capability of LPBF in the fabrication of complex parts within anticipated properties, this manufacturing process is widely used in different industries such as aerospace, energy, medical, and automotive [34].

The LPBF process involves numerous independent process parameters, such as laser power, laser scanning speed, hatch space (the distance between two adjacent scan paths), and layer thickness (the thickness of each layer, equivalent to the incremental amount of the lowering building bed) [13]. While manufacturing with multiple process parameters presents challenges and requires optimization, these controllable variables offer significant potential for producing products with

alloys like titanium alloys (Ti-alloys), which conventional production methods often struggle to achieve [3,25].

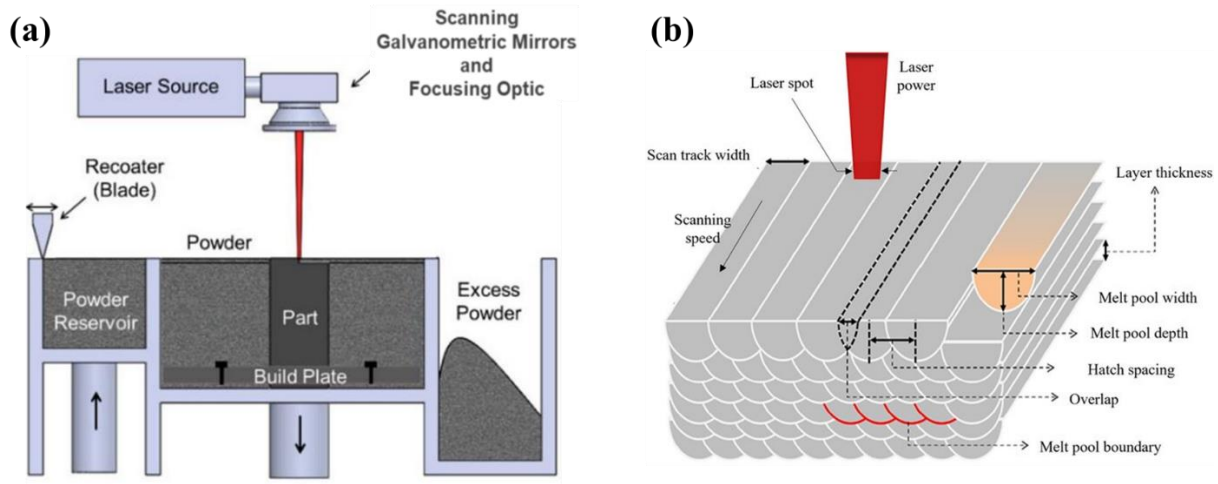

Figure 2-1: (a) Schematic representation of the LPBF process and (b) the LPBF process parameters [32,33].

Compared to other high-strength metals such as steel and Ni-base alloys, machining operations of titanium products are challenging and costly [5]. This difficulty is attributed to several unique physical and chemical properties of titanium. These include its high strength, low thermal conductivity, and chemical reactivity with tool materials, particularly at elevated temperatures, leading to significant tool damage and reduced tool life. Additionally, its relatively low Young's modulus results in spring-back, causing poor surface quality, and its high chemical reactivity, combined with low hardness, can give rise to the galling phenomenon [6,35]. Consequently, AM stands out as one of the most suitable manufacturing processes for creating titanium parts.

2.2 Titanium alloy

Titanium is a nonmagnetic element with low density and a relatively high melting point. The maximum operational temperature for structural titanium components is around 600 °C, which can be enhanced through the addition of alloying elements [6,35]. Various titanium alloys (Ti-alloys) offer a combination of high strength-to-weight ratio, excellent toughness and stiffness, composability, biocompatibility, as well as strong resistance to corrosion and creep. These

exceptional properties make them well-suited for a wide range of applications across industries, including aerospace, automotive, medical, and marine [4,36–38].

2.2.1 Phase metallurgy of Ti-Alloy

Titanium, being a transition element with allotropic behaviour, exhibits varying solid-state crystal structures at different temperature ranges. At low temperatures, pure titanium possesses a hexagonal close-packed (hcp) crystal structure known as the α phase, while at higher temperatures, typically between the beta transus temperature (approximately 885 °C) and the melting point (1670 °C), it adopts a body-centred cubic (bcc) crystal structure known as the β phase [16,39].

The alloying elements in Ti-alloys are primarily chosen based on their impact on the proportions of the α and β phases below the beta transus point. They can be categorized into three groups: Alpha-stabilizers, Beta-stabilizers, and Neutral additions. Alpha-stabilizers are elements that favour the α phase and expand the temperature range in which it exists, effectively raising the beta transus temperature. Aluminium (Al), Gallium (Ga), Germanium (Ge) and interstitial elements (oxygen, nitrogen, and carbon) are some examples of alpha-stabilizer elements. Conversely, beta-stabilizers lower the beta transus temperature and support the stability of the β phase at lower temperatures. The beta-stabilizers are typically bcc in their crystal structure, including Vanadium (V), Molybdenum (Mo), Niobium (Nb), Tantalum (Ta), Chromium (Cr), and Iron (Fe). Neutral additions cause a negligible reduction in the beta transus temperature and dissolve in both α and β phases [39–41].

Based on the aforementioned categorization of alloying elements, titanium alloys (Ti-alloys) can be classified into three primary groups: α alloys, α-β alloys, and β alloys. In addition to these main categories, there are two other subdivisions: near-α alloys and β-metastable alloys. Each of these groups possesses distinct properties. Fig. 2-2 provides a diagram illustrating the influence of alpha-stabilizers and beta-stabilizers on the behaviour of Ti-alloys [6,35,42,43].

The α alloys encompass commercially pure titanium (cp-Ti) and alloys containing α-stabilizers and/or neutral elements. When a small amount of β-stabilizer is added, the Ti-alloys are referred to as near-α alloys. α+β alloys typically have a β volume fraction ranging from about 5% to 40%. The next category is β-metastable titanium alloys, which still exhibit two phases. In β-metastable alloys, the level of β-stabilizer is increased to the point where the β phase no longer transforms

into martensite upon rapid quenching. It is important to note that these alloys can still have a volume fraction of more than 50% α phase. The final group consists of single-phase β alloys, which predominantly consist of β phase [6,35,42,43].

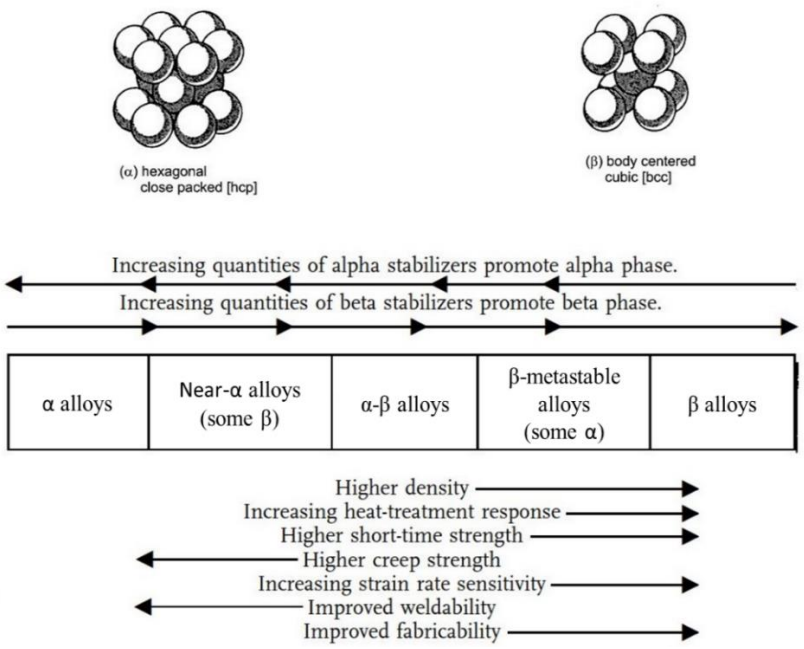

Figure 2-2: Classification of Ti-alloys and effects of alpha-stabilizers and beta-stabilizers on Ti-alloys behavior [6,43].

2.2.2 Ti-5Al-5Mo-5V-3Cr (Ti-5553) alloy details

This study deals with Ti-5Al-5Mo-5V-3Cr (Ti-5553), a β-metastable alloy with martensite-suppressing elements such as V, Mo, Cr, Mn, Fe, Co, Ni, W, Ta, and Nb [44]. In comparison with the most widely used Ti-alloys, Ti-6Al-4V, the addition of Mo has been used to increase the corrosion resistance, Cr improves heat and corrosion resistance and more V provides higher wear and heat resistance [45].

Ti-5553 was designed in the late 1990s, based on the older VT22 alloy, by the VSMPO corporation in Russian, the world's largest titanium producer. They developed Ti-5553 to improve the processability and performance of the established Ti-10V-2Fe-3Al alloy. By the modification, Ti-

5553 has deeper hardenability and is capable of high-strength forging applications [36,46,47]. The β-metastable Ti-5553 has been selected as the truck beam component material based on the high strength and hardenability, of the Boeing 7E7 and Airbus A-380 landing gear. Recently, it has been employed in load-bearing fuselage components, high-lift devices in wide-body aircraft and even nacelles and wings, as well as landing gear [15,16,36,48,49].

As mentioned above, in β-metastable alloys, β-stabilizers are increased to a level where the β phase no longer transforms to martensite upon fast quenching and the final microstructure remains as single-phase β to room temperature. However, slow cooling from above the β transus point, during the manufacturing process or aging heat treatment below the β transus can cause the formation of the α phase [50–52].

In Fig. 2-3, three common types of α phases can be observed in the heat-treated Ti-55531 alloy, which exhibits a microstructure quite similar to that of Ti-5553. These phases include globular primary alpha (α_p), needle-shaped secondary alpha (α_s), and grain-boundary alpha (GBα), which are dispersed within the β matrix. In the lamellar microstructure, coarse lamellar α_s are uniformly distributed within the β phase, whereas in the bimodal microstructure, in addition to the fine α_s, the α_p and GBα are also present [53,54].

The difference in the shape, size and distribution of the α phases in the β phase matrix may have a significant effect on the hardness, strength, toughness and other mechanical behaviours of Ti-5553 [55]. This is one of the most important features of this alloy. For instance, Huang et al. [53], have reported that the lamellar microstructure exhibits remarkably lower strength and slightly higher ductility, compared to the bimodal microstructure. Therefore, the effects of the manufacturing process and supplementary post-processing on the microstructure and phase transformation of Ti-5553 should be taken into consideration.

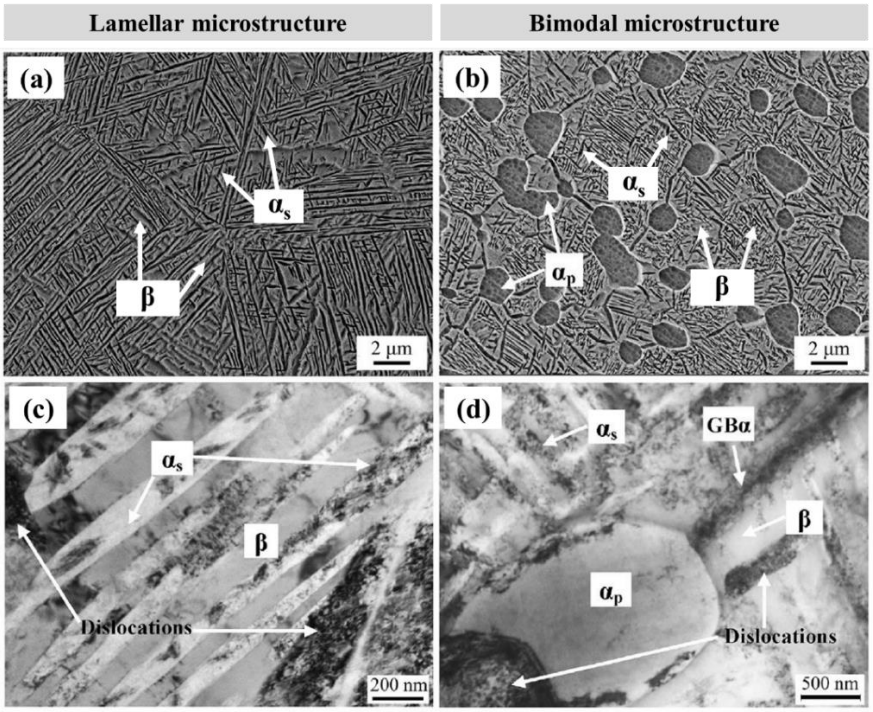

Figure 2-3: SEM images showing (a) the lamellar and (b) bimodal microstructures of heat-treated Ti-55531. The globular primary α, needle-shaped secondary α, and β matrix are marked. The mentioned phases, grain boundary α, and dislocations are also shown in the TEM images of (c) the lamellar and (d) bimodal microstructures [53].

Schwab et al. [55] have investigated the effect of α phase formation on the mechanical properties of printed Ti-5553. Fig. 2-4 shows in the presence of the α phase, the compressive stress of LPBF-made Ti-5553 has been significantly increased by about 60% [55].

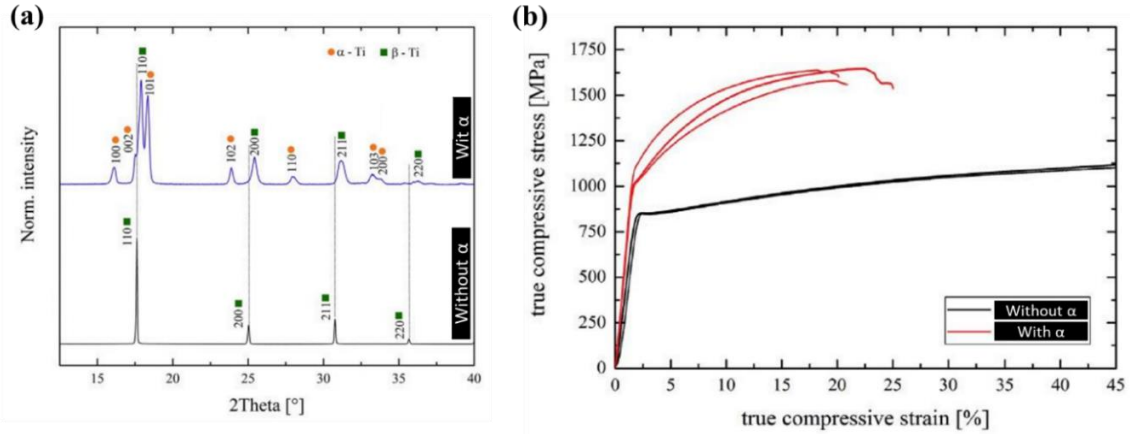

Figure 2-4: (a) X-ray diffraction result confirming the presence of α and β phases, and (b) effect of α phase on compressive strength of two LPBF-made Ti-5553 samples [55].

2.3 LPBF of Ti-5553

Traditional manufacturing encompasses a step-by-step process of converting raw materials or semi-finished products into final items, with each step adding value. Various methods such as casting, machining, and welding are employed, each presenting unique challenges in the production of Ti-alloy parts [38,39].

One of the challenges in the investment casting of Ti-5553 products is the presence of a hard and brittle layer, named α case, on the outer surface of the part which causes defects in the mechanical properties. The formation of this undesirable case is attributed to the interaction between the alloy and the ZrO2 face coating, as well as the remaining oxygen within the shell mould [40,41]. Ti-5553 presents significant challenges when it comes to subtractive manufacturing. This difficulty is mainly due to the high chemical reactivity and low thermal conductivity of titanium, which can lead to a substantial reduction in the lifespan of cutting tools. Additionally, the remarkable high-temperature strength and low elasticity modulus of titanium adversely affect its machinability [13,14]. The welding of Ti-5553 leads to a varied microstructure in the weld region, where the fusion zone suffers from a reduction in Al content and decreased hardness values. During welding, localized heating induces residual stresses as the weld contracts in the final stages of the joining process. These residual stresses not only result in notable distortion but also have a detrimental impact on the fatigue properties [25,42,43].

Unlike conventional manufacturing, which often requires multiple stages to produce intricate shapes, LPBF, as a controllable AM fabrication method, can create highly complex products in a single automated step, eliminating the need for human intervention [4,5]. Moreover, LPBF, the same as other AM techniques, introduces new areas of interest in manufacturing, such as Design for Additive Manufacturing (DfAM). DfAM is an engineering process that enables the creation of more complex shapes and production components, all while reducing both weight and material usage [44].

LPBF is a feasible manufacturing method for Ti-alloy parts fabrication with customized properties, however, achieving these properties is quite challenging due to the involvement of several independent parameters. The multitude of process parameters associated with this method necessitates the optimization of the process for specific materials [4,45]. Achieving high-quality

parts in LPBF relies significantly on the melting and solidification process during manufacturing, necessitating thorough investigation alongside process optimization efforts [10,46]. Simulating the LPBF process offers valuable insights into understanding the impact of process parameters on temperature distribution and thermal condition of the fabricated part, all without the need for conducting a large number of trial-and-error experimental tests [47,48]. Therefore, simulation or modelling serves as a valuable resource for gaining a comprehensive understanding of the LPBF process, particularly when it comes to controlling the microstructure and properties of printed parts [6,49]. In the following sections, process optimization, LPBF modelling, and microstructure evolution will be reviewed.

2.4 Process optimization

Fabricating a part with ideal properties is a challenging task, primarily due to the intricate physical interactions resulting from the laser-powder interaction of the LPBF process and the multitude of process parameters at play. Furthermore, the process parameters vary with different materials, adding another layer of complexity to the printing of a desirable final product [8,56]. Hence, the optimization of the LPBF process for a specific material is necessary.

LPBF of Ti-5553 is a relatively recent development with a limited number of research studies. Schwab et al. [17] studied the printability of Ti-5553 and could successfully print a part with 99.95% density, featuring a tensile strength and strain capacity of around 800 MPa and 14%, respectively. Bakshivash et al. [57] optimized the LPBF process for Ti-5553 using Volumetric Energy Density (VED), achieving a favourable 99.92% relative density, less than 12 μm surface roughness, and a hardness of 295 ± 10 HV.

Volumetric Energy Density is defined as the average energy transferred to a volume of material and it is one of the LPBF parameters representatives that is comprehensive. In addition to determining the process window for a material, the *VED* could be normalized against enthalpy and used for the comparison of multiple materials [58,59]. *VED* [J/mm^3] is given by some different equations and here Eq. 2-1 presents one of the general formulae to calculate that [60,61].

$$VED = \frac{P}{vdl} \tag{2-1}$$

where P represents the laser power [W], ν is the laser scanning speed [mm/s], d is the laser spot diameter [mm] and l is the layer thickness [mm].

Ramachandiran et al. [5] determined the impact of *VED* values on the relative density through Archimedes' density measurements of Ti-5553 samples and were able to show that the highest values were associated with maintaining the conduction melting band. They also investigated the mechanical behaviour and the formed microstructure of full-dense Ti-5553 samples, printed with the lowest and the highest identified *VED.* As shown in Fig. 2-5a, the conduction melting mode can be achieved when the *VED* value is between 39.1 J/mm^3 and 56.1 J/mm^3. Lower and higher than this range exhibit a lack-of-fusion melting mode and a keyhole melting mode, respectively. Fig. 2-5b shows irregular lack-of-fusion defects at *VED* = 30.9 J/mm^3 and spherical keyhole defects at *VED* = 75.5 J/mm^3 [5].

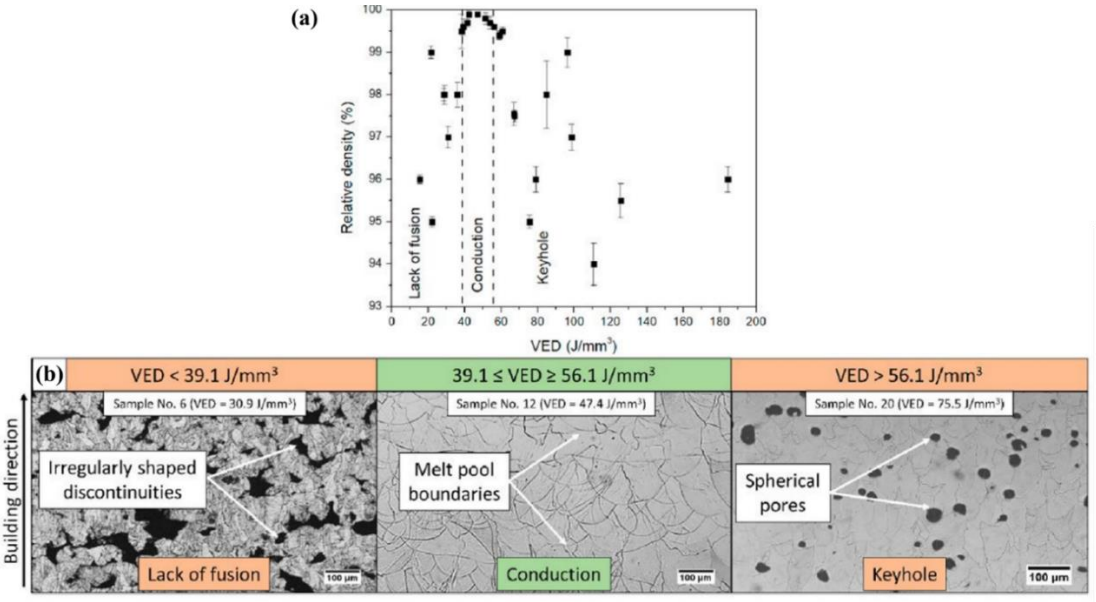

Figure 2-5: (a) Melting mode regions based on Archimedes' relative density across the *VED*s considered (b) OM images of samples printed in different *VED* ranges [5].

The mechanical behaviour of LPBF-made Ti-5553 has been studied and compared to the Ti-5553 parts made by conventional methods. As can be seen in Fig. 2-6, the reported strength and elongation for the as-printed Ti-5553 in the literature are about 780 MPa and 13-35%, respectively [5,17]. It is worth mentioning that the strength and elongation in a vacuum arc melted (VAM) and

forged Ti-5553 alloy have been reported to be approximately 1160 MPa and 5.5%, respectively. The primary cause for the considerable strength variation between as-printed and conventionally manufactured Ti-5553 lies in the reduced formation of the α phase during supercooling in metal printing processes [36,57,62].

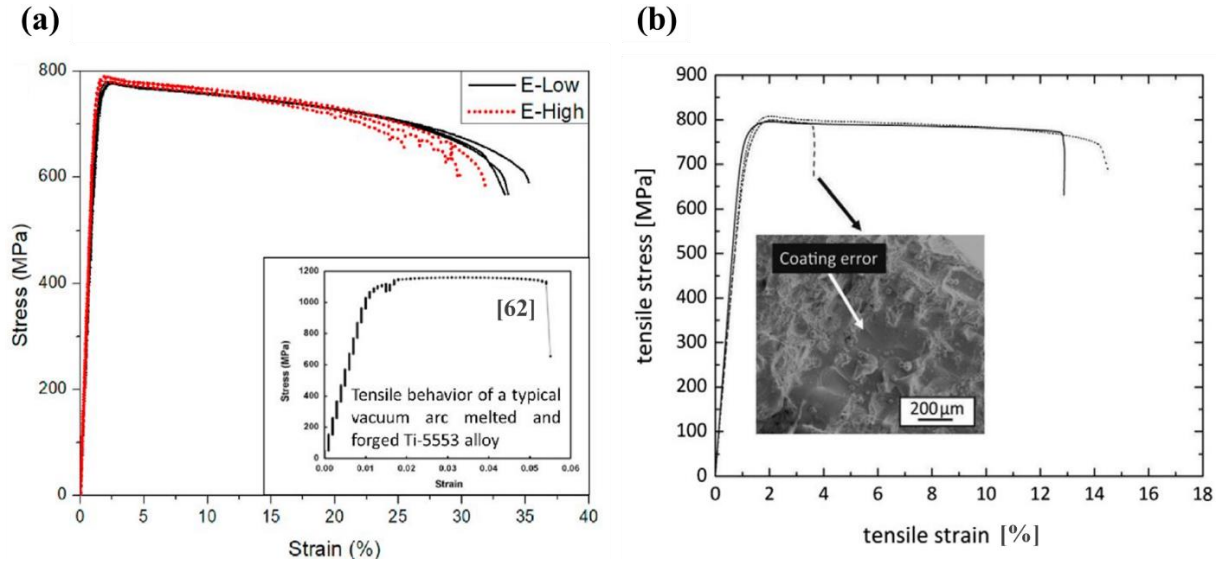

Figure 2-6: (a) Engineering stress-strain curves of LPBF-made samples with E-Low (P=187.5 W & v=1120 mm/s) and E-High (P=187.5 W & v=751 mm/s), compared with VAM and forged Ti-5553 from literature [5,62]. (b) Engineering stress-strain curves of LPBF-made 3 samples with process parameters of P=100 W & v=180 mm/s [17].

The optimization process could be assessed through a methodology that can comprehensively uncover how different main factors such as laser power and scanning speed affect melting and solidification. It should be considered that the common full factorial design of the experiment approaches may require a significant number of sample printing and experiments [63]. A single-track study is a dependable and thorough method for efficiently examining how process conditions affect the quality of printed parts [59,64].

2.5 Experimental single-track study

During the LPBF process, the interaction of laser irradiation and powder material results in two basic phenomena of melting and solidification. Since these two key steps affect significantly the formed microstructure and properties, understanding them is extremely important [3,65].

The melting and solidification phenomena can be precisely studied based on the melt pool features and microstructures [66]. A melt pool refers to the molten region of metal powder particles created by the focused laser beam during the additive manufacturing process. The correlation between the process parameters and the melt pool evolution can show how the process conditions influence the quality of the printing [67]. Hence, a comprehensive single-track study facilitates understanding various aspects of the solidification process [68,69]. In the single-track study, track surface morphology and melt pool size are examined. Tenbrock et al. [64] investigated the single-track geometry created under various laser powers, scanning speeds, and laser spot sizes to optimize the LPBF process for stainless steel (Fig. 2-7) [64].

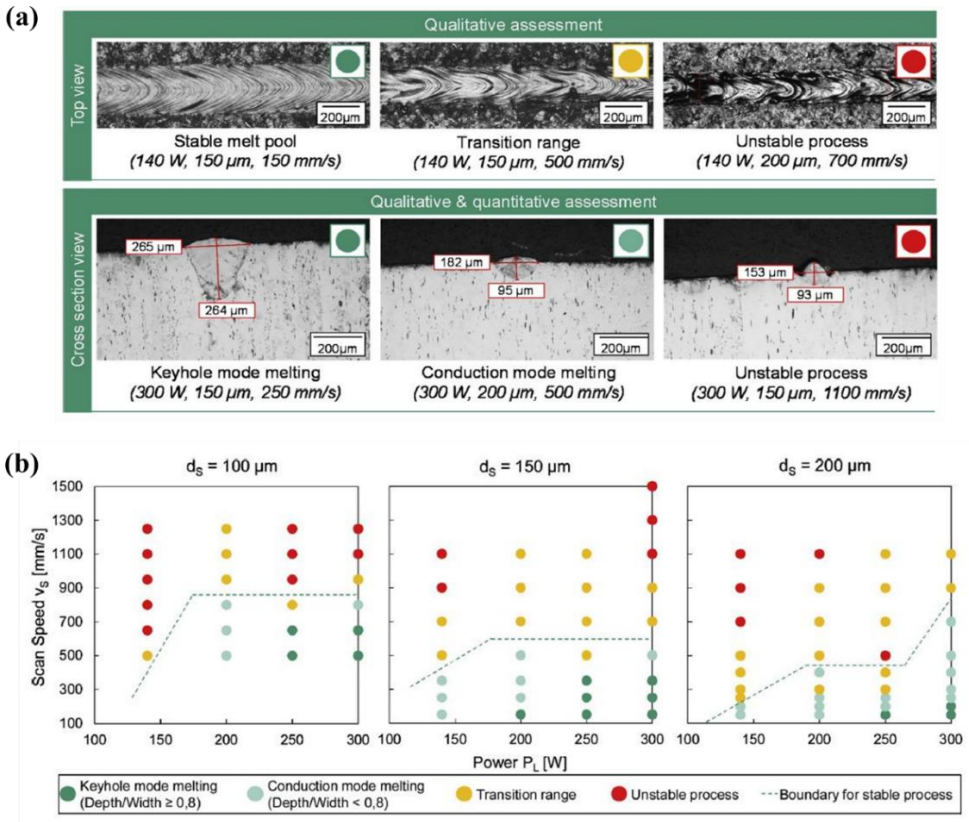

Figure 2-7: (a) Qualitative and quantitative analysis of single-track geometry (the parameters are laser power, spot size, and scanning speed, respectively). (b) Process window based on the single-tracks conditions [64].

In Fig. 2-7a, both qualitative and quantitative assessments of single-track geometry from top and cross-sectional views are presented. In this research, a value of 0.8 has been defined as the melt

pool depth-over-width ratio at the conduction to keyhole melting mode threshold. Fig. 2-7b categorizes the process parameters into four groups based on the conditions of the single tracks: keyhole, conduction, transition, and unstable [64].

In addition to the optimization, the single-track study can be employed for microstructure evaluation. He et al. [70] investigated the influence of laser power and scanning speed on the microstructure formation in LPBF-made H13 steel single-tracks. In Fig. 2-8a, the microstructure characterization reveals that the upper part of the melt pool exhibits a cellular fcc microstructure within a bcc matrix, whereas the microstructure in the bottom part of the melt pool consists of coarse white ferrite (bcc) and fine white ferrite (fcc) within a bcc matrix [70]. Vecchiato et al. [71] examined the microstructure of the 316L steel melt pool and reported the crystal orientation texture of these grains.

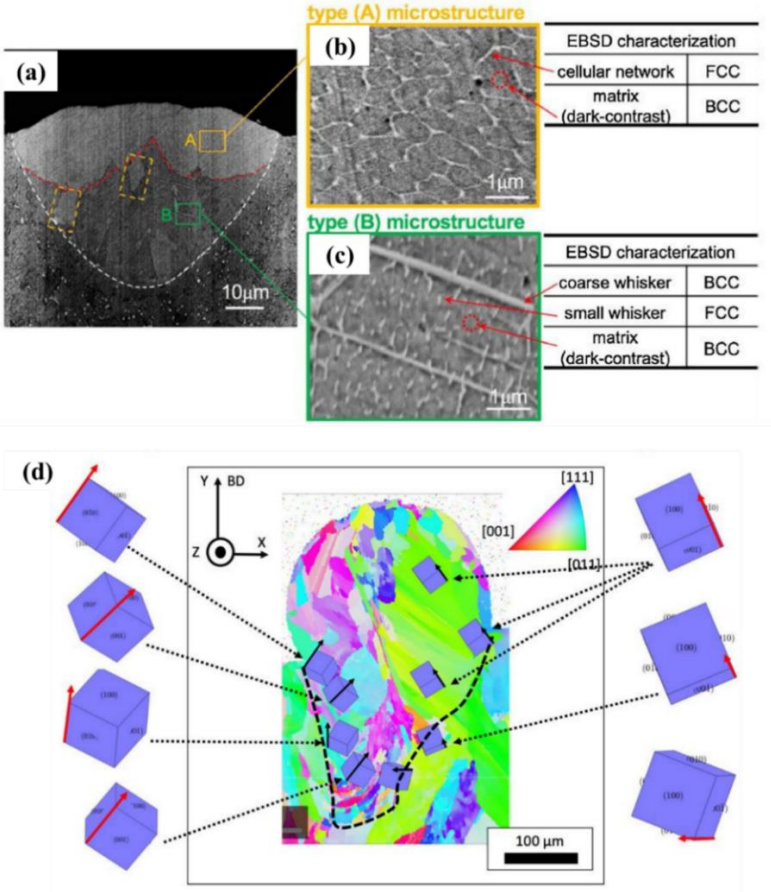

Figure 2-8: (a) Microscopic observation of H-13 steel single-track melt pool and (b)(c) 2 types of detected microstructures [70]. (d) EBSD map shows the grain crystal orientation in the melt pool [71].

It is worth noting that in the experimental analysis, certain critical aspects of the correlation between the formed microstructure and LPBF process parameters remain unknown due to the nearly unmeasurable nature of key thermal variables such as temperature gradient and solidification rate [8,72]. Modelling is a valuable tool for gaining insights into the thermal analysis of the LPBF process, and the next section will review the work of several researchers who have focused on simulating LPBF.

2.6 Numerical thermal analysis

Modelling of the LPBF process provides an insight into understating the effect of process parameters on temperature distribution and thermal condition of the printed part without conducting a high number of trial-and-error experimental tests [72,73]. One of the fastest and most efficient numerical methods to perform thermal analysis for the LPBF process is the Finite Element (FE) method. The FE method has been extensively used for LPBF modelling by many researchers due to the capability of FE to model different laser heat source profiles [74–77].

In the numerical modelling of the LPBF process, several challenging physical phenomena, such as distributed powder material, phase transformation, vaporization, and Marangoni effects, need to be taken into consideration [78–80]. While incorporating all these complex multi-physics aspects enhances the accuracy of the modelling, it may lead to intricate and time-consuming problem-solving. Consequently, some researchers have proposed conduction-based modelling for microscale continuous-domain simulation. In this type of modelling, fluid dynamics and convective thermo-flow are neglected (conduction-based), the interaction between the heat source and the material is studied on the scale of melt pools (microscale), and instead of treating individual powder particles as independent domains, continuous geometry domains are modelled (continuous-domain) [20,23,81–85].

To assess the temperature distribution and the formation of melt pools during the LPBF process, a heat transfer problem can be defined by considering the significant thermal mechanisms. Two primary 3D components can be designed: a powder part and a bulk part. The laser beam irradiation can be modelled as a moving heat source that inputs heat flux onto the top of the powder part (Fig. 2-9). The material's initial state and thermophysical properties (e.g., thermal conductivity, density, and specific heat capacity) must be considered for both mentioned parts. Achieving a reliable

solution necessitates the consideration of material state variations at different temperatures and conditions [23,83,86,87].

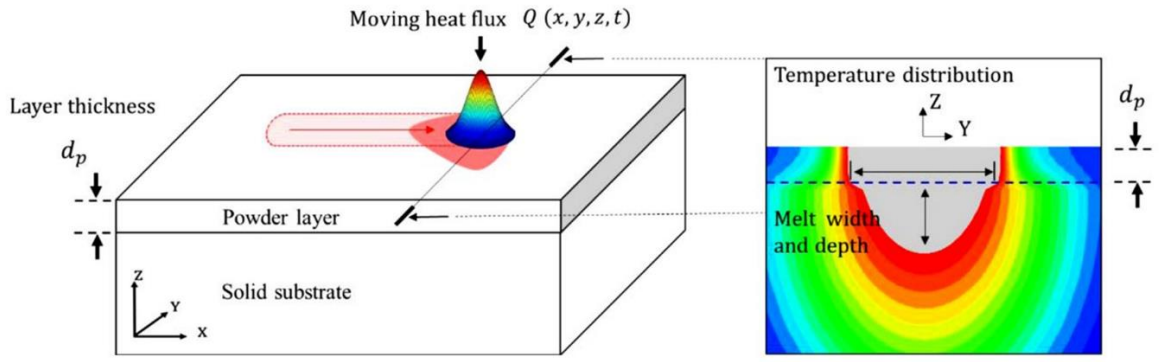

Figure 2-9: Schematic diagram of the LPBF process with a temperature distribution cross-section [84].

Fig. 2-9 depicts a schematic diagram of the LPBF process featuring a modelled 3D moving heat flux with Gaussian heat distribution, along with a cross-sectional view of the temperature distribution in the molten pool and heat-affected zones [84]. As shown in Fig. 2-9, the shape and dimensions of the melt pool can be extracted from the simulation.

The melt pool geometry prediction is one of the most useful applications of the LPBF process simulation. The melt pool shape and geometry contain some valuable information such as material printability, acceptable process parameters range, melting and solidification modes, and possible defects [10,70]. Also, the comparison of simulated melt pool dimensions with experimentally measured melt pool size can be used for model validation and calibration.

Fig. 2-10a reveals the simulated melt pool dimensions. In this figure, the simulated melt pool depth, width, and length are 190 μm, 135 μm, and 660 μm, respectively [88]. Fig. 2-10b illustrates a comparison between experimental and numerical melt pool geometry. The simulation shows a good agreement with the size of experimental track cross-sections [89].

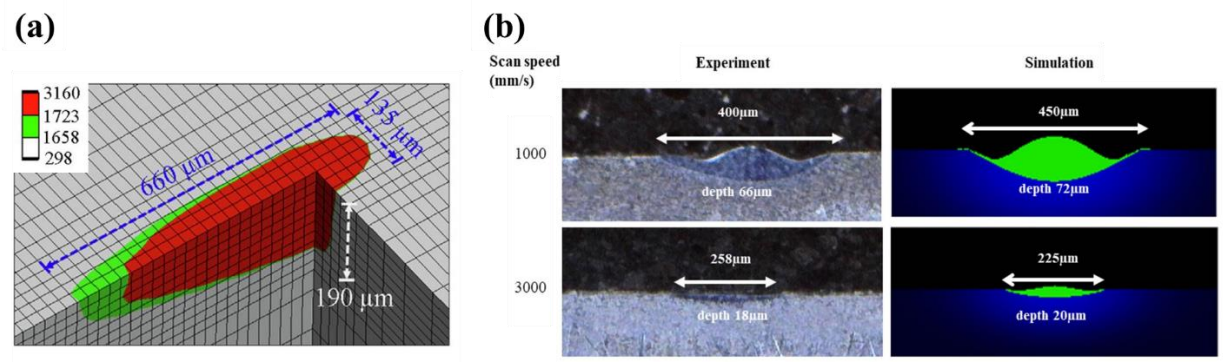

Figure 2-10: (a) Simulated melt pool dimension [88]. (b) Comparison of the experimentally and numerically measured melt pool geometry, created under different scanning speeds [89].

Another valuable application of LPBF process modelling is the prediction of microstructure by calculating thermal variables such as temperature gradient and solidification rate. As illustrated in Fig. 2-11a, the cooling rate, temperature gradient, and solidification rate are extracted from various points in the modelled melt pool. By correlating these calculated thermal variables with experimental grain morphology, a criterion for the columnar-to-equiaxed transition (CET) in single tracks can be established [86]. Additionally, the simulated cooling rate can be combined with empirical equations to predict the primary dendritic arm spacing (PDAS) in the melt pool (Fig. 2-11b) [90].

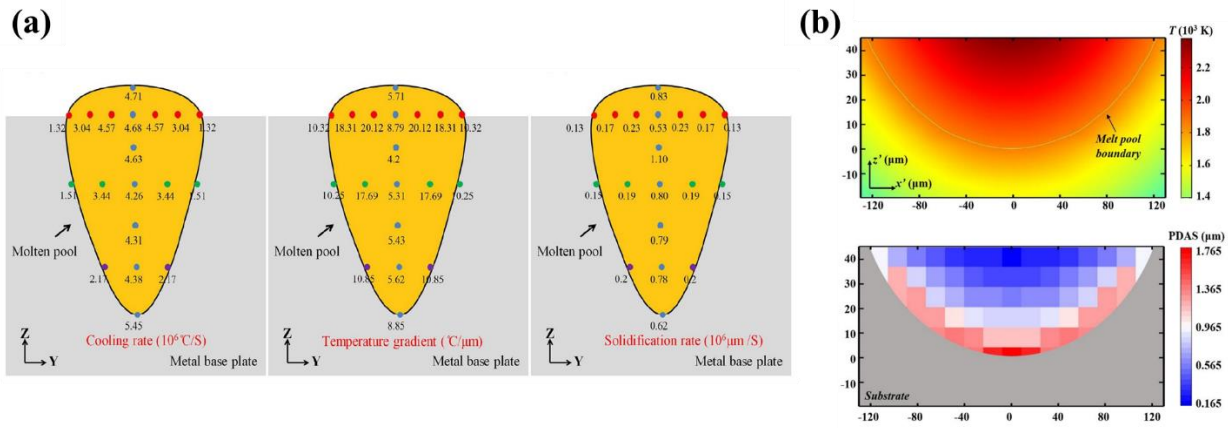

Figure 2-11: (a) Estimated cooling rate, temperature gradient and solidification rate at different points of the modelled melt pool [86]. (b) Simulated temperature distribution across the transverse section of the melt pool and site-specific primary dendritic arm spacing (PDAS) across the melt pool [90].

The knowledge gained from experimental and numerical analysis of melt pool solidification provides a more precise understanding of the microstructure formation, which can be utilized for microstructure control in LPBF [91,92]. Microstructure control is a novel topic that has garnered considerable attention among researchers in the field of additive manufacturing.

2.7 Microstructure control in LPBF

While the large number of process parameters in additive manufacturing can pose a challenge to achieving optimal quality, it provides the manufacturer with more flexibility in controlling the manufacturing process. If the manufacturers thoroughly understand the relationship between process parameters and manufacturing conditions, controlling these parameters enables them to engineer the microstructure and properties of the printed part [26,34,92]. This is one of the advantages of additive manufacturing that is sometimes not achievable in traditional production methods.

Microstructure control is carried out through various methods, but almost all of them are based on temperature distribution and melt pool geometry control. The use of various scanning strategies and different laser intensity profiles (laser beam shaping) are among the methods of controlling microstructure [93–95]. For instance, Ishimoto et al. [96] employed various X-Scan and XY-Scan strategies to control crystallographic orientation. As depicted in Fig. 2-12, a 90° rotation of scanning in each layer produces a distinct crystallographic texture. They deduced that the microstructure achieved through the XY-scan strategy resulted in anisotropy, manifesting in a decreased Young's modulus along the build direction of the printed specimens [97].

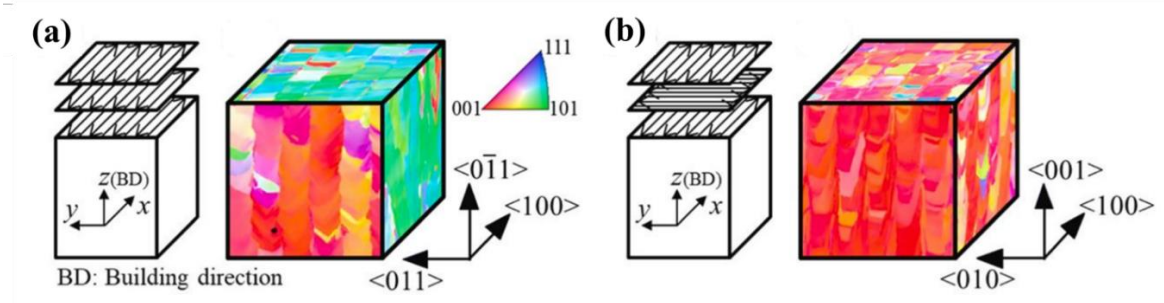

Figure 2-12: Schematic representation of scanning strategy and the developed crystallographic texture for (a) X-Scan and XY-Scan [96].

Marattukalam et al. [98] reported on how scanning strategies can result in different textures, thereby influencing mechanical properties. As illustrated in Fig. 2-13b, the samples created by Y-Scan and Z-Scan exhibit preferential growth directions of the columnar cells parallel to <110> and <100>, respectively, whereas the sample created by Rot-Scan displays a random crystallographic texture. Fig. 2-13a demonstrates that the mechanical behaviour, influenced by microstructure, can be significantly different [98].

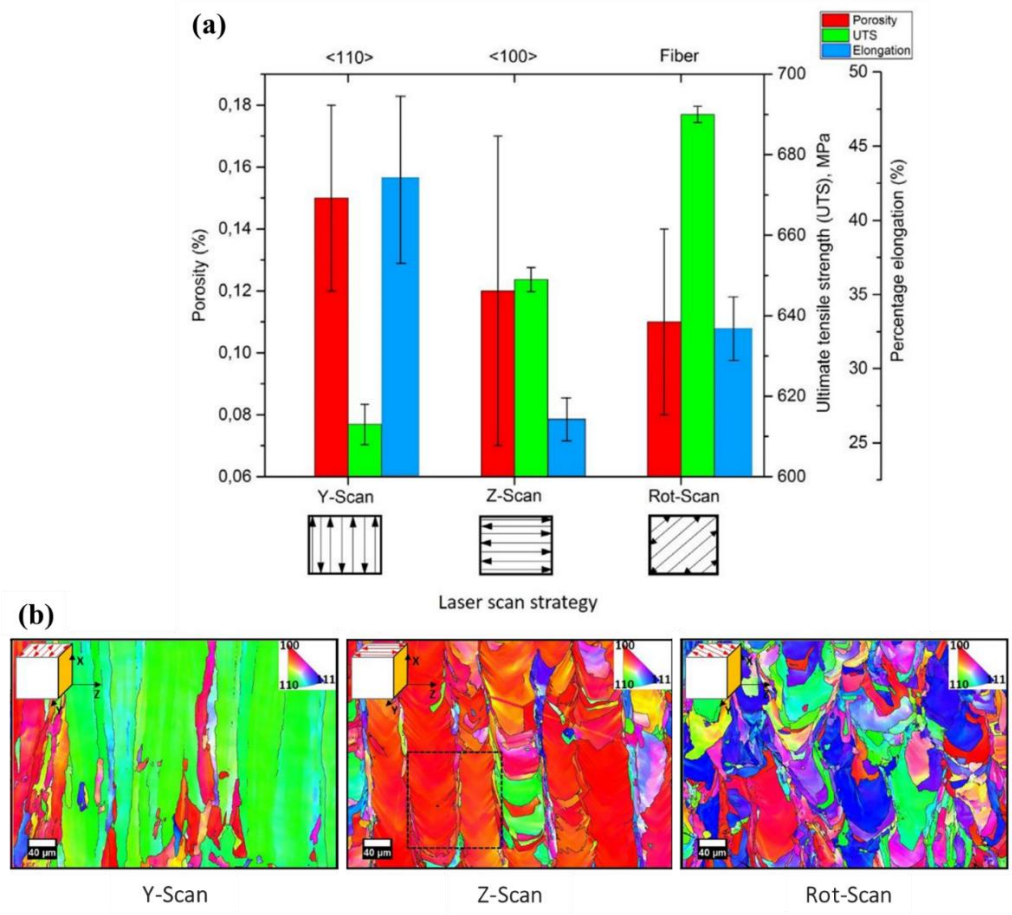

Figure 2-13: (a) Variation in porosity, ultimate tensile strength, and percentage elongation with different laser scanning strategies. (b) EBSD IPF maps, showing crystallographic grain orientations when scanned along the Y-axis, Z-axis and at 67° rotation [98].

Laser beam shaping is emerging as another method for microstructure control, attracting recent attention from researchers [99,100]. Roehling et al. [101] studied the impact of Gaussian and

elliptical beam profiles on controlling grain nucleation and morphology. Figures 2-14a and 2-14b illustrate the simulated formation of single-tracks and melt pools using Gaussian and elliptical beam shapes, respectively. As depicted in Figures 2-14c to 2-14f, although the crystallographic texture in all samples is the same, the microstructure fabricated by the Gaussian beam shape exhibits a higher grain size compared to samples created by the elliptical beam shape [101].

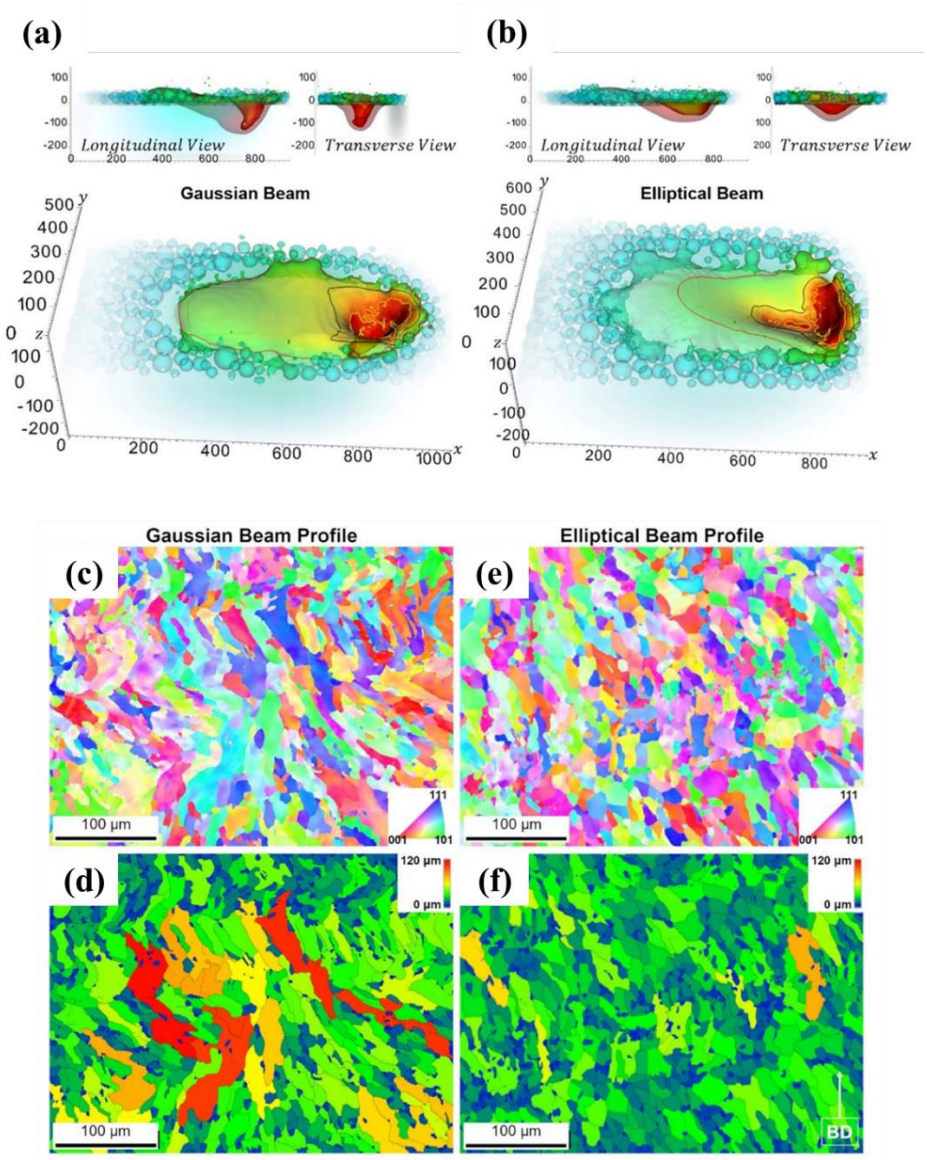

Figure 2-14: Simulation of single tracks formed using (a) a Gaussian beam shape and (b) an elliptical beam shape. Inverse pole figure (IPF) maps and grain size analysis for microstructures of cubes built with (c,d) a Gaussian beam and (e,f) an elliptical beam [101].

In addition to the mentioned methodologies, there are other innovative methods utilized for microstructure control. One such method, employed by Schwab et al. [55], involves regulating the formation of the α phase in Ti-5553. They maintained a constant build plate temperature of 500°C during LPBF, effectively inducing a heat treatment during production, resulting in a higher α phase content in the final microstructure [4,55]. In the current thesis, an innovative approach will be proposed using secondary laser scanning to control the grain morphology of the printed part. This method, termed "laser post-exposure treatment," will be discussed in Chapter 6.

2.8 Summary

Among AM techniques, LPBF stands out as a highly effective method for manufacturing customized metallic parts, especially when conventional manufacturing faces challenges. The production of titanium parts, known for their versatility, proves difficult with subtractive methods, making LPBF a suitable alternative. Despite recent research efforts exploring LPBF processes with various materials, several unknowns persist, particularly concerning the LPBF of recently developed alloys like Ti-5Al-5V-5Mo-5Cr (Ti-5553). An in-depth comprehension of the LPBF process for metals hinges upon a precise understanding of melting and solidification phenomena. Integrating experimental single-track and multi-layer studies, with numerical modelling of melting and solidification in the melt pool yields comprehensive insights that have not been done so far. The capability to control the microstructure and tailor the properties of printed parts stands as a distinct advantage of additive manufacturing, often unattainable in conventional manufacturing methods. Although the formed microstructure under various controlling methods has been studied, targeted microstructure control (e.g., directionally solidified (DS) microstructure), especially for Ti-5553, has not been carried out. Based on the published studies, while a comprehensive experimental and numerical analysis of LPBF solidification is essential for achieving Ti-5553 printed parts with customized quality, a systematic study is needed to gain the knowledge required to control the formation of tailored microstructures during the LPBF process.

Chapter 3

3 LPBF Process Optimization through Comprehensive Single-track and Multi-layer Studies

3.1 Introduction

Additive manufacturing (AM) is an advanced fabrication method used to construct parts through layer-by-layer deposition. AM offers incredible potential for manufacturing products with alloys like titanium alloys (Ti-alloys), which face difficulties in conventional production methods [1–3]. While Ti-alloys find extensive use in various industries because of their high strength-to-weight ratio, excellent corrosion resistance, and good toughness, the machining operation of Ti products is not simple [4–6]. To address these challenges, Laser Powder Bed Fusion (LPBF) as a metallic AM method can offer an ideal solution. LPBF is known for its feasibility in fabricating parts with customized properties, but obtaining these properties is quite challenging due to the involvement of several independent parameters [7,8]. The quality of the produced piece is highly dependent on the process parameters, as these parameters directly affect the melting and solidification of the molten metal [14,102,103]. Hence, an investigation into the effect of process parameters on the melting and solidification condition is necessary for the quality assessment of a printed part [13].

Among Ti-alloys, recently developed β-metastable Ti-5Al-5V-5Mo-5Cr (Ti-5553) offers a wide processing window, and excellent heat treatability, making it a preferred material in the aircraft industry [15,16]. LPBF of Ti-5553 is a relatively new development, and as a result, there is a limited number of published research studies on this topic. Schwab et al. [17] conducted a study on the printability of Ti-5553 and successfully printed a part with a density of 99.95% and a pure β phase microstructure, which achieved a tensile strength of about 800 MPa and a strain of up to 14%. Bakshivash et al. [57] optimized the LPBF of Ti-5553 using the volumetric energy density (*VED*). They achieved a good relative density of 99.92%, a surface roughness of < 12 μm, and a hardness of 295 ± 10 HV, using a *VED* of 112 J/mm^3 [57]. Ramachandiran et al. [5] investigated the mechanical behaviour and the formed microstructure of full-dense Ti-5553 samples printed with the lowest and highest identified *VED*. The printed samples exhibited a YS/UTS of 780 ± 10 MPa with an elongation of 30 ± 5% [5].

Tailored manufacturing requires an in-depth understanding of how the main LPBF process parameters influence the melting and solidification conditions. Keshavarzkermani et al. [59] conducted the "single-track study" method to investigate how LPBF process parameters affect the melt pool solidification of Hastelloy X, examining the geometry and microstructure of the single-track melt pools under varying process parameters. The single-track study is a detailed examination of the single-scan laser tracks on the powder material to understand how process conditions affect the formation and characteristics of the melt pool [10]. This fundamental method has been extensively used in experimental research and modelling by several researchers [56,78,104–107]. The single-track study will be more productive when coupled with the evaluation of 3D samples, allowing for a more holistic understanding of the fabrication. Guo et al. [68] proposed a process map for IN738LC, based on characteristics of track morphology, melt pool geometry, and the pore condition in the printed bulk samples. In addition to the fabrication map, He et al. [70] established a relationship between the microstructure and the cracking behaviour of H13 tool steel through a single-track to 3D cube study.

In this chapter, the single-tracks, along with multi-layers were studied to systematically identify the optimal process parameters and explore the impact of these parameters on the quality of the printed Ti-5553. The knowledge gained from the investigation of track morphology and melt pool geometry was integrated with the observed microscopic examinations and X-ray computed tomography measurement to create a reliable process map.

3.2 Material and experiment

In this section, the sample fabrication and characterization methods that were employed for the identification of the process map (Chapter 3) and the investigation of the effect of process parameters on the properties of the printed parts (Chapter 4) will be introduced.

3.2.1 Sample fabrication

Plasma-atomized Ti-5553 powders, produced by AP&C were used to fabricate test specimens with chemical compositions (wt.%) as reported in Table 3-1. The fabrication was carried out using the EOS M290 machine, which was equipped with a 400 W ytterbium continuous fibre laser with a wavelength of 1060 nm, under a high-purity argon gas atmosphere.

Table 3-1: Chemical composition of the as-received Ti-5553 powder

Al	V	Mo	Cr	Fe	O	N	C	Ti
5.14	4.98	4.97	2.91	0.37	0.09	0.01	0.01	Balance

Single-tracks and multi-layers of Ti-5553 were printed on substrates, with varying laser power (125, 175, 225, 275, and 325 W) and scanning speed (600, 800, 1000, 1200, 1400, and 1600 mm/s). The layer thickness for single-tracks, multi-layers, and substrates was maintained at 45 μm. Table 3-2 provides the parameters used in the single-track and multi-layer experiments. These initial process parameters have been chosen based on the published literature on LPBF of Ti-5553 [5,57].

Table 3-2: Process parameters of single-track and multi-layer samples

Process parameter	Value
Power (W)	125 – 175 – 225 – 275 – 325
Scanning speed (mm/s)	600 – 800 – 1000 – 1200 – 1400 – 1600
Layer thickness (μm)	45

The block substrates were fabricated using the same printing parameters, including a laser power of 225 W, a scanning speed of 1000 mm/s, a layer thickness of 45 μm, and a hatch distance of 100 μm. The stripe scanning strategy, with a 67° random rotation was used in each layer. For the single-track samples, the rectangular block substrate had dimensions of 25 mm × 21 mm × 5 mm. As shown in Fig. 3-1a, on top of each rectangular substrate, 2 different sets of parameters were applied, with three replicates each (e.g., green lines: P = 275 W & v = 600 mm/s and red lines: P = 275 W & v = 800 mm/s), where the distance between each single-track was 3 mm.

Similar to single-track samples, a rectangular block (22.5 mm × 20 mm × 5 mm) was designed and served as the substrate for the multi-layers. On top of each substrate, 6 different multi-layers were printed, each with distinct process parameters (1 fixed laser power and 6 varying scanning speeds). Each multi-layer consisted of 10 tracks and 25 layers. Due to the hatch distance of 100 μm and a layer thickness of 45 μm, the exact dimensions of each multi-layer cross-section were 1.125 mm × 1 mm. An X-scan (stripe, without rotation) scanning strategy was used for multi-layer

printing. In total, 30 sets of process parameters were used for printing 90 single-tracks (with 3 replications) on 15 substrates and 30 multi-layers on 5 substrates. The schematic and real image of a single-track sample and a multi-layer sample are shown in Fig. 3-1.

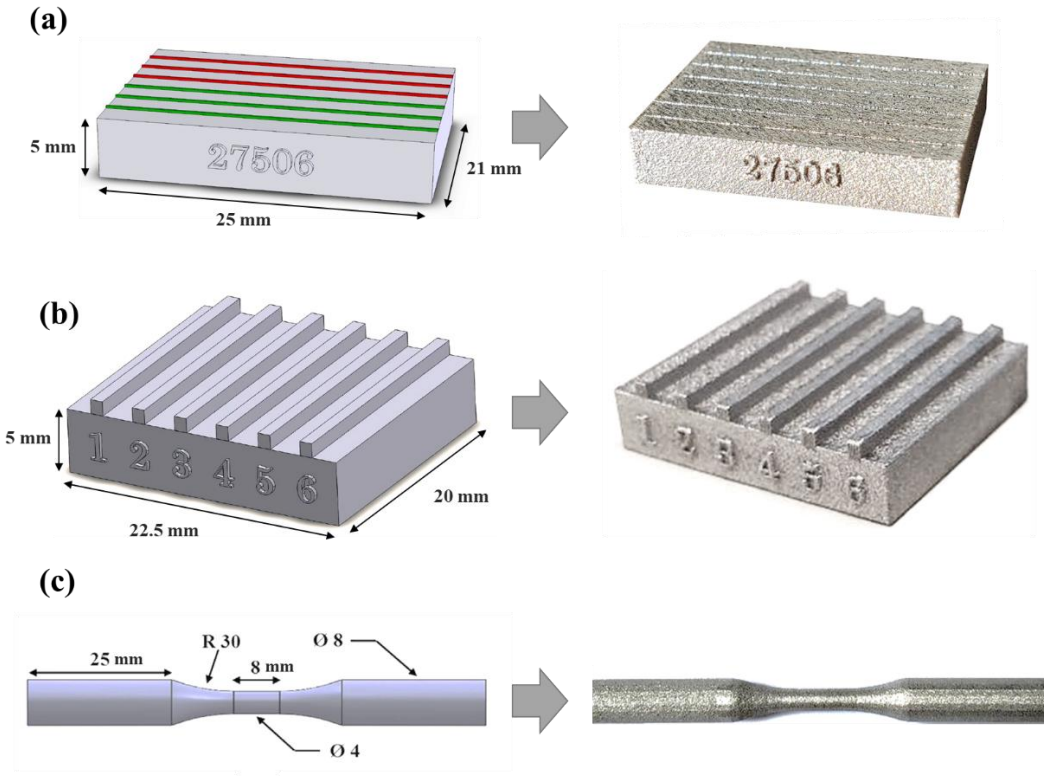

Figure 3-1: The schematic and real images of (a) a single-track sample with 2 different single-tracks and 3 replications, (b) a multi-layer sample with 6 different multi-layers, and (c) a tensile test specimen geometry.

In this research work, 3 tensile test samples, each with 5 repetitions, were also printed and examined. These samples were printed with three selected process parameters as follows: P = 175 W & v = 1000 mm/s, P = 325 W & v = 1000 mm/s, and P = 325 W & v = 1400 mm/s. All process parameters, except for the scanning strategy (which is XY-scan with a 90° rotation), remained the same as the multi-layer printing parameters. The dimensions of the tensile test specimens are depicted in Fig. 3-1c.

3.2.2 Characterization

In preparing the metallographic samples, the single-track specimens were precision sectioned using a Buehler ISOMET 1000 saw. This procedure involved cutting them at a specific point along the track line, precisely one-third of the way, and perpendicular to the track scan direction. The sections obtained from the cuts were then mounted, ground, and polished according to standard procedures. Subsequently, they were etched using Keller's reagent, composed of 95 ml distilled water, 2.5 ml HNO3, 1.5 ml HCl, and 1 ml HF. For electron microscopy investigations, an additional step was incorporated into the preparation process. This involved using a non-crystallizing amorphous colloidal silica suspension (Buehler MasterMet2) with a particle size of 0.02µm. The specimen was polished using a Buehler VibroMet2 vibratory polisher for approximately 5 hours.

3D surface morphology of single-track and multi-layer samples was measured using a Keyence VK-X250 confocal laser microscope. Melt pool boundaries were observed at high resolution using a Keyence VHX-7000 optical microscope (OM) at 6000X magnification. Scanning electron microscopy (SEM) and electron backscatter diffraction (EBSD) analyses were conducted with a TESCAN VEGA3 SEM equipped with a BRUKER e-FlashFS detector. Phase identification of selected multi-layer samples was performed using a Bruker D8 DISCOVER X-ray diffraction machine with a copper cathode. The operational voltage used was 40 kV, with a current of 44 mA. The scan speed was set at 0.5° per minute, and the designated scan range spanned from 20 to 120 degrees.

To assess the distribution of porosity, the ZEISS Xradia 520 Versa X-ray computed tomography (CT) system was employed. This was performed on the multi-layer blocks (1 mm × 1 mm × 5 mm) for each manufacturing condition. It involved scanning 801 2D projections at 140kV, with an exposure time of 1 second and a voxel size of 6µm. Subsequent analysis of the 3D reconstructed images was carried out using the commercial software Dragonfly 3.1. To study the mechanical behaviour of printed samples, uniaxial tensile tests were conducted using an Instron 8872 servohydraulic frame with a load capacity of 25 kN, at a crosshead speed of 0.45 mm/min, following the ASTM E8 standard. To evaluate the microhardness in multi-layer cross-sections, a Clemex CMT automated microhardness tester (300 g force with 10 s dwell time) was employed.

3.3 Result and Discussion

3.3.1 Single-track geometry

3.3.1.1 Track profilometry

As mentioned in section 3.2.1, 90 single-tracks with 30 sets of process parameters and 3 replications were printed on 15 LPBF-made substrates. The laser power ranged from 125 to 225 W, the scanning speed ranged from 600 to 1600 mm/s, and the layer thickness was set at 45 μm. To find a reliable process window, the track profilometry and melt pool geometry were measured from micrographs. Fig. 3-2 shows the geometrical features of the single tracks with different combinations of process parameters.

Based on the examination of the top surface morphology, single tracks can be classified into two types: continuous and discontinuous. Continuous single tracks exhibit an uninterrupted, straight, and regular section profile with minimal width variation along the track length on top of the substrate. This type of track is achieved when the volumetric energy density (*VED*) reaches a critical value, resulting in more consistent melting. In contrast, insufficient *VED* leads to improper wetting and poor flow of the molten powder particles over the substrate, resulting in non-uniform and discontinuous tracks. Discontinuous tracks exhibit some irregularities along the track length and significant width variation, which can lead to the formation of lack-of-fusion defects in printed parts [10–12].

According to the track morphology depicted in Fig. 3-2, the lack-of-fusion defect is expected in the part created with low power parameters such as P = 125 W & v = 1600 mm/s, P = 125 W & v = 1400 mm/s, and P = 125 W & v = 1200 mm/s, and high scanning speed parameters like P = 175 W & v = 1600 mm/s, and P = 225 W & v = 1600 mm/s.

To achieve a desirable continuous track, it is essential to ensure that the *VED* value also does not exceed a specific limit [58,108]. When the *VED* reaches very high levels, such as 120.4 J/mm^3 (P = 325 W & v = 600 mm/s), 101.9 J/mm^3 (P = 275 W & v = 600 mm/s), and 90.3 J/mm^3 (P = 325 W & v = 800 mm/s), the resulting single tracks appear relatively wider than those created with moderate and low *VED*, indicating potential overexposure (see Fig. 3-2). Consequently, continuous single tracks can be categorized into two types: regular (narrow) and overexposed

(wide) tracks. Part printing with continuous regular tracks results in a desirable conduction melting mode, while continuous overexposed tracks can lead to non-desirable keyhole defects [68,70,109]. These melting modes and defects will be discussed in later sections.

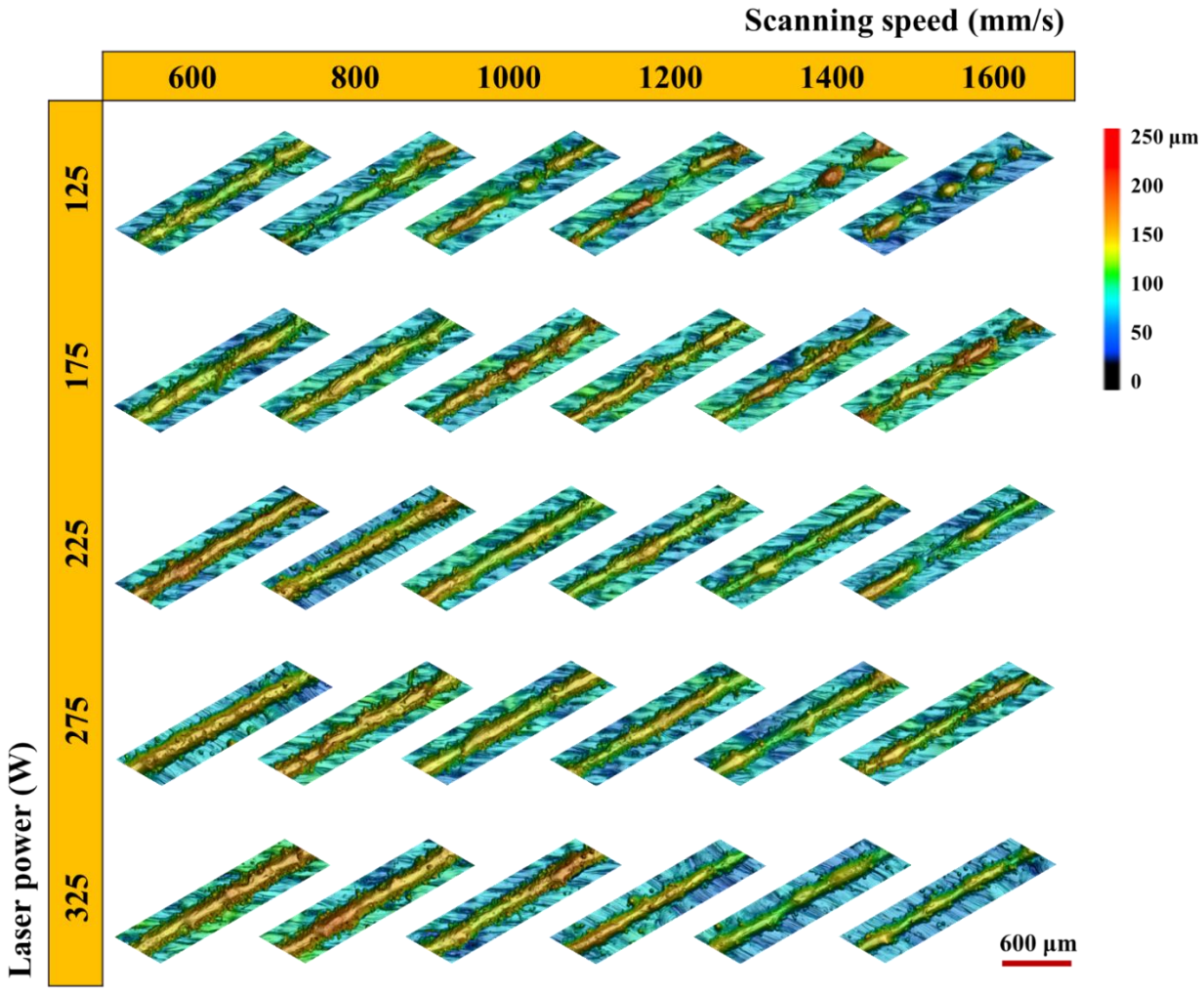

Figure 3-2: Experimental surface profilometry measured by confocal microscope to show the geometrical features of the single tracks at different conditions.

3.3.1.2 Melt pool dimensions

As the track geometry is the basic building block for the additive manufacturing process, it directly affects the properties of the printed part and should be considered in the AM fundamental research

[107]. Alongside the top-surface morphology of the tracks, the dimensions of the track melt pool help determine the LPBF process window. As illustrated in Fig. 3-3, these dimensions are defined by the melt pool depth, width, and bead height.

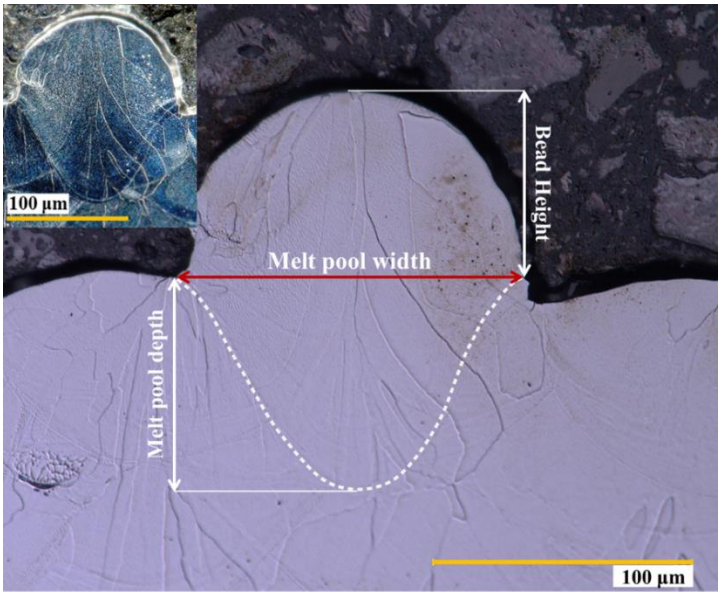

Figure 3-3: Optical microscopic image: cross-section of an LPBF-made single-track (P = 225W & v = 1400 mm/s). The bright and dark images have been captured by full coaxial and full ring illumination modes, respectively.

Fig. 3-4 provides a qualitative representation of the geometry of the single tracks, while Fig. 3-5 illustrates the measured melt pool size as a function of laser power and scanning speed. Melt pool width and depth were determined using micrographs of cross-sections from individual tracks. The trend in melt pool depth and width with different process parameters reveals that the deepest and widest melt pool is associated with the highest *VED*, characterized by the highest laser power and the lowest scanning speed (P = 325W & v = 600 mm/s). Conversely, the smallest melt pool is associated with the lowest *VED*, characterized by the lowest laser power and the highest scanning speed (P = 125W & v = 1200 mm/s). Notably, the melt pool dimensions of single tracks with a laser power of 125 W and scanning speeds of 1400 and 1600 mm/s could not be consistently measured due to their instability.

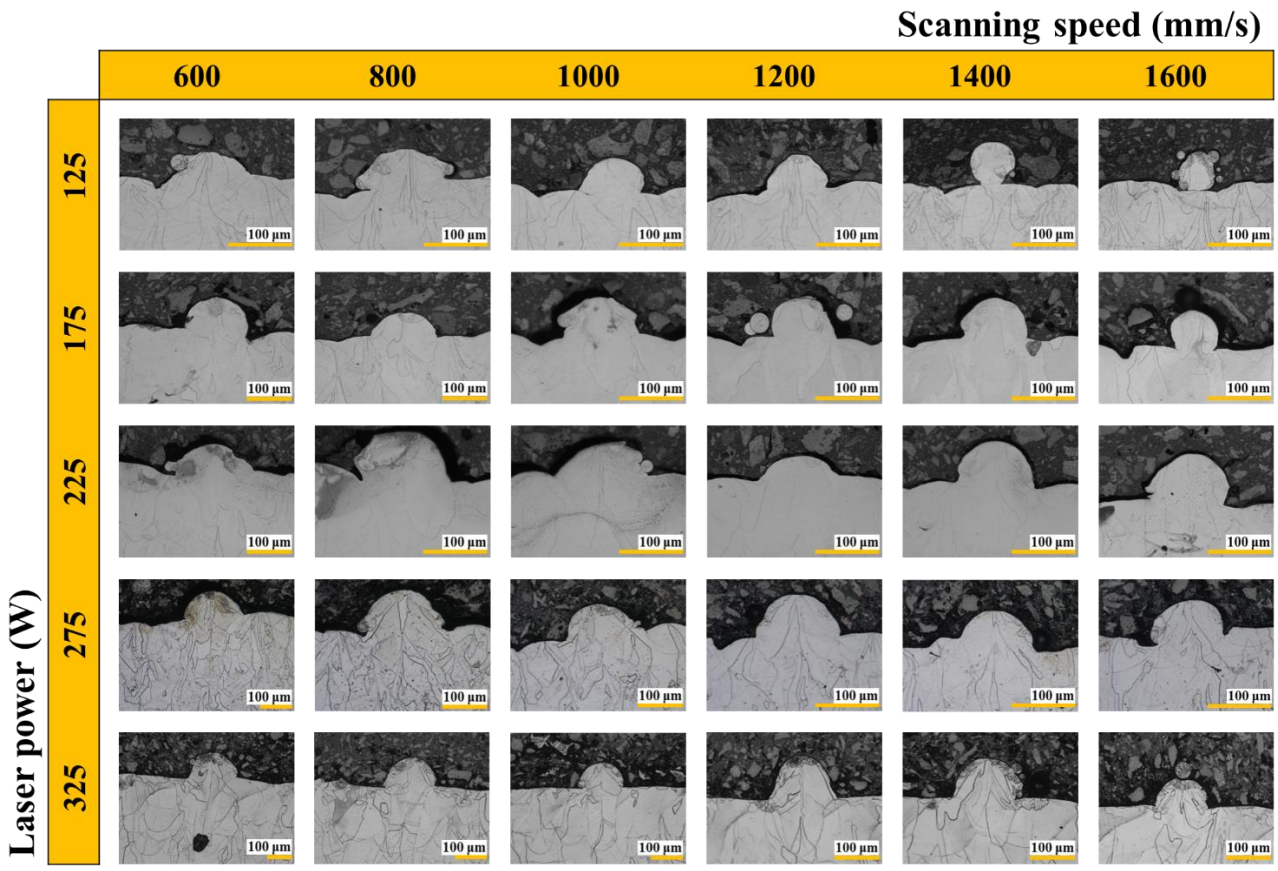

Figure 3-4: Microscopic images of the single-track's cross-section made by the laser powers ranging from 125 to 325 W and the scanning speeds ranging from 600 to 1600 mm/s.

Fig. 3-5a illustrates that increasing the scanning speed results in a reduction in melt pool depth for all laser powers. Additionally, it highlights that the effect of scanning speed on depth is more pronounced at higher laser powers, while the influence of laser power on depth is more significant at lower scanning speeds. Similarly, in Fig. 3-5b, the melt pool width decreases with increasing scanning speed. Therefore, increasing the laser power at a constant scanning speed, or reducing the scanning speed at a constant laser power, results in an increase in melt pool size. It is worth mentioning that the bead height was independent of the input laser power, scanning speed, and *VED* and no noticeable trend was observed. The reason behind this phenomenon is the presence of opposing effects on track bead formation. For instance, when input energy is low, a smaller amount of metal powder may melt, leading to a shorter bead height. Conversely, reduced input

energy can result in balling and humping, thereby increasing bead height. Guo et al. reported the same result for IN738LC superalloy single-track beads [68].

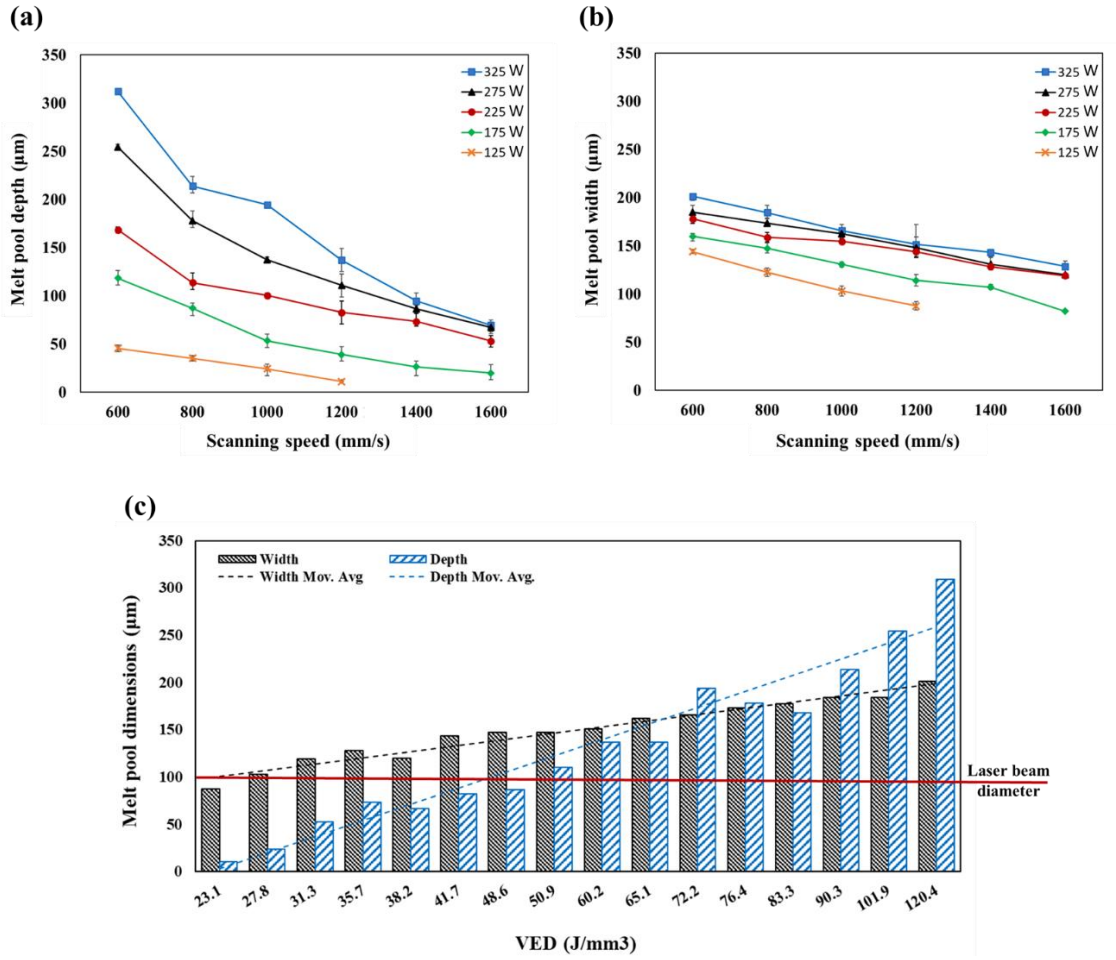

Figure 3-5: (a) Melt pool depth and (b) melt pool width, as a function of laser power and scanning speed. (c) Variation of melt pool dimensions with volumetric energy density.

Fig. 3-5c illustrates the variation of melt pool depth and melt pool width with *VED* value. It shows that while the *VED* grows from 23.2 J/mm^3 (P = 125W & v = 1600 mm/s) to 120.4 J/mm^3 (P = 325W & v = 600 mm/s), the melt pool depth increases from 11 ± 3 μm to 254 ± 9 μm and the melt pool width increases from 85 ± 11 μm to 194 ± 7 μm. The melt pool depth and width increase to around 243 μm (~ 22 times the lowest value) and 109 μm (~ 2 times the lowest value), respectively. Therefore, increasing the *VED* leads to a significantly higher growth rate for the melt pool depth

compared to its width. To show the melt pool growth rate, the moving average trendline has been applied for both the melt pool depth and the melt pool width as shown in Fig. 3-5c.

3.3.1.3 Effect of process conditions on melt pool size

The higher sensitivity of melt pool depth to the energy input can be attributed to the Gaussian distribution of the laser heat source. Given the Gaussian distribution of the laser beam, the intensity of laser radiation at the center of the laser beam is notably higher compared to the intensity at the beam edge [59,110]. Consequently, the melting of powder particles at the edge of the laser beam profile is less responsive to energy input changes compared to the center. As a result, the width of the melt pool is less sensitive to the input energy changes than the melt pool depth. Also, the high intensity at the center of the laser beam may cause an increase in the temperature of the melt pool to the boiling temperature. This leads to the vaporization of the molten metal which can result in a surface depression of the melt pool, which can induce pressure along the depth direction (recoil pressure) to increase melt pool penetration [111–113]. This usually occurs at high *VED* values (particularly with high laser power and low scanning speed) and shows greater sensitivity of the melt pool depth to the process parameters at higher laser powers and lower scanning speeds (Fig. 3-5a).

As shown in Fig. 3-5c, almost all the melt pool widths are larger than the laser beam diameter (100 μm). The reason for this is that during the LPBF process, each track can be created through two mechanisms, which can work independently or in combination. The first mechanism involves melting the powder directly through laser irradiation, primarily within the laser beam incident zone. The second mechanism involves melting nearby powder particles outside the laser beam incident zone through conduction, convection, and radiation, which transfer heat to adjacent particles. Since for moderate and high *VED* values, both mechanisms work together, it is expected that the width of the single-track melt pool would be wider than the laser beam diameter.

The contributions of laser power and scanning speed to single-track melt pool dimensions can be statistically estimated by the ANOVA table. Table 3-3 and Table 3-4 stand for two ANOVA summaries for analyzing the melt pool width and melt pool depth, respectively. These tables show the obtained sum of squares (SS), degree of freedom (df), mean squares (MS), F values, P-value,

and F_{crit} from the ANOVA study of melt pool dimensions for the 5 laser powers, 6 scanning speeds and 3 replications, at a 95% confidence interval.

It is seen that the F values for both laser power and scanning speed are much larger than their respective F critical values, meaning that both laser power and scanning speed significantly affect the width and depth of the melt pool (Table 3-3 and Table 3-4). To find the contribution of each parameter on melt pool dimensions separately, the SS associated with the parameters should be divided by the Total SS. While the impacts of laser power and scanning speed on melt pool width are nearly equal (46.2% and 48.6%, respectively), laser power has a more considerable influence on melt pool depth compared to scanning speed (53.7% and 37.9%, respectively). From a different point of view, it can be stated that the melt pool depth shows greater sensitivity to laser power (~1.4 times) than it does to scanning speed. This fact agrees with what has been revealed in Fig. 3-5c; wherein the slope of the depth moving average trendline is 2.6 times greater than the slope of the width moving average trendline.

Table 3-3: ANOVA table for the effect of laser power and scanning speed on melt pool width

Source of Variation	SS	df	MS	F	P-value	F crit
Laser power	57615.4	4	14403.8	214.8	0.0000	2.5
Scanning speed	56874.2	5	11374.8	169.6	0.0000	2.4
Interaction	4496.1	20	224.8	3.3	0.0000	1.7
Error	4023.3	60	67.1			
Total	123009	89				

Table 3-4: ANOVA table for the effect of laser power and scanning speed on melt pool depth

Source of Variation	SS	df	MS	F	P-value	F crit
Laser power	265273.8	4	66318.5	1438.7	0.0000	2.5
Scanning speed	192455.1	5	38491.1	834.9	0.0000	2.4
Interaction	48532.7	20	2426.6	52.6	0.0000	1.7
Error	2765.8	60	46.1			
Total	509027.5	89				

The dependence of melt pool geometry on the laser power and scanning speed can be combined with the Marangoni convection effect. Marangoni convection is a fluid flow phenomenon that occurs due to surface tension variations in a liquid when there is a gradient in temperature or concentration along the liquid's surface. During the LPBF process, the laser beam heats the powder bed locally, such that a large gradient is developed within the melted pool, whereas the surface tension of molten Ti-5553 changes as temperature changes [114]. The variation in surface tension creates a gradient that causes inward or outward fluid flow and affects the melt pool geometry [1,72,80,115].

The relationship between the LPBF process parameters and Marangoni convection is primarily influenced by how the parameters affect the temperature gradient in a material. Higher laser power results in a higher temperature at the center of the melt pool and consequently higher temperature gradient in the melt pool [116]. On the other hand, although a lower scanning speed increases the laser energy input, longer exposure times of the laser on each point of the powder bed provide more time for heat to diffuse away from the melt pool [71]. As a result, the temperature gradient between the hottest point of the melt pool and the surrounding cooler molten metal becomes gentler. Therefore, the impact of the laser power on the Marangoni convection is higher, compared to the effect of scanning speed.

If we assume that the direction of radial Marangoni flow is inward, it can be observed that the enhanced Marangoni fluid flow penetrates the melting material, leading to a deeper melt pool [117,118]. Consequently, increasing laser power enhances the Marangoni convection and laser energy input which both increase the melt pool depth. Conversely, decreasing the scanning speed primarily increases laser energy input and has a diminishing effect on Marangoni convection. This fact shows the stronger dependence of melt pool depth on laser power compared to scanning speed which agrees with the experimental measurements and statistical analysis.

The greater sensitivity of Marangoni flow to laser power, as opposed to scanning speed, is evident in the Marangoni number (M_a), which can be estimated using the following equation:

$$M_a = \frac{\Delta\gamma L}{\mu_d D_c} \tag{3-1}$$

where $\Delta\gamma$ represents the difference in surface tension within the Marangoni flow [N m], L refers to the length of the free surface, which in the context of a melt pool, is referred to as melt pool length [m], μ_d represents dynamic viscosity [Pa s], and D_c is the diffusion constant [1]. Based on Eq. 3-1, the Marangoni number is related to the length of the melt pool, which is the distance between the nose and tail of the melt pool when viewed from the top. Given that the melt pool length is geometrically related to the melt pool depth (with a deeper melt pool resulting in a longer melt pool), it can be concluded that the Marangoni number is associated with melt pool depth. Therefore, increasing laser power has a greater impact on raising L (melt pool length) and subsequently raising the Marangoni number compared to changes in scanning speed.

It should be noted that in some alloys the direction of Marangoni convection flow in the melt pool is outward and increasing the melt pool temperature gradient causes a wider melt pool, instead of deeper. In alloys where elements impart a high surface activity, the surface tension of the molten metal can be decreased notably, and this reduction may cause a change in the sign of the gradient of surface tension with temperature, leading to a reversal of the Marangoni convection flow direction [1,115,116].

The geometry of the single tracks, including track surface morphology and melt pool dimensions, was investigated under various process conditions. As mentioned earlier, certain processing parameters may result in undesired defects and pores in the fabricated structure. Therefore, to establish a more reliable process map, it is necessary to assess the density of printed parts under different process conditions.

3.3.2 Multi-layer density

Along with the single tracks, the 30 process parameters (P = 125 – 325 W & v = 600 – 1600 mm/s) were used for multi-layer printing. The cyclic process of heating, melting, cooling, and solidification that occurs during the deposition of a multi-layer can offer a valuable understanding of how a single track can influence various aspects of the 3D-printed structure quality, including density, surface roughness, microhardness, and the resulting microstructure [13,119–121]. The measured relative density of multi-layers at different process parameters can be seen in Fig. 3-6.

To assess the presence of porosity and determine the relative density of multi-layers, a 1 mm × 1 mm × 5 mm block was extracted from each multi-layer and used for CT scanning. Fig. 3-6a shows

the block and an X-ray computed tomography image that qualitatively displays uniformly distributed pores within the block.

The relative density of the printed multi-layer at different laser powers and scanning speeds is shown in Fig. 3-6b. The relative density of low *VED* samples which have low laser power (P = 125 W), and high scanning speed (v = 1600 mm/s) is considerably lower than the other parameters. The lack-of-fusion defects occurring in the discontinuous and unstable tracks cause a high level of porosity (about 10%) [64,122]. Also, when considering high *VED* parameters, particularly under conditions of low scanning speed (v = 600 mm/s), the relative density tends to be low. This situation is expected to result in the presence of keyhole defects within these samples [79,109]. Fig. 3-6b demonstrates that the highest density can be attained with moderate scanning speeds and relatively high laser powers (v = 1000 – 1400 mm/s and P = 225 – 325 W). In such samples, the presence of porosity is negligible, allowing for a density close to 100%.

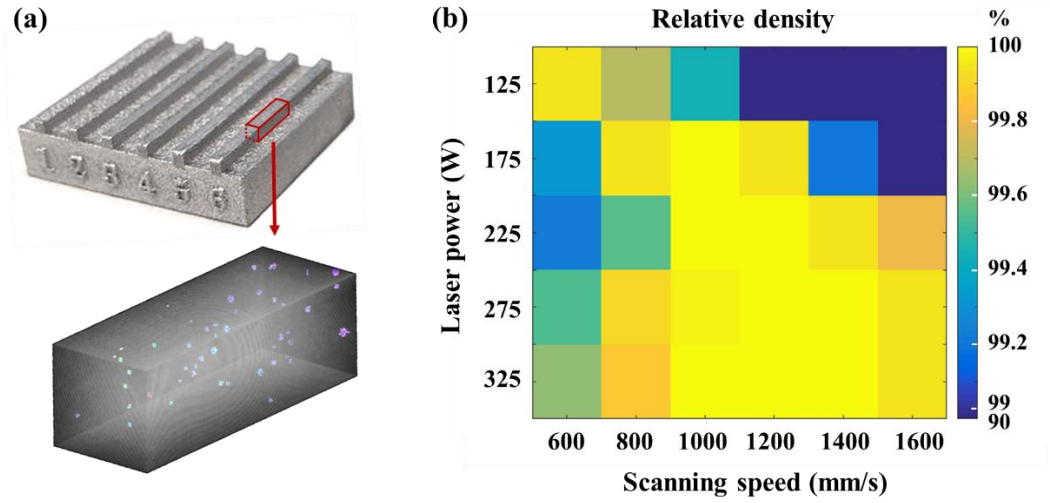

Figure 3-6: (a) 6 multi-layer tracks on a substrate and an X-ray computed tomography (CT) image showing pores distribution through a multi-layer. (b) Relative density of multi-layer structures at different conditions, measured by CT scanning.

3.3.3 Process map for LPBF of Ti-5553

The multi-layer structures were also cross-sectioned for microscopic investigation. Based on the micrographs from multi-layer structures, the measured relative density, single-track morphology, and melt pool geometry, the 30 combinations of laser power and scanning speed can be categorized into three groups according to melting modes: lack-of-fusion, conduction, and keyhole melting modes. Fig. 3-7 illustrates the track morphology, melt pool geometry, and multi-layer cross-section images of these melting modes.

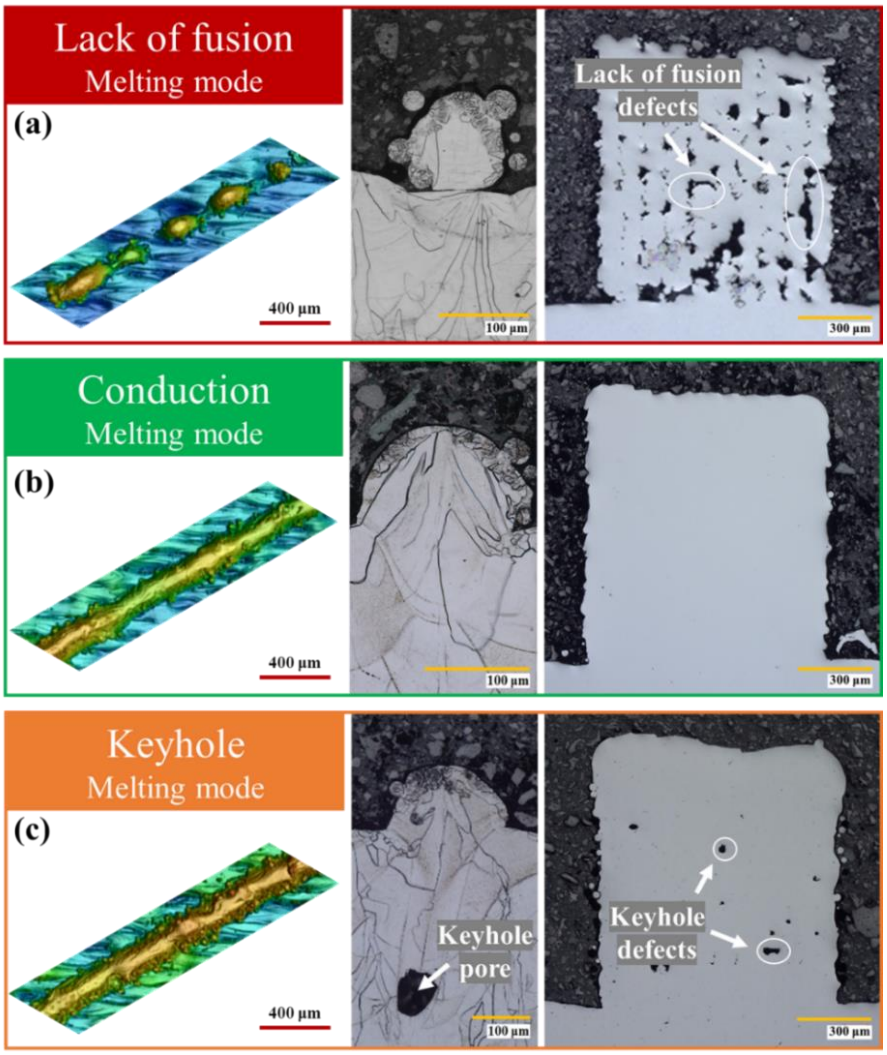

Figure 3-7: Track surface morphology, melt pool geometry and multi-layer cross-section images for 3 melting modes of (a) lack-of-fusion (P = 125 W & v = 1600 mm/s), (b) conduction (P = 325 W & v = 1200 mm/s), and (c) keyhole (P = 325 W & v = 600 mm/s).

In Fig. 3-7a, the lack-of-fusion defect is visible in the image of the multi-layer sample. The lack-of-fusion defect typically manifests as a distinct boundary between two adjacent tracks and/or layers of material where proper fusion did not occur, showing that either the laser energy is insufficient to fully melt the powder, or the scanning speed is too high, preventing proper fusion [63,123]. Although the lack-of-fusion defect shown in Fig. 3-7a arises from the presence of discontinuous tracks, it is worth noting that sometimes continuous tracks can also lead to this type of defect [22]. Fig. 3-8a and Fig. 3-8b schematically show how insufficient melt pool depth or melt pool width in the continuous tracks can induce lack-of-fusion defects.

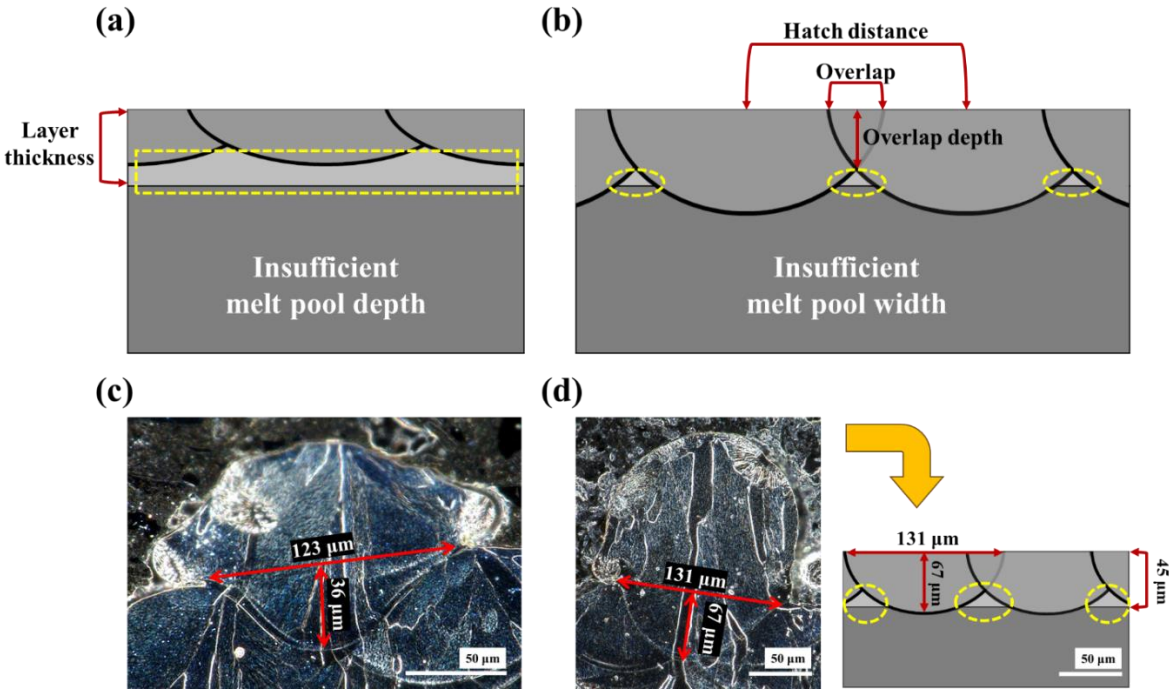

Figure 3-8: Schematic diagram of the melt pool sectional view illustrates how insufficient melt pool (a) depth and (b) width can result in a lack-of-fusion defect with unmelted powder particles shown by yellow dashed lines. (c) A melt pool with a depth less than layer thickness: P = 125 W & v = 800 mm/s. (d) A melt pool with a depth larger than layer thickness but insufficient width: P = 275 W & v = 1600 mm/s. The schematic diagram has the same scale.

When the melt pool depth is less than the layer thickness, the recently charged powder layer may not fully melt, and this can result in a distinct boundary between two adjacent layers (Fig. 3-8a). In this study, referring to Fig. 3-5, all the melt pools were created using process parameters of P = 125W & v = 800 to 1600 mm/s, and the melt pools were manufactured with parameters using P =

225W & v = 1600 mm/s and P = 225 W & v = 1400 mm/s have a depth less than layer thickness (45 μm). Consequently, the presence of a lack-of-fusion defect was expected before the printing of 3D multi-layer samples. As an example, Fig. 3-8c depicts a melt pool (P = 125W & v = 800 mm/s) with a depth of 36 μm, which is less than the layer thickness.

As shown in Fig. 3-8b, some powder particles between the boundaries of two adjacent melt pools and the previously solidified layer may remain unmelted (indicated by the yellow dashed lines), despite the melt pool depth being sufficiently large. This typically happens when the overlap depth is smaller than the layer thickness. Fig. 3-8d displays a melt pool created using process parameters of P = 275 W & v = 1600 mm/s, with a depth of 67 μm and width of 131 μm. It also schematically illustrates the melt pool conditions during printing, approximately to scale. This observation indicates that the formation of lack-of-fusion defects can be predicted before the printing of 3D parts.

In this work, the hatch distance has been assumed constant; however, reducing the hatch distance or increasing the overlap can sometimes mitigate this defect. Estimating melt pool dimensions through simulation would be highly valuable for mitigating lack-of-fusion defects in the LPBF process [22,87]. The shape of the lack-of-fusion defect is typically irregular and jagged [1,123]. In some cases, a sample with a lack-of-fusion melting mode may have some regular round shape defects. The formation of round-shaped pores is attributed to two main reasons: firstly, the trapped atmospheric gases within the molten pool which have no time to escape before solidification occurs, and secondly, the entrapped gas within powder particles during the gas atomization process [124,125]. During the lack-of-fusion melting mode, it should be noted that the melt pools are often very shallow or sometimes unmeasurable [9,22]. For instance, in Fig. 3-7a, the melt pool dimensions at various sections of the discontinuous and unstable single-track vary or cannot be measured due to the lack of contrast between the negligible melted layer and the prior layer.

Fig. 3-7c illustrates the keyhole defect in both the multi-layer sample and at the bottom of the single-track melt pool. When high *VED* process parameters are used, exceeding a certain limit of laser energy input can lead to the appearance of the keyhole defect and a shift into the keyhole melting mode. In this mode, the increased laser energy input significantly raises the temperature of the melt pool surface and nearby areas. The temperature can reach the metal boiling point, causing the metal to evaporate and generate recoil pressure that affects the melt pool, leading to

surface depression. In cases with higher energy input, increased metal vaporization can result in the formation of a narrow path called a keyhole channel. This newly formed channel enhances the laser's ability to penetrate the material, and the concurrent surface depression contributes to a greater depth for the molten pool. When the keyhole channel reaches a sufficient depth, small spherical voids can form upon solidification at the bottom of the channel, trapping traces of metal vapour. Marangoni convection and the movement of molten metal within the melt pool region prevent these trapped metal vapours (pores) from rising upward, causing them to remain in the solidified melt pool [71,79,109,111,112,126].

Fig. 3-7c illustrates the formed pore at the bottom of the single-track melt pool. In Fig. 3-7b, the multi-layer image illustrates the absence of visible defects or pores in the conduction melting mode, where a moderate *VED* value is used. In Fig. 3-6b, the relative density of this multi-layer (P = 325 W & v = 1200 mm/s) is reported to be nearly 100%, and no defects were observed with CT scanning either.

The conduction melting mode, which provides a fully dense part, is the desirable mode. However, a transition mode might occur between conduction and keyhole modes can be a suitable choice for LPBF manufacturing. When the process conditions are close to the conduction-keyhole threshold, either no pores are formed, or any small pores that do form may be eliminated by remelting during the next layer printing. This transient mode has negligible porosity and acceptable density, making it a good compromise between conduction and keyhole modes. Since higher laser energy can penetrate deeper, have multiple reflections in the vapour cavity of the keyhole channel, and transfer input energy more efficiently, the transition mode is preferred over the conduction mode [109,122,126,127].

As shown in Fig. 3-7, in the conduction melting mode, the shape of the single-track melt pool is bowl-shaped, with the width and depth dimensions closely resembling each other, while the keyhole single-track melt pool is goblet-shaped, and its depth is notably larger than its width. Tenbrock et al. reported that the melt pool depth-to-width ratio is typically around 0.8 at the threshold between the conduction mode and keyhole mode [64]. Although the keyhole melt pool is significantly deeper than the conduction melt pool, the width of the keyhole melt pool is slightly larger than that of the conduction melt pool. That is why the surface morphology of the keyhole single-track is not significantly wider than that of the conduction single-track (Fig. 3-7).

Fig. 3-9 shows the microscopic images of all the multi-layers under various conditions. In this figure, the mentioned groups of melting mode are represented by three different colours: red stands for the lack-of-fusion melting mode, amber stands for the keyhole melting mode, and green stands for the desirable conduction melting mode with a relative density exceeding 99.95%. The lack-of-fusion defect is prominently visible in the low *VED* multi-layers, with a laser power of 125 W (except for P = 125 W & v = 600 mm/s), and with a scanning speed of 1600 mm/s. On the other hand, keyhole pores are observed in several high *VED* multi-layers, such as those with parameters P = 325 W & v = 600 mm/s, P = 325 W & v = 800 mm/s, and P = 275 W & v = 600 mm/s. Multi-layers with moderate *VED* values that exhibit high relative density in Fig. 3-6 do not display any visible defects in their microscopic images, as shown in Fig. 3-9.

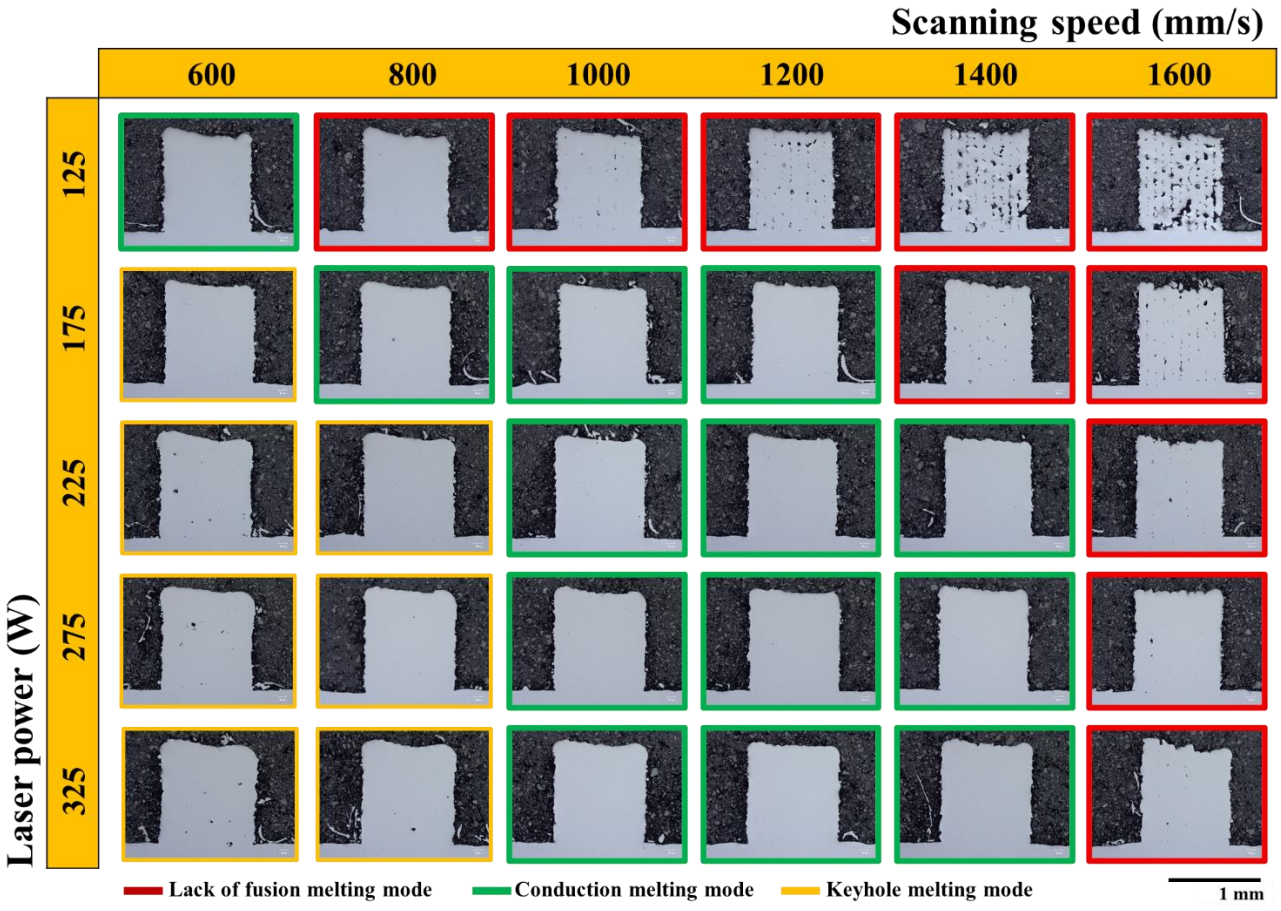

Figure 3-9: Microscopic images depict the cross-section of multi-layers under various process parameters, categorized into three groups based on their melting modes.

The map presented in Fig. 3-9 offers a reliable process map for the LPBF of Ti-5553. The proposed procedure can be used as a fast and cost-effective method for the optimization of the LPBF process for other alloys. Continuing from the current discussions, in the following sections, some of the most consequential process parameters will be examined to identify those most relevant to quality in manufacturing. An investigation into the effect of process parameters on the quality of manufacturing can provide the manufacturer with additional information from each set of process parameters for making informed decisions.

3.4 Conclusions

A comprehensive study on LPBF-made single-track and multi-layer samples was conducted to establish a process map and assess the impact of laser power and scanning speed on Ti-5553 printing quality. In addition to measuring the density of 3D-printed multi-layers, track surface morphology and melt pool geometry for each set of process parameters were thoroughly examined to ensure the reliability of the process map. The following conclusions can be drawn from the current experimental analysis:

1) Increasing the *VED* from 23.1 J/mm^3 to 120.4 J/mm^3 results in a notably greater growth rate for the melt pool depth, approximately 2.6 times higher than that of its width. This is because the Gaussian distribution of the laser heat source makes the melting of powder particles at the beam's center more responsive to energy variations compared to the edges.

2) The melt pool depth is more responsive to laser energy input at lower scanning speeds and higher laser power. At elevated *VED*s, the vaporization of molten metal results in a surface depression on top of the melt pool area. This depression subsequently creates a driving force in the direction of melt pool depth, ultimately leading to a deeper melt pool.

3) Based on the statistical analysis, while the impacts of laser power and scanning speed on melt pool width are nearly equal (46.2% and 48.6%, respectively), the melt pool depth demonstrates greater sensitivity to laser power than it does to scanning speed (53.7% and 37.9%, respectively).

4) Insufficient melt pool depth, where the melt pool depth is less than the layer thickness, and insufficient melt pool width, where the overlap depth of two adjacent tracks is smaller than the layer thickness, may cause a lack-of- fusion defects in a printed part.

5) In layer-by-layer manufacturing, horizontal and nearly horizontal grains provide additional randomly oriented nucleation sites for grains, disrupting columnar growth. When deeper melt pools are used, a greater extent of remelting occurs, leading to the removal of a higher percentage of horizontal and nearly horizontal grains. As a result, in printed parts with deep melt pools (higher *VED*), the thick columnar grains in the texture tend to become more elongated.

6) Choosing process conditions near the conduction-keyhole threshold can be effective since pores may not form or, if they do, they are small and can be eliminated during subsequent layers. This transition mode, with its ability to allow deeper laser penetration, multiple reflections in the keyhole channel, and efficient energy transfer, is sometimes preferred over the conduction mode.

Chapter 4

4 An Investigation into the Effect of Process Parameters on the Quality of LPBF-made Part

4.1 Introduction

Continuing from the discussions in Chapter 3 regarding LPBF process optimization, in this chapter, some of the most consequential process parameters will be examined to identify those most relevant to quality in manufacturing. An investigation into the effect of process parameters on the printed part properties, such as mechanical behaviour and surface roughness, can provide the manufacturer with additional information from each set of process parameters for making more precise choices. For instance, a comparison between the mechanical behaviour of two optimized parameters shows a decrease in strength of only ~3.5%, resulting in a significant increase of ~65% in ductility. Furthermore, the achievements of this research can help a manufacturer to tailor the process for different applications. For instance, the melt pool size and the stronger effect of laser power on melt pool depth can be employed to increase layer thickness, resulting in faster production. Additionally, these results can be used to mitigate the occurrence of the lack-of- fusion defects and for melt pool engineering.

It should be noted that using the multi-layers (with a cross-sectional area of 1×1 mm) instead of 3D cubes helps create a more confident connection between single-track and multiple tracks in a 3D part. This is particularly important because phenomena like heat accumulation during 3D part printing can lead to unexpected changes in this context. Additionally, the small size of the multi-layer approach has rendered this method relatively quicker and more cost-effective.

In the following sections, the impact of laser power and scanning speed on the microstructure of the melt pool and the corresponding multi-layer will be examined. Additionally, the surface roughness, stress-strain behaviour, and microhardness of LPBF-made samples under various conditions will be discussed.

4.2 Result and discussion

4.2.1 Microstructure formation

To conduct the microstructure investigation, two sets of process parameters were chosen: one from the conduction mode (P = 275 W & v = 1000 mm/s) and the other from the keyhole mode (P = 325W & v = 800 mm/s). Fig. 4-1 presents the results of the microscopic analysis for single-track and multi-layer samples under the mentioned specified conditions. Since the presence of pores can change the thermal conditions and disrupt the solidification process, both multi-layer samples were selected from those with relatively high density [128].

Fig. 4-1a illustrates the EBSD inverse pole figure (IPF) map of a deep single-track melt pool, with process parameters of P = 325 W & v = 800 mm/s. As discussed in the preceding sections, the boundaries of the melt pool were found from SEM images of etched samples. Fig. 4-1a also shows the microscopic image of the etched melt pool to demonstrate the process of finding the melt pool boundary. The width and depth of the melt pool are 184 μm and 238 μm, respectively, resulting in a depth-over-width ratio of 1.3. Since Tenbrock et al. [64] defined a melt pool with an aspect ratio above 0.8 as likely to be in the keyhole mode of melting, the 1.3 ratio places it within the category of keyhole melt pools. A bowl-shaped melt pool created using parameters of P = 275 W & v = 1000 mm/s can be seen in Fig. 4-1c. Although the depth-over-width ratio of this melt pool (0.78) is close to the mentioned threshold, Fig. 9 illustrates that this set of process parameters indicates a conduction melting mode for the melt pool.

It has been reported often in the literature that the directions of thermal gradient and heat flux at the fusion line (solidification front) are normal to the fusion line. Consequently, the direction of grain growth (solidification) is normal to the fusion line [9,12,71,129,130]. Since at the beginning of solidification, the fusion line aligns with the melt pool boundary, it can be said that grain growth initiates perpendicular to the melt pool boundary. This fact can be seen clearly in both melt pools in Fig. 4-1a and Fig. 4-1c. The grains tend to grow from the melt pool boundary toward the center of the melt pool, which is typical of solidified structures based on the heat flow direction [130,131].

In the middle part of a deep goblet-shaped melt pool, the melt pool boundary is almost vertical. As the grain growth direction is perpendicular to the melt pool boundary, all the grains in this region

are horizontal. In the keyhole melt pool of Fig. 4-1a, these horizontal grains have been marked. Conversely, at the bottom of the melt pool, where the melt pool boundary is almost horizontal, the grains grow toward the top of the melt pool, vertically due to heat flow resulting from accelerated final cooling at the surface. These thin vertical grains (marked in Fig. 4-1a and Fig. 4-1c) are present on the centreline of the melt pools, regardless of their shape. As the multi-layer samples were manufactured by the stripe scanning strategy without rotation (X-scan) and the tracks were deposited layer by layer on top of each other, the vertical grains can grow epitaxially through the layers and form very thin columnar grains parallel to the build direction. A very thin columnar grain has been marked with a yellow rectangle, in the multi-layer IPF map of Fig. 4-1d.

In LPBF of Ti-alloys, the high G/R ratio suggests a preference for columnar growth, which is reported in the literature as the dominant mode of microstructure evolution [128,130,132]. The columnar grain structure can be seen clearly in Fig. 4-1b and Fig. 4-1d. The schematic outlines of the melt pools are shown at their actual size and have been inserted in the multi-layer IPF map in Fig. 4-1b. The centerline of the melt pools which aligns with the very thin grain, has been represented using a white dashed line. The distance between the melt pools can be determined by measuring the distance between the very thin grains (centerlines), which is equal to the hatch distance. As mentioned in the sample fabrication section, each multi-layer consists of 10 tracks, with a hatch distance of 100 μm. These tracks are marked in Fig. 4-1b.

As shown in Fig. 4-1b and Fig. 4-1d, the multi-layer sample with the deeper melt pool (higher *VED*) has a coarser grain structure. The average grain size for the higher *VED* multi-layer (90.2 J/mm^3) with process parameters of P = 325 W & v = 800 mm/s is 61.3 μm, while this value for the multi-layer with lower *VED* (65.1 J/mm^3) and process parameters of P = 275 W & v = 1000 mm/s is 46.8 μm. It should be mentioned that the fine grains and attached droplets on the left and right sides of the multi-layers were excluded from the grain size analysis.

In addition to the very thin columnar grain, a thick columnar grain has been marked in Fig. 4-1d. By comparing Fig. 4-1b and Fig. 4-1d, it can be said that a greater area of the higher *VED* multi-layer is occupied by thick columnar grains when compared to the lower *VED* multi-layer. The reason for the presence of longer thick columnar grains in the higher *VED* sample is the deeper remelting during the melting process of the subsequent layer. During layer-by-layer manufacturing, horizontal grains and grains that are nearly horizontal and inclined upward can

provide additional randomly oriented nucleation sites for grains, disrupting columnar growth. Some of these grains are eliminated during the remelting process, while others persist depending on their position and growth direction [9,26]. Deeper melt pools, such as the one shown in Fig. 4-1a, lead to greater remelting, removing a higher percentage of horizontal and nearly horizontal grains. Therefore, the thick columnar grains in the texture of a printed part with a deep melt pool (higher *VED*) tend to be more elongated. It is worth noting that the lower quarter of all the multi-layers has similar finer grains, which result from the influence of the substrate's grain structure and can be ignored in the grain structure analysis of the multi-layers.

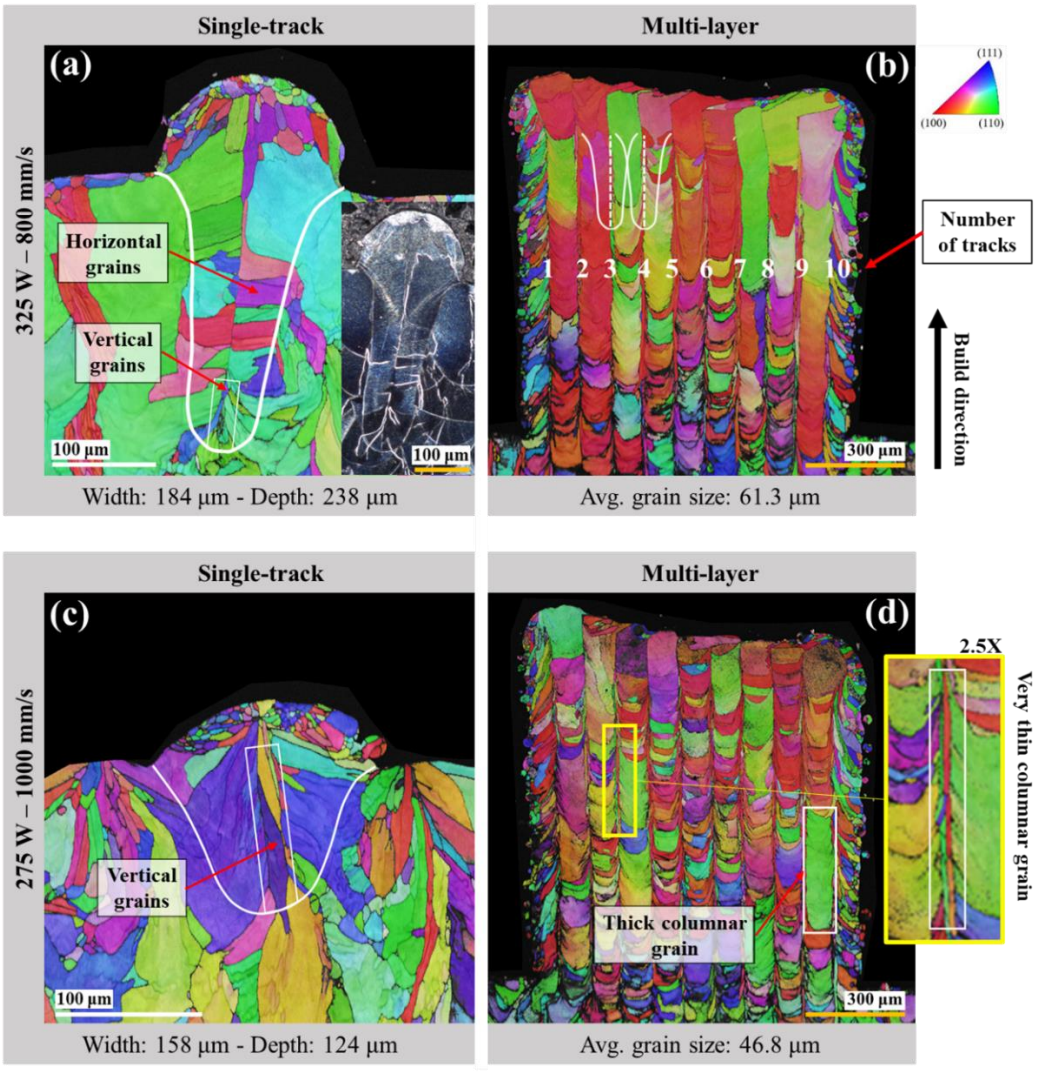

Figure 4-1: EBSD IPF-Z map of single-track and multi-layer samples with process parameters of (a)(b) P = 325 W & v = 800 mm/s and (c)(d) P = 275 W & v = 1000 mm/s, respectively.

It is observed in Fig. 4-1a and Fig. 4-1c that the grains in the melt pool grew epitaxially from the substrate grains that are located near the melt pool boundary. In addition to the columnar grains growing from the parent grains at the melt pool boundary, some grains near the center of the melt pool appear detached from the melt pool boundary. These small grains are also columnar and grow toward the center of the melt pool [100,101]. As mentioned above, the G/R ratio in LPBF of Ti-alloy is exceedingly high, consequently, the formation of equiaxed grains is not expected in these melt pools [128,132]. Microstructure evaluation in the track bead is more complicated. The lower half of the track bead microstructure is influenced by the grains from the upper region within the melt pool, and the microstructure of the upper half of the bead is affected by spatter, droplets, and airflow. The fine grains formed inside the track bead are typically a result of an increased number of nucleation sites created by these spatters and droplets [59].

Regarding the phase metallurgy of Ti-5553, it should be noted that this β-metastable alloy consists primarily of the β phase with some α phase. In this alloy, β-stabilizing elements such as V, Mo, Cr, and Fe strongly inhibit the formation of the α phase from the primary β phase, particularly when the cooling rate is extremely high, and diffusion time is limited [4,52,133]. In β-Ti alloys, the α phase can develop through two distinct processes: one occurs during gradual cooling from a temperature higher than β-transus temperature (860±10 °C), while the other takes place during isothermal heat treatment (aging) below the β-transus temperature [5,133]. Based on this fact, due to the typically super-fast cooling in the LPBF process, in as-printed Ti-5553 material, either there is no α phase, or it exists in exceptionally low amounts. In the current study, the XRD patterns of the two different samples are presented in Fig. 4-3a, confirming the presence of both β and α phases, with different amounts of α phase. This result and its effect on mechanical properties will be discussed in the “Mechanical behaviour” section.

4.2.2 Mechanical behaviour

4.2.2.1 Tensile strength

Three sets of process parameters were selected from the conduction melting mode region. Sample #1 with process parameters of P = 325 W & v = 1000 mm/s has a relatively high *VED* value of 72 J/mm^3, while samples #2 and #3 both have similar moderate *VED* values of ~50 J/mm^3. Sample #2 was processed with parameters P = 325 W & v = 1400 mm/s, which has a scanning speed

approximately 40% higher than that of sample #1. On the other hand, sample #3 was processed with parameters P = 225 W & v = 1000 mm/s, having a laser power nearly 40% lower than that of sample #1 (Fig. 4-2a).

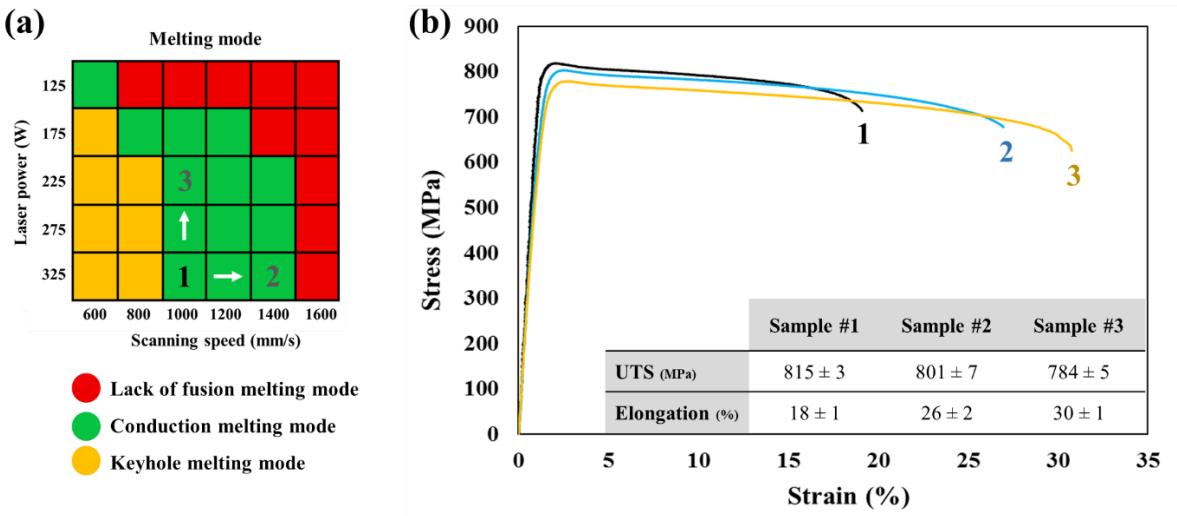

Figure 4-2: (a) Melting mode map and the corresponding process parameters for the selected samples on the map. (b) Engineering stress-strain curves of 3 selected samples from conduction melting mode. Sample #1 has a relatively high *VED* (P = 325 W & v = 1000 mm/s), while samples #2 (P = 325 W & v = 1400 mm/s) and #3 (P = 225 W & v = 1000 mm/s) both have similar moderate *VED* values.

Fig. 4-2b shows the engineering stress-strain curves of the 3 selected samples. It reveals the strength of all 3 samples is nearly the same, although the strength of sample #1 (815 ± 3 MPa) is greater than that of sample #2 (801 ± 7 MPa), which are both slightly stronger than sample #3 (784 ± 5 MPa). Regarding the ductility, the elongations of samples #3 and #2 are comparable, and significantly greater than that of sample #1. The elongations of samples #3, #2, and #1 are 18 ± 1%, 26 ± 2%, and 30 ± 1%, respectively, showing an inverse trend compared to their strength values. It is worth mentioning that the strength and the range of elongation in Ti-5553 alloys produced using conventional methods have been reported to be approximately 1200 MPa and 5-15%, respectively [36,57,62]. However, for the as-printed Ti-5553, the reported strength and elongation in the literature are about 780 MPa and 30%, respectively [5,17].

To discuss the mechanical behaviour, it is necessary to investigate the phase metallurgy, hence samples #1 and #3 which have more significant differences were chosen for the XRD test. Fig. 4-3a shows the XRD patterns of samples #1 and #3 which confirm the presence of mainly β and some α phase in both samples. It can be concluded that sample #1 contains a higher proportion of the α phase, as evidenced by the slightly higher α peaks observed in its pattern compared to sample #3. The calculated volumetric portion of α phase in sample #3 is 6.8%, while sample #1 has about 16% α phase. It should be noted the amount of α phase in as-received powder is very low and almost negligible. Fig. 4-3b presents the EBSD grain analysis for these three samples, revealing average grain sizes of 118.4 μm, 96.1 μm, and 67.9 μm for samples #1, #2, and #3, respectively. Samples #2 and #3 have almost the same melt pool geometry but exhibit different grain sizes. This observation is not contradictory to the information provided in the "Microstructure formation" section, as the x-scan scanning strategy was used for the multi-layer fabrication, while the tensile specimens were created with the XY-scan scanning strategy.

Based on the higher fraction of α phase shown for sample #1 in Fig. 4-3a, it can be concluded that the primary mechanism responsible for enhancing strength is precipitation strengthening. This is consistent with the higher strength reported as the proportion of the α phase increases in these beta-stabilized titanium alloys [5,133]. The process of heat treatment precipitation of the α phase has been shown to lead to a considerable increase in strength in this material, along with a corresponding decrease in ductility observed here between samples #1 to #3 [134].

The heat accumulation from the cyclic heating and cooling during part printing may facilitate elemental diffusion and in-situ ageing heat treatment which promotes the diffusion of α-stabilizing elements like Al to form the α phase [5,133]. This phenomenon is expected to occur more in the higher energy process parameters because they can produce higher temperatures and can maintain these elevated temperatures over a wider range of time and depth within the part. Therefore, the α phase can be formed in the as-printed tested samples, although in the high VED sample #1, which has a deeper and hotter melt pool promoting a higher amount of α phase.

The small-sized and dispersed α phase particles produce a high number of α/β interfaces that act as dislocation barriers. When dislocation movement is hindered, it becomes more difficult for the material to deform plastically, leading to an increase in strength and usually a reduction in ductility and elongation [5,53,133,134]. Therefore, higher strength and lower ductility are expected for

sample#1 which has slightly more α phase. It should be noted the trade-off of achieving higher strength is a decrease in ductility [53]. This reverse relationship between tensile strength and total elongation of β Ti-alloys such as Ti-5553 has been also reported by Zhu et al. [135].

An additional notable finding evident in the stress-strain diagrams depicted in Fig. 4-2b is the absence of strain hardening. The minimal strain hardening typically observed in materials with a BCC crystal structure is anticipated to result from a low dislocation density [136].

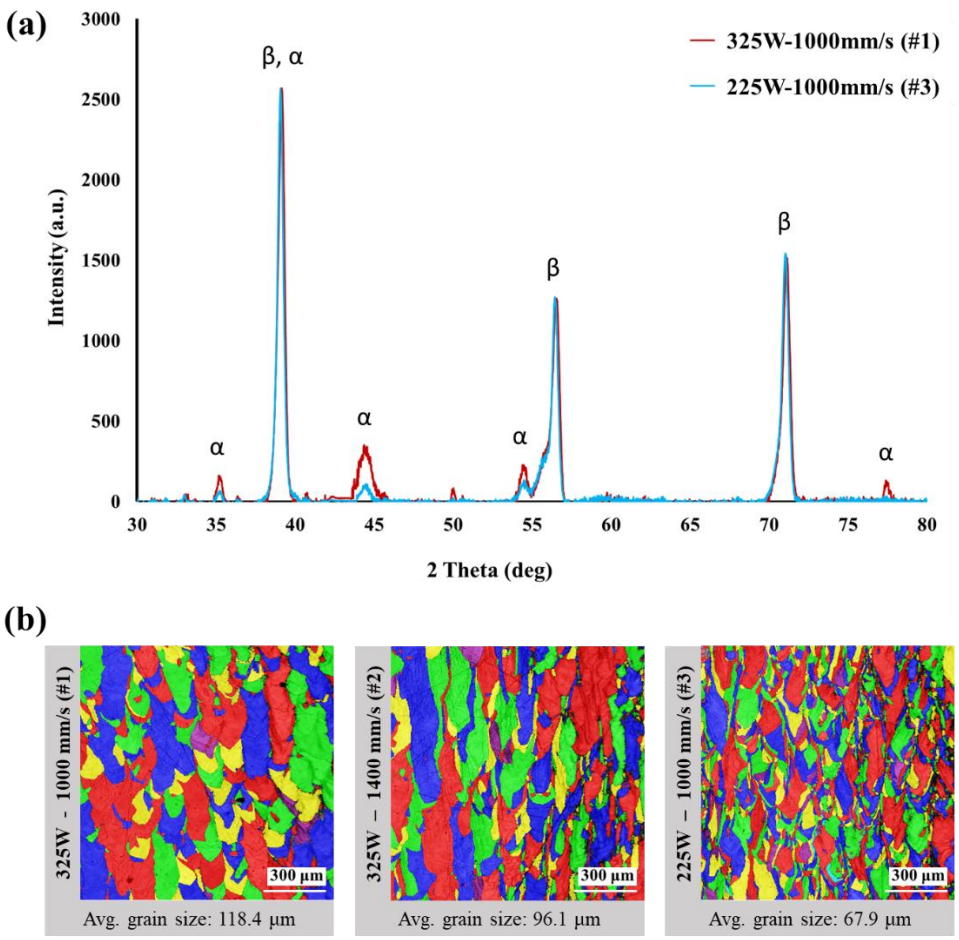

Figure 4-3: (a) XRD patterns of sample #1 (P = 325 W & v = 1000 mm/s) and sample #3 (P = 225 W & v = 1000 mm/s). It confirms a higher presence of α phases in sample #1 compared to sample #3. (b) EBSD grain analysis of sample #1, sample #2 (P = 325 W & v = 1400 mm/s), and sample #3.

Panza-Gios et al. [50], have investigated the effects of grain size on the strength of Ti-5553, described by the Hall-Petch relation. The Hall-Petch equation shows a linear relationship between the grain size and the yield strength, as follows:

$$\sigma_Y = \sigma_1 + K\, D^{-\frac{1}{2}} \quad (4\text{-}1)$$

where σ_Y is yield strength [MPa], σ_1 is friction stress (a material constant related to the resistance of the crystal lattice to dislocation movements) [MPa], K is strengthening coefficient [MPa $mm^{-0.5}$], and D is the average grain size [mm]. The reported values of σ_1 and k for Ti-5553 are 736 MPa and 17.9 MPa $mm^{-0.5}$, respectively [50]. Based on Eq. 4-1, a small value of the strengthening coefficient compared to the large value of σ_1 indicates a weak dependence of the strength on grain size, especially when the differences in grain sizes are not significant.

When comparing sample #1 to samples #2 and #3, a decrease in strength of only approximately 1.5% and 3.5%, respectively, results in a significant increase in their ductility, with approximately 45% and 65% improvements observed, respectively. In this research, along with the effect of grain size, the size, morphology, volume fraction, and distribution of the formed α phase may be such that their effect on elongation is more significant than their effect on strength. While further comprehensive investigations are needed to fully understand the details of α phase formation, the current results provide valuable insights into the mechanical behaviour of parts produced with the desired process parameters. This information aids manufacturers in making more educated decisions about fabrication.

4.2.2.2 Microhardness

Another test that can demonstrate the mechanical behaviour of printed parts under various process parameters is the hardness test. Fig. 4-4 shows the result of the microhardness measurement under various conditions for the multi-layers. The optical microscopy image in Fig. 4-4a displays a microhardness indentation map of a multi-layer structure. Out of a total of 80 indents, 72 are situated within the multi-layer, while the remaining 8 are within the substrate. In Fig. 4-5b, the average Vickers microhardness, based on 72 analyzed indents for each set of conditions, has been plotted.

The highest and lowest hardness are, respectively, observed in the specimens printed with probably the highest and lowest *VED* values, although the range of hardness is not very wide. The samples created with process parameters of P = 325 W & v = 800 mm/s and P = 125 W & v = 1600 mm/s exhibit the highest hardness of 318 HV and the lowest hardness of 300 HV, respectively, whereas the average measured hardness of the substrate is 311 HV. The same to the above-mentioned discussion about the tensile strength, the hardness can be attributed to the formation of α phase [5,133]. The printed samples with higher energy input contain more α precipitates, leading to higher hardness due to precipitation hardening.

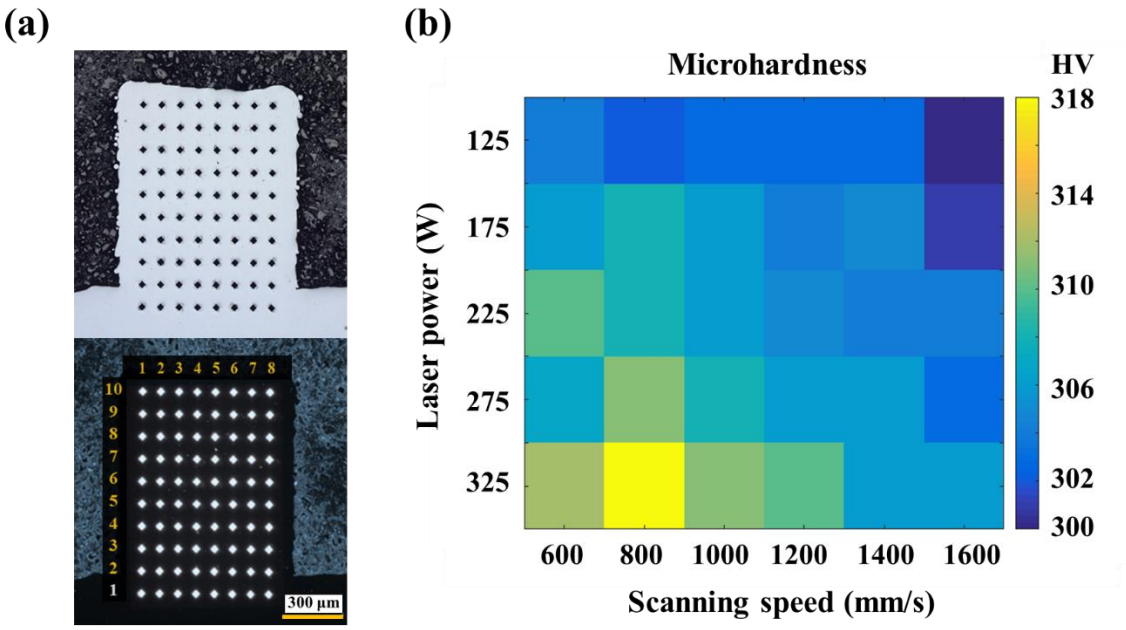

Figure 4-4: (a) OM image of the microhardness indentation map on a multi-layer. (b)Vickers microhardness of the multi-layers at different conditions, utilizing an average of 72 indents for each set of conditions.

To improve measurement accuracy, indents placed on visible lack-of-fusion and keyhole defects, or those located within 50 µm of the defects, have been excluded from the average hardness calculation. It is important to note that despite their exclusion, the non-negligible detrimental effect of these defects on the hardness of their surrounding areas persists. This fact may explain why samples manufactured with process parameters of P = 325 W & v = 600 mm/s and P = 275 W & v = 600 mm/s exhibit lower hardness than expected.

The microstructure formation and its effect on the mechanical behaviour of LPBF-made Ti-5553 were discussed. One of the other crucial aspects of manufacturing quality is surface roughness, as it is critical in controlling some mechanical properties such as fatigue [25]. Hence, in the following section, the surface roughness of multi-layer samples will be examined.

4.2.3 Surface roughness

The diagram in Fig. 4-5a depicts the surface roughness of multi-layered samples produced with various laser powers and scanning speeds. In this diagram, Ra is referred to the arithmetic average of the profile heights (absolute value), along the evaluation length [121]. The surface roughness was evaluated over 30 lines, from the top surface of the multi-layers. As shown in Fig. 4-5a, the highest roughness occurs in samples where there is a lack-of-fusion melting mode, while the surface roughness of multi-layered specimens with conduction and keyhole melting modes is considerably lower.

Fig. 4-5a shows that surface roughness has a stronger dependence on scanning speed changes compared to the laser power values examined. At a constant laser power, this figure illustrates an average surface roughness difference of 12.1 μm between samples with the lowest and highest scanning speeds. Conversely, at a fixed scanning speed, the average surface roughness difference between samples with the lowest and highest laser power is 7.6 μm. As shown in Fig. 4-5a, the lowest surface roughness values can be seen at lower scanning speeds such as 600, 800, and 1000 mm/s, while the highest roughness is associated with samples produced using higher scanning speeds.

Fig. 4-5b shows micrographs of the cross-section of the multi-layered samples produced with the highest scanning speed of 1600 mm/s and laser powers ranging from 125 W to 325 W. These images reveal the multi-layers with high scanning speed have a rough surface, even when the laser power is high enough (325 W) to provide high density. According to Fig. 4-5b, it is noteworthy that the sample with a laser power of 325 W and a high scanning speed of 1400 mm/s has a relatively high surface roughness (16.8 μm), while, referring to Fig. 6b, its density is almost 100%. Considering this point, if the goal is to obtain a fully dense LPBF-made part with favourable surface roughness, P = 325 W & v = 1400 mm/s may not be the optimal choice, despite providing a high-density structure.

The discontinuous or unstable tracks with high width variation along their length are the main reasons that a higher scanning speed is associated with higher surface roughness. By increasing the scanning speed, the LPBF tracks start to fluctuate and tend to break up. This instability can cause the molten pool surface to become uneven, leading to irregularities in the solidified layers. There are some potential factors contributing to the track instability during the melt flow process, such as the Plateau-Rayleigh instability [68,137]. The Plateau-Rayleigh instability specifically deals with the fragmentation and breakup of thin molten metal into smaller droplets because of surface tension. This instability occurs when the ratio of molten metal thickness to its length is larger than a specific value and the solidification is fast enough [116,138]. As increasing the scanning speed provides a narrower melt pool and faster solidification, the mentioned unstable tracks appear at higher scanning speeds and build rougher surfaces.

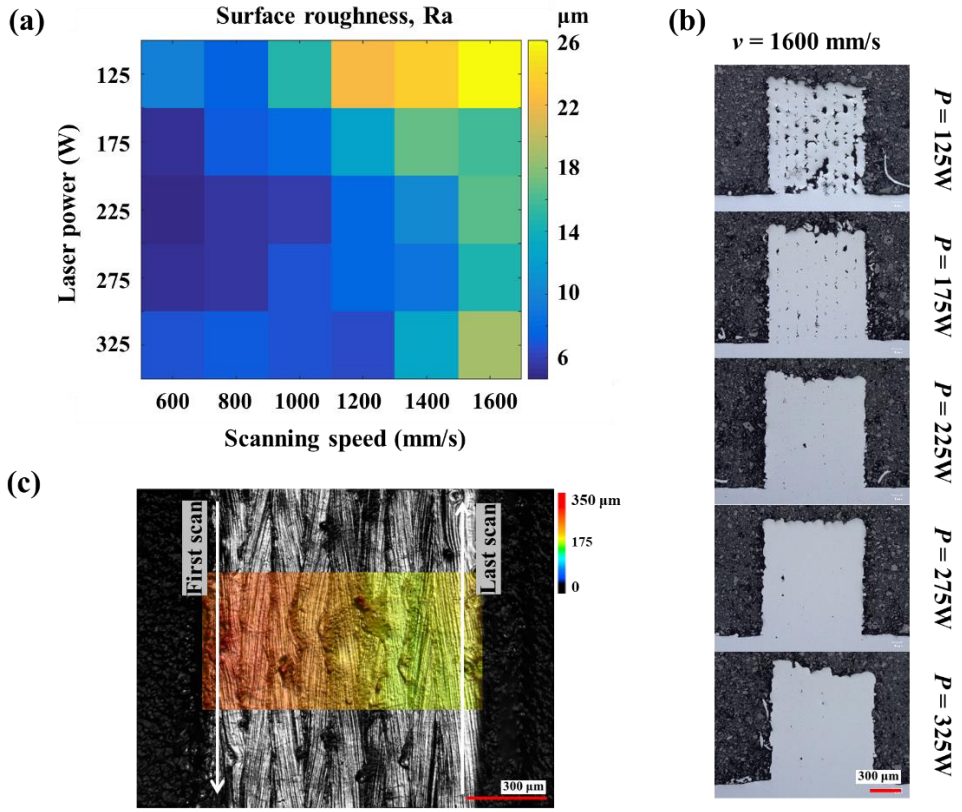

Figure 4-5: (a) Surface roughness of multi-layers under various conditions. (b) Microscopic images from the cross-sectioned multi-layers with a scanning speed of 1600 mm/s. (c) Surface morphology: a top view of a multi-layer.

The other point that can be found in the investigation of multi-layer surfaces is a phenomenon known as “denudation”. Denudation refers to the interaction between the laser and powder in which powder is removed from around a track during the laser scanning [139]. The denudation under normal atmospheric pressure occurs due to the rapid evaporation of metal vapour from the melted pool. This evaporation leads to an inward movement of the surrounding gas toward the molten track, driven by the Bernoulli effect. This inward gas movement is powerful enough to capture powder particles, which might be integrated into the melted pool or expelled alongside the metal vapour [110,140]. Denudation can drastically affect the final surface morphology, especially for thin parts like multi-layers [104].

Fig. 4-5c illustrates the top view of a multi-layer and its surface morphology. It shows the height of the surface has been decreased from left to right. The first scan built a higher surface compared to the last scan, which is attributed to denudation. The first track had enough powder particles around itself to build a complete structure, while due to denudation, subsequent tracks had progressively fewer metal powder particles in their vicinity. Hence, a gentle slope is observable on the upper surface of the multi-layer samples (Fig. 4-5c). It should be mentioned that in the manufacturing of the multi-layer samples, the contour was applied. As a result, the first and last tracks underwent an additional scan, which is why they exhibited a slight duplicated bump.

To express the extent of denudation, the denudation width phrase is used. Amiri et al. [141] conducted an experimental and analytical investigation into the impact of laser power and scanning speed on denudation width. They reported that, for a given laser power, the denudation width expands with a reduction in scanning speed, while this value reaches a plateau by increasing in laser power, at a fixed scanning speed [141]. In Fig. 9, a clear trend can be observed for changes in scanning speed: as the scanning speed increases, the slope of the upper surface decreases. However, when it comes to changes in laser power, no specific patterns can be discerned from the multi-layer cross-section images.

In the current research, the LPBF-made single-tracks, along with printed multi-layers were studied systematically to find the optimal process parameters and explore the effect of these parameters on the properties of the printed Ti-5553. Based on the mentioned result and discussion, a manufacturer can select suitable process parameters from the available full-dense options according to the application and required properties of an LPBF-made part. For example, the

sample printed with parameters of P = 325 W & v = 1000 mm/s exhibits high strength, high hardness, and suitable surface roughness but has low ductility. On the other hand, the printed sample using P = 325 W & v = 1400 mm/s has significantly higher ductility but slightly lower strength and hardness. Adding to this, the sample printed at P = 325 W & v = 1400 mm/s has high surface roughness, whereas the printed sample with P = 225 W & v = 1000 mm/s, while maintaining consistent mechanical properties, provides much lower surface roughness. It should be noted that significant differences in properties, such as elongation and surface roughness, between two samples with the same *VED* values indicate that *VED* alone is insufficient as a design parameter [142].

4.3 Conclusions

After an in-depth single-track to multi-layer study to identify a reliable process map, the effects of the significant process parameters on the properties of the printed parts were investigated. Since each set of process parameters within the desirable process window has its unique properties and qualities, supplementary examinations, including microstructure evaluation and mechanical behaviour testing, were also conducted on them. This comprehensive study provides manufacturers with precise and diverse options tailored to their specific applications and product requirements. The following conclusions can be drawn from the current experimental analysis:

1) In layer-by-layer manufacturing, horizontal and nearly horizontal grains provide additional randomly oriented nucleation sites for grains, disrupting columnar growth. When deeper melt pools are used, a greater extent of remelting occurs, leading to the removal of a higher percentage of horizontal and nearly horizontal grains. As a result, in printed parts with deep melt pools (higher VED), the thick columnar grains tend to become further elongated.

2) In the high *VED* sample, characterized by deeper and hotter melt pools, the α phase content is higher, resulting in increased strength and hardness, and decreased ductility.

3) The trade-off for achieving higher ductility involves a slight decrease in strength. When comparing the high *VED* (72 J/mm3) sample to the moderate *VED* (~50 J/mm3) samples,

there is a significant increase in ductility by 45% (or 65%), correlated with a slight decrease in strength of only approximately 1.5% (or 3.5%).

4) The surface roughness has a stronger dependence on scanning speed changes compared to the laser power changes. The multi-layers created at high scanning speeds exhibit rough surfaces, even when the laser power is set to a sufficient level (325 W) to ensure high density.

5) The notable variations in properties observed between two samples with the same *VED* indicate that *VED* alone is not sufficient as a design parameter and the main process parameters, such as laser power and scanning speed, should be considered separately.

Chapter 5

5 Numerical Modelling for LPBF Process with a Novel Hybrid Heat Source Model

5.1 Introduction

Additive manufacturing (AM) is an advanced fabricating method utilized to build near-net-shape parts by depositing material based on a digital model [2,7]. Among AM methods, Laser Powder Bed Fusion (LPBF) is considered a feasible and high-resolution fabrication method for producing metallic parts with tailored properties. However, this novel manufacturing method involves many independent parameters, which pose a challenge to achieving desired properties without a proper physical understanding of the process [1,8,59,143]. The LPBF process parameters, particularly the laser power and speed, affect the melting and solidification condition of the molten metal powders and control the microstructures, and consequently mechanical behaviours [13,14]. Hence, achieving the desired properties may necessitate correlating the process parameters with melting and solidification conditions [102,103,144,145].

To study the correlation between process conditions and melt pool solidification a deep understanding of thermal outputs including temperature gradient and cooling rate is required; however, it is extremely challenging to experimentally measure thermal variables at rapid solidification conditions and small length scales with the current hardware and software [21,82,120]. Finite Element (FE) methods are one of the fastest and most efficient numerical methods to perform thermal analysis for LPBF-made 3D parts. Over the last decade, the FE method has been extensively used for LPBF modelling by many researchers due to the capability of FE to model different laser heat source profiles [74–77]. Promoppatum et al. [20] developed an FE model with a Gaussian 2D heat source model to investigate the temperature distribution in the LPBF single-track scanning. They also compared their FE modelling result with an analytical model and found a more accurate melt pool simulation with their FE model. Zhidong et al. [87] proposed a comprehensive literature review of eight useful 3D heat source models and used them for melt pool geometry simulation. They compared the numerical results with experimental results and suggested a heat source including absorptivity function expression, as the best one for their work.

Shahabad et al. [23] implemented a heat transfer simulation with a 3D conical Gaussian heat source model and proposed two empirical equations based on the relationship between the key process parameters and the heat source model parameters. They predicted the melt pool geometry within a very low error range of 6–13%. This kind of reliable melt pool geometry prediction allows manufacturers to suppress defects by refining the LPBF process parameters before experimental trials. Mukherjee et al. [22] used a numerical simulation to investigate the potential improper fusion among tracks and layers during the LPBF process and predict the lack-of- fusion defect in the LPBF-made parts by simulated melt pool dimensions. In addition to the geometry, thermal variables of the melt pool can be extracted from the numerical modelling. Liu et al. [86] presented the temperature gradient, cooling rate, and solidification rate of the modelled melt pool area. By comparing the simulated thermal variables and the experimental grain morphology, they plotted the valuable Columnar to Equiaxed Transition (CET) criterion. Zhang et al. [90] and Promoppatum et al. [19] investigated the primary dendritic arm spacing (PDAS) as well as the grain morphology of the melt pool.

To simulate the laser interaction with metallic powders, the current study proposes a new hybrid heat source model for LPBF single-track scanning that includes three weighted conical Gaussian heat source models. Also, an absorptivity coefficient function, an absorptivity profile function, and an anisotropically enhanced thermal conductivity have been considered in this hybrid heat source. The model is developed to describe the thermal condition of molten metal during melting and solidification, for the process parameters which provide conduction melting mode. The original aspects of the developed model are as follows: 1) a triple-cone heat source profile is designed using physics-based observations to generate accurate melt pool geometry and temperature distribution; 2) the thermal variables such as G and R, are calculated for different locations and various time steps of melt pool solidification to predict many important aspects of the microstructure such as grain morphology, subgrain size, and grain growth direction.

5.2 Material and experiment

In this research, a numerical-experimental approach has been used to validate and calibrate the single-track scanning model with a new hybrid heat source model. To this end, several Ti-5553 single-tracks at different process parameter combinations (which lead to conduction melting mode)

were made and evaluated based on the existing literature and used to compare measured experimental and numerical melt pool dimensions [57]. For LPBF of Ti-5553, the laser power and scanning speed range used in this work were 125 - 225 W and 600 - 1600 mm/s, respectively.

5.2.1 Powder material

Samples were printed using Plasma Atomized Ti-5553 powder particles produced by AP&C. The microscopic observation (Fig. 5-1) shows that Ti-5553 powder particles are almost spherical in shape, with attached satellite particles.

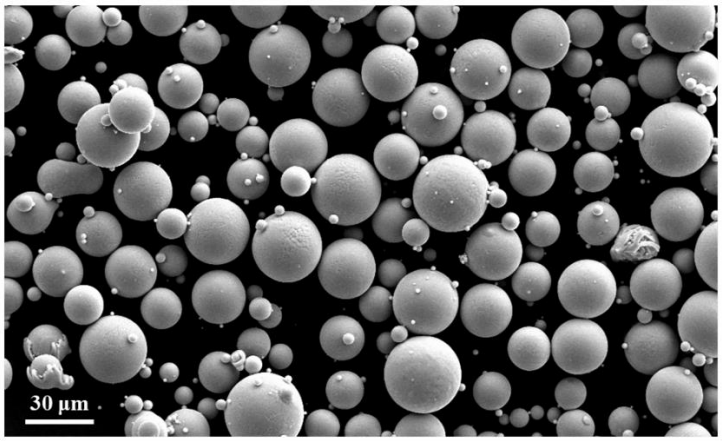

Figure 5-1: Microscopic image of the virgin Ti-5553 powder.

The summary of the image analysis from virgin powder is reported in Table 5-1. The analysis has been done by Bakhshivash et al. [146]. This Ti-alloy has martensite-suppressing elements such as V, Mo, Cr, and Fe, with chemical compositions (wt.%) reported in Table 5-2.

Table 5-1: The summary of the image analysis results [146]

	Count (#)	Minimum	Maximum	Average	Standard deviation
Size distribution	2237	0.48 µm	52.85 µm	12.36 µm	12.48 µm
Sphericity	2237	0.62	1.00	0.96	0.05

Due to the high strength and hardenability offered by beta metastable Ti-5553 alloy, it is currently used as the truck beam component material for the Boeing 7E7 and Airbus A-380 landing gear. It is recently employed in load-bearing fuselage components, high-lift devices in wide-body aircraft and even nacelles, wings, and landing gear [9,15,16,36,48].

Table 5-2: Chemical composition of the as-received Ti-5553 powder

Al	V	Mo	Cr	Fe	O	N	C	Ti
5.14	4.98	4.97	2.91	0.37	0.09	0.01	0.01	Balance

5.2.2 Processing and characterization

The EOS M290 machine equipped with a 400W Ytterbium continuous fibre laser with a wavelength of 1060 nm was employed to fabricate the single-track specimens. The laser spot diameter is 100 μm, and the process was carried out under a high-purity argon gas atmosphere.

To perform a detailed metallurgical study, a rectangular block with the same material (Ti-5553) was designed as a single-track substrate. The block substrates were fabricated with the same process parameters and dimensions of 25×18×5 mm. The process parameters are reported in Table 5-3.

Table 5-3: Process parameters of single tracks' substrate

Power (W)	Velocity (mm/s)	Hatch distance (μm)	Layer Thickness (μm)	Scan Strategy
225	1000	100	45	Stripes

Laser power and scanning speed of single tracks were varied as follows: laser power 125, 175, and 225 W and scanning speed 600, 800, 1000, 1200, 1400 and 1600 mm/s. The layer thickness of the single tracks is kept constant at 45 μm. It should be noted that a calibration step was performed after substrate printing and before the single-track scanning to eliminate the effect of powder packing (during substrate printing) and maintain a layer thickness of 45 um. Table 5-4 indicates the parameters used in single-track experiments. On top of each rectangular substrate, 2 different

parameters (1 fixed laser power and 2 varying scanning speed) with 3 replications were applied (2×3 single laser scan). The distance between each single-track was 2.5 mm.

To prepare the metallographic samples, the single-track specimens were cut and cross-sectioned using a Buehler ISOMET 1000 machine, at the one-third distance of the track line and perpendicular to the track scanning direction. The cut sections of samples were mounted, ground and polished according to standard procedures and etched by using Keller's reagent (95 ml distilled water, 2.5 ml HNO3, 1.5 ml HCl, 1 ml HF). For electron microscopy, an additional step was added to the preparation procedure, in which a non-crystallizing 0.02µm colloidal silica suspension (Buehler MasterMet2) was used to polish the specimen for about 5 hours with a Buehler VibroMet2 vibratory polisher.

Table 5-4: Process parameters of Single-track samples

Process parameter	Value
Power (W)	125 – 175 – 225
Scanning speed (mm/s)	600 – 800 – 1000 – 1200 – 1400 – 1600
Layer thickness (µm)	45

In order to measure the depth and width of the melt pools, a Keyence VHX-7000, high-resolution digital microscope was used at 6000X magnification. By using both the Full coaxial mode (Observation in the bright field) and Full ring mode (Observation in the dark field) of the microscope, melt pool boundaries could be resolved more readily. Scanning electron microscopy (SEM) and Electron backscatter diffraction (EBSD) analysis were performed by TESCAN VEGA3 SEM, equipped with a BRUKER e$^-$Flash^{FS} detector to investigate the melt pool microstructure of the fabricated single-track samples.

5.3 Numerical modelling of LPBF

5.3.1 Physical description

A three-dimensional model for LPBF single-track scanning was developed, and the commercial software COMSOL Multiphysics® was used to predict the melt pool geometry and temperature

distribution. For the geometry, a substrate domain of 1500×750×500 μm was considered the bulk part, and a top layer domain of 1500×750×45 μm as the powder part was modelled (Fig. 5-2). In the mentioned 3D model, the powder part was evenly covered on top of the bulk part, and the layer thickness was set to 45μm. Both solid and powder components were meshed using very fine cuboid (hexahedron) elements, resulting in a total of 105,000 elements. The single-track scanning required 57 minutes of computation on an Intel® Core i7-7700 CPU.

The developed model has also been studied with higher and lower element sizes. In comparison with the optimal state, when the number of elements was increased to 150000, the maximum melt pool temperature increased by 0.8%, the melt pool depth increased roughly by 1%, and the computation time extended by 3.6 times. Conversely, reducing the number of elements to approximately 65000 resulted in a 5.1% decrease in the maximum melt pool temperature, a reduction of about 9% in the melt pool depth, and a decrease in computation time to 0.8 times the optimal state. This comparison indicates that a higher number of elements, with a significant increase in computational time, provides similar results to the optimal case. On the other hand, reducing the number of elements not only does not significantly reduce the calculation time but also results in notable different outcomes from the optimal case.

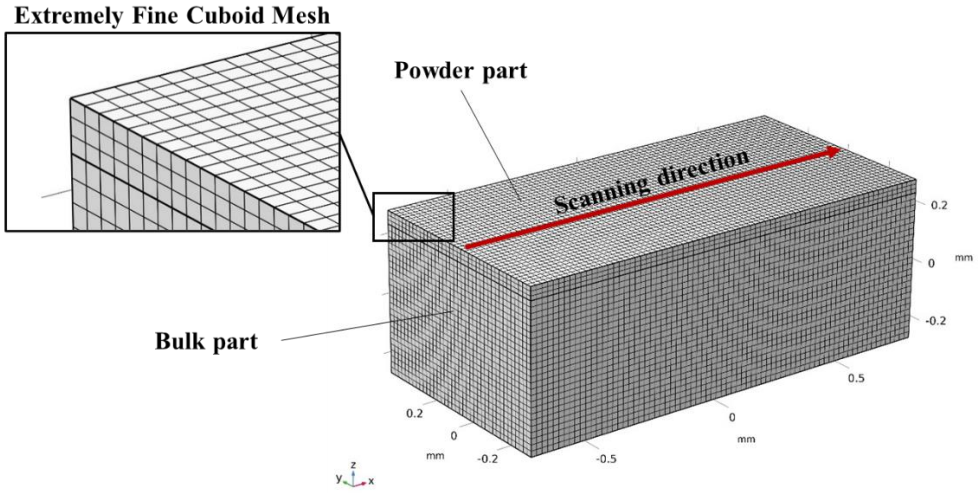

Figure 5-2: Designed single-track model geometry and mesh configuration for FE analysis.

5.3.2 Governing equation and boundary Conditions

Based on the first law of thermodynamics (i.e., conservation of energy), the governing equation for a three-dimensional heat transfer can be written in the following form (Eq. 5-1):

$$\rho C_p \frac{\partial T}{\partial t} - \left[\frac{\partial}{\partial x}\left(k_x \frac{\partial T}{\partial x}\right) + \frac{\partial}{\partial y}\left(k_y \frac{\partial T}{\partial y}\right) + \frac{\partial}{\partial z}\left(k_z \frac{\partial T}{\partial z}\right)\right] = Q(x, y, z, t) \quad (5\text{-}1)$$

where ρ is the density of material [kg/m^3], C_p is the specific heat [J/kg.K], T is the temperature [K], t is the time [s], k is the temperature-dependent thermal conductivity [W/m.K], and Q is the volumetric heat source [W/m^3].

Note that in Eq. 5-1, it has been assumed there is no mass transfer. Due to the preheating of the building plate, a constant 353K temperature was applied to the bottom surface of the 3D model, and the initial temperature of the entire model was set to 293K. It should be mentioned that the ambient temperature (T_{amb}) of the environment during the process was set to 293K. The convective and radiative heat losses were considered as other boundary conditions. The convective heat loss (q_c) was expressed based on Newton's law in Eq. 5-2 and applied to the top surface. The radiative heat loss (q_r) was applied on the top surface and accounted for by using the Stefan-Boltzmann law (Eq. 5-3). Since the thermal conductivity of the powder is very low, the isolation boundary condition was assumed in the other boundary surfaces.

$$q_c = h_c\,(T_{amb} - T) \quad (5\text{-}2)$$

$$q_r = \varepsilon \sigma_{sb}\,(T_{amb}^4 - T^4) \quad (5\text{-}3)$$

where h_c is the convective heat transfer coefficient [W/(m^{2}K)], ε is the melt pool and surrounding zone emissivity, and σ is the Stefan–Boltzmann constant [W/(m^{2}K^4)].

5.3.3 Material properties

In this simulation, two different material properties of Ti-5553 were assigned to the model for two forms of bulk and powder. Due to the similarity between the physical properties of Ti-5553 and Ti-64, for unknown properties of Ti-5553 powder, some interpolations have been used based on published Ti-64 powder properties. The effective thermal conductivity of Ti-64 powder is typically from 0.22 to 0.53 W/m.K below 664 K ($0.4T_m$) and about 6.9 W/m.K at melting temperature. On the other hand, the bulk thermal conductivity of Ti-64 at room temperature and melting point is

from 6.7 to 7.5 W/m.K and about 33.4 W/m.K, respectively [74,78,147–149]. Based on the existing bulk thermal conductivity of Ti-5553 and corresponding values of Ti-64 alloy, the thermal conductivity of the Ti-5553 powder was estimated and reported in Table 5-5 [150]. In Table 5-5, the density, and the specific heat of solid and powder Ti-5553 have been mentioned as well. The density of the powder Ti-5553 (effective density) was calculated based on bulk density (Eq. 5-4) and defined as:

$$\rho_{Powder} = (1 - \varphi)\rho_{Solid} \tag{5-4}$$

where ρ_{Powder} is the density of powder, ρ_{Solid} is the density of the solid and φ is powder porosity. The powder porosity has an initial value (assumed 0.45 in this work) under melting temperature (1933 K) which decreases to zero when the powder is fully melted [148,151].

As in prior literature, the powder part heat capacity was assumed to be the same as that of the solid [23,152]. Note that, to compensate for the latent heat of fusion, the specific heat increased between solidus and liquidus and assumed the latent heat of fusion is equal to extra absorbed heat in this range [23]. The amount of this modification in the mentioned temperature area can be derived from Eq. 5-5 [20]:

$$C_P = \begin{cases} C_{P,\text{Sensible}} & for \quad T < T_s \\ C_{P,Modified} = C_P + \frac{L}{\Delta T_m} & for \quad T_s < T < T_l \\ C_{P,\text{Sensible}} & for \quad T > T_l \end{cases} \tag{5-5}$$

where T_s, T_l, and L are solidus temperature, liquidus temperature, and the latent heat of fusion, respectively. As the melting point of Ti-5553 (liquidus) is about 1933 K and the melting temperature range is assumed 50 K, the solidus temperature will be approximately 1883 K.

Table 5-5: Thermophysical properties at specific temperatures for bulk and powder Ti-5553

	Thermal conductivity (W/m.K)	**Density (g/cm^3)**	**Specific heat (J/g.K)**
Bulk Ti-5553	5 (298) – 34.4 (1933)	4.3 (298) – 3.9 (1933)	0.53 (298) – 0.83 (1933)
Powder Ti-5553	0.26 (298) – 8.62 (1933)	2.1 (298) – 1.6 (1933)	0.53 (298) – 0.83 (1933)

For thermal conductivity and density of molten titanium, a 40% and 10% reduction have been considered, respectively, based on solid-to-liquid phase transformation. In this study, to improve the accuracy of the simulated melt pool dimensions, the anisotropically enhanced thermal conductivity method was employed [24,86,87,153]. It can be expressed as (Eq. 5-6):

$$k_x = \lambda_x k, \quad k_y = \lambda_y k, \quad k_z = \lambda_z k \tag{5-6}$$

where λ_x, λ_y, and λ_z are the thermal conductivity (k) enhancement factors. As mentioned in the literature, the thermal conductivity of an LPBF-made solid part along the build direction (z) is much higher than along the horizontal (x,y) directions. This anisotropic behaviour is related to the grain shapes and orientations (columnar grain along with build direction), which affect the electron and phonon transport from grain boundaries [30]. Therefore, the enhancement factor in the depth direction (λ_z) should be greater than in the other directions. Based on a published study by Zhou et al. [30], the enhancement factors of λ_x=1, λ_y=1, and λ_z=3 were defined for the bulk part (LPBF-made substrate) of the model. Also, fluid dynamics have not been considered in the modelling to reduce the complexity of the simulation and the computational time. The anisotropically enhanced thermal conductivity method is commonly used by researchers [86,87,154,155] to compensate for the effect of the heat convection of the fluid. Therefore, the same enhancement factors were defined for the powder part of the model.

Finally, it is worth mentioning that, at first, the thermophysical properties of Ti-5553 powder were assigned to the powder part, but after the solidification of a molten element of the powder part, all thermophysical properties of the solid will be assigned to that element. Also, to improve the computational efficiency, the material absorption coefficient did not vary with phase changes in this simulation.

5.3.4 Hybrid heat source model

The three-dimensional conical Gaussian heat source model is a well-known volumetric heat source implemented in the simulation of metallic PBF and welding processes. In this 3D heat source model, a Gaussian heat intensity distribution is applied in a conical profile. Since it has a semi-cylindrical geometry perpendicular to the component thickness and choosing a proper height for the cone can effectively compensate for the absence of convection heat transfer, it is suitable for the simulation of deep penetration laser welding and manufacturing [23,84,156,157]. In the current

research, a new hybrid conical heat source model with the Gaussian distribution has been developed and used for simulation. As mentioned in the introduction, in this kind of FE modelling, conduction is the dominant heat transfer mechanism. Hence, when the laser irradiates on the top surface powder particles, the laser intensity will be absorbed by those particles, and then the absorbed heat will penetrate through the build piece based on the heat source model shape and intensity distribution function.

In reality, the top surface powders can not absorb laser radiation completely, and a portion of the laser beam may penetrate through the gaps between powder particles directly or via reflection and heat the lower sublayer powders. Indeed, as reported in a previous study by Boley et al., laser energy absorption of the powder layer in additive manufacturing is the sum of each sublayer's absorbed energy [158–161]. Based on this fact, using multiple heat source profiles (for powder sublayers) in the LPBF process is needed. It should be noted all the above-mentioned facts are related to the conduction melting mode, where the powder condition is more stable, and the following model should not be used for the process parameters which cause an unstable keyhole melting mode. It should be noted that there is no laser beam transmission in titanium powders.

The proposed hybrid model in the current research addresses this physics. Fig. 5-3 shows the percentage of laser energy absorption by the first powder layer directly and the percentage of the laser energy that may penetrate into the next sublayer. This portion can be calculated by a simple area ratio measurement.

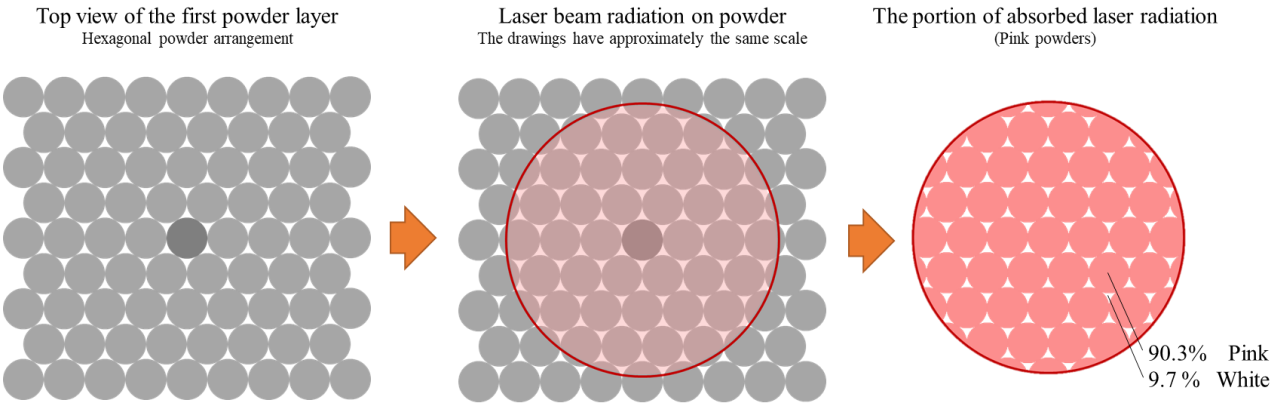

Figure 5-3: The percentage of absorbed laser radiation in the first layer of powder. About 90% of laser radiation is absorbed and the remaining 10% penetrates to the next powder sublayer.

Since the nominal diameter of the laser beam is 100 μm and the powder size (diameter) is assumed 15 μm (based on the average size of Ti-5553 powder from Table 5-2), the first powder sublayer may absorb about 90% of laser radiation, and about 10% may penetrate to the next sublayer. The calculated percentage agrees with similar investigations in the literature [161].

As layer thickness is 45 μm, it can be assumed that there are 3 sublayers and for each sublayer, a specific 3D conical Gaussian heat source should be applied. This hybrid heat source is called the triple-cone heat source model.

Based on a 3D conical Gaussian heat source model, laser beam heat input at any plane (x,y) perpendicular to the z-axis at time *t* can be expressed as (Eq. 5-7):

$$Q_v\,(x,y,z,t) = \frac{6\alpha P}{\pi H(r_0^2 + r_0 r_1 + r_1^2)} \exp\left[-2\,\frac{(x-x_c)^2 + (y-y_c)^2}{r^2}\right]$$

$$r(z) = r_0 + \frac{z}{H}(r_0 - r_1) \tag{5-7}$$

where α, P, x_c, and y_c are the material absorptivity, laser power, and the positions of the beam center in *x* and *y* directions, respectively. As shown in Fig. 5-4a, *H* is the height, *r* is the radius at different z, r_0 is the radius of the laser spot on top (50 um) and r_1 (30 um) is the radius on the bottom of the conical Gaussian heat source. The values for parameters *H* and α will be explained in section 5.4.1.

For the triple-cone heat source model, since the portion of laser effectiveness in the first sublayer is 90% and penetration to the next sublayer is 10%, a factor of 90%, 9%, and 1% should be considered for the heat source model of the top sublayer, middle sublayer, and bottom sublayer, respectively (Fig. 5-4b).

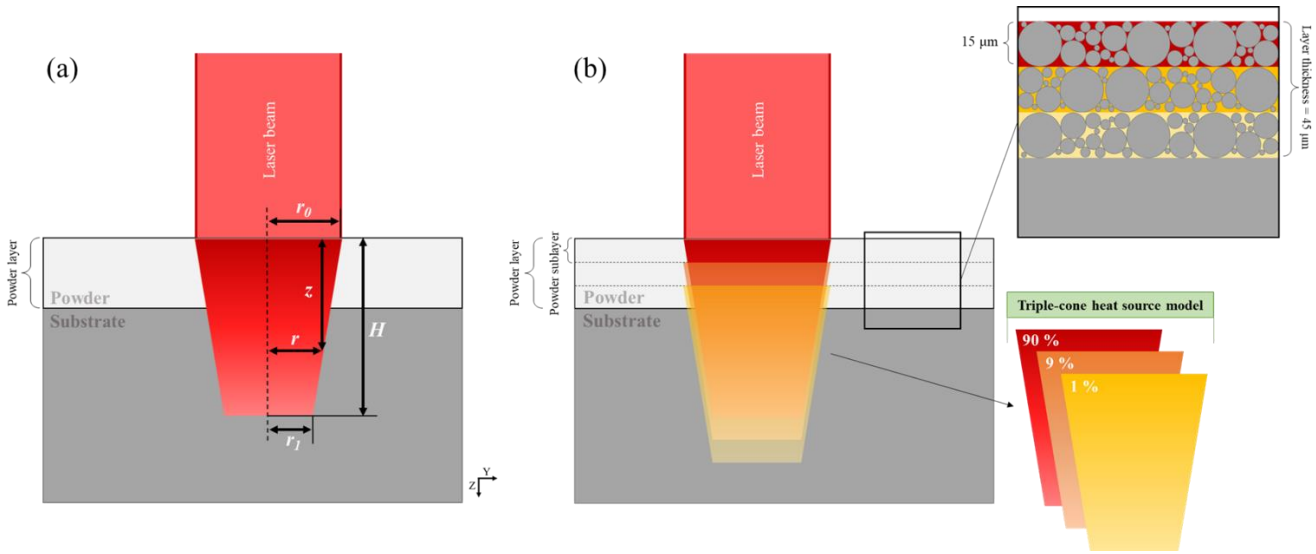

Figure 5-4: Schematic diagram of the volumetric heat source models: (a) Conical Gaussian heat source model and (b) the hybrid triple-cone Gaussian heat source model.

One of the main advantages of this triple-cone heat source in comparison with a regular (single-cone) conical heat source, at the same conditions, is that the temperature in the simulated melt pool with a triple-cone heat source is more distributed through the layers. In the simulated melt pool with a regular conical Gaussian heat source, the temperature of the hottest region is extremely high (higher than the material boiling point), even in the conduction melting mode. To address this issue, the temperatures above the boiling temperature (T_b) should be capped at T_b. Therefore, the temperature distribution in the considerable area of the melt pool will be affected by this assumption. On the other hand, the triple-cone Gaussian heat source can lead the heat through the model domains and provide an acceptable temperature distribution (under boiling point) for the simulated melt pool. Hence, the hybrid triple-cone Gaussian heat source model is more reliable for the investigation of solidification and microstructure formation, compared to the regular cone Gaussian heat source model.

5.4 Result and discussion

5.4.1 Experimental measurement and validation

As mentioned in Table 5-4, LPBF single-tracks with a laser power range from 125 to 225W, scanning velocities from 600 to 1600 mm/s, and a layer thickness of 45 μm were printed on LPBF-made Ti-5553 substrate. The melt pool width and depth were measured through the microscopic images of the single-track cross-sections. To validate and calibrate the developed model, the measured melt pool dimensions were used to make a comparison between the experimental and numerical results [23,85,87].

Suzuki et al. [162] found that the melt pool depth and melt width have linear relationships with $P/\sqrt{v}$ based on the equation of deposited energy density, E_D [J], as follow:

$$E_D = \frac{AP}{\sqrt{\pi D v \sigma^3}} \tag{5-8}$$

where A and P are the laser absorptivity and the laser power [W], respectively, $D\tau$ is the thermal diffusivity [$m^2.s^{-1}$], v is the laser scanning speed [m/s] and σ [m] is the laser spot size (Fig. 5-5b). Shahabad et al. [23] reported that as the melt pool size is proportional to heat source profile height (H) and laser absorptivity (α) of the conical Gaussian heat source model, these two factors have also direct relationships to $P/\sqrt{v}$, which this ratio can be used for model calibration. When the deposited energy density increases, the melt pool depth becomes larger due to higher heat penetration, and the material tends to absorb more energy. The flowchart in Fig. 5-5a shows how the height of the heat source profile and absorption coefficient were used in the calibration procedure [23]. In this figure, D_{Sim}, W_{Sim}, D_{Exp}, and W_{Exp} are simulated melt pool depth, simulated melt pool width, experimental melt pool depth, and experimental melt pool width, respectively, and ε is the maximum acceptable error of model prediction (10%).

As shown in Fig. 5-5c and Fig. 5-5d, the behaviour of the achieved H and α due to energy density changes are linear. Therefore, the empirical equations for H and α could be described in Eq. 5-9 and Eq. 5-10:

$$H = a_1 \frac{P}{\sqrt{v}} + b_1 \tag{5-9}$$

$$\alpha = a_2 \frac{P}{\sqrt{v}} + b_2 \quad (5\text{-}10)$$

where H [μm], α, P [W], and v [mm/s] are the height of the conical Gaussian heat source, laser absorptivity, laser power and scanning speed, respectively. The coefficients in the H and α empirical equations are as follows: a_1=26.704, b_1=50.534, a_2=0.0578, and b_2=0.2006.

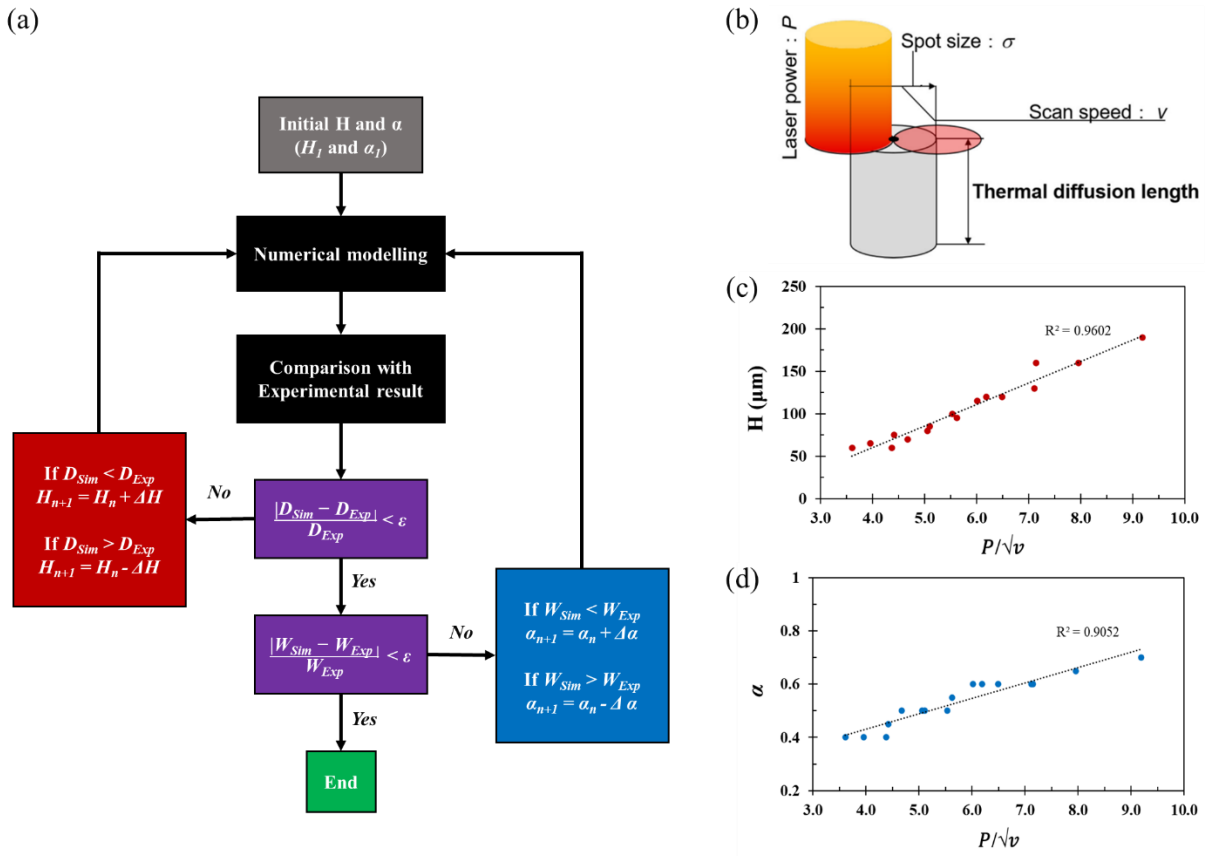

Figure 5-5: (a) Flowchart of the heat source calibration procedure [23]. (b) Schematic illustrations deposited energy density [162], (c) liner behaviour of height of the conical Gaussian heat source H, and (d) absorption coefficient α due to the deposited energy density changes.

After calibration, the numerical results revealed a good agreement with the experimental results. Their average difference percentage for the melt pool depth was 8.8% and for the melt pool width was 4.5%.

Fig. 5-6 shows the comparisons of experimental and simulated melt pool dimensions at 225W, 175W, and 125W. In this figure, melt pool size measurements (16 single tracks with 3 replications) are plotted as a function of laser power and scanning speed. As shown in Fig. 5-6, for all powers, the melt pool depth and width were reduced by increasing the scanning speed. Therefore, the deepest and widest melt pool belonged to the largest power and the smallest scanning speed (225W, 600 mm/s), and the smallest melt pool depth and width belonged to the smallest power and the largest scanning speed (125W, 1200 mm/s). Since the single tracks with a power of 125 W and scanning speeds of 1400 and 1600 mm/s were not stable enough, their melt pool dimensions were not measurable.

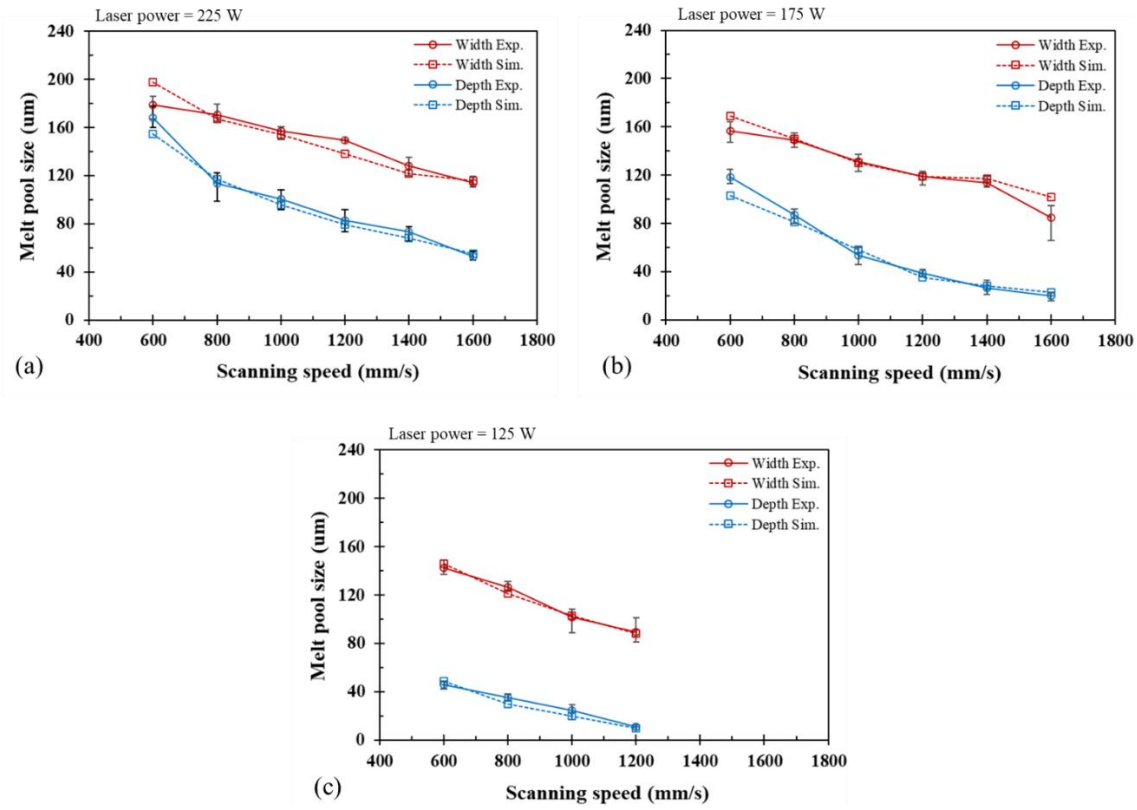

Figure 5-6: Comparisons of experimental and simulated melt pool dimensions at different laser powers of (a) 225, (b) 175, and (c) 125 W. The average percentage difference between numerical and experimental results for the melt pool depth was 8.8% and for the melt pool width was 4.5%.

Fig. 5-7 shows the experimental and numerical melt pool shape and dimensions at two different process parameters. It should be noted that in the measurement of the simulated melt pool depth,

the powder layer has not been considered. The experimental results are clearly in good agreement with the numerical results. This predicted melt pool dimension can be used for finding the melting mode thresholds, possible defects, and process optimization. For instance, low input energy (low laser power and high scanning speed) may cause a shallow and small melt pool and the lack-of-fusion defects [9]. In fact, when the melt pool width is small and two adjacent melt pools can not cover the gap between themselves, a lack-of- fusion is expected [1,22]. On the other hand, at high input energy (high laser power and low scanning speed), a deep melt pool with a spherical defect at the bottom of that is expected. This defect is typical of the laser beginning to operate in keyhole mode [1,79]. These two facts should be taken into consideration for hash distance and layer thickness choice.

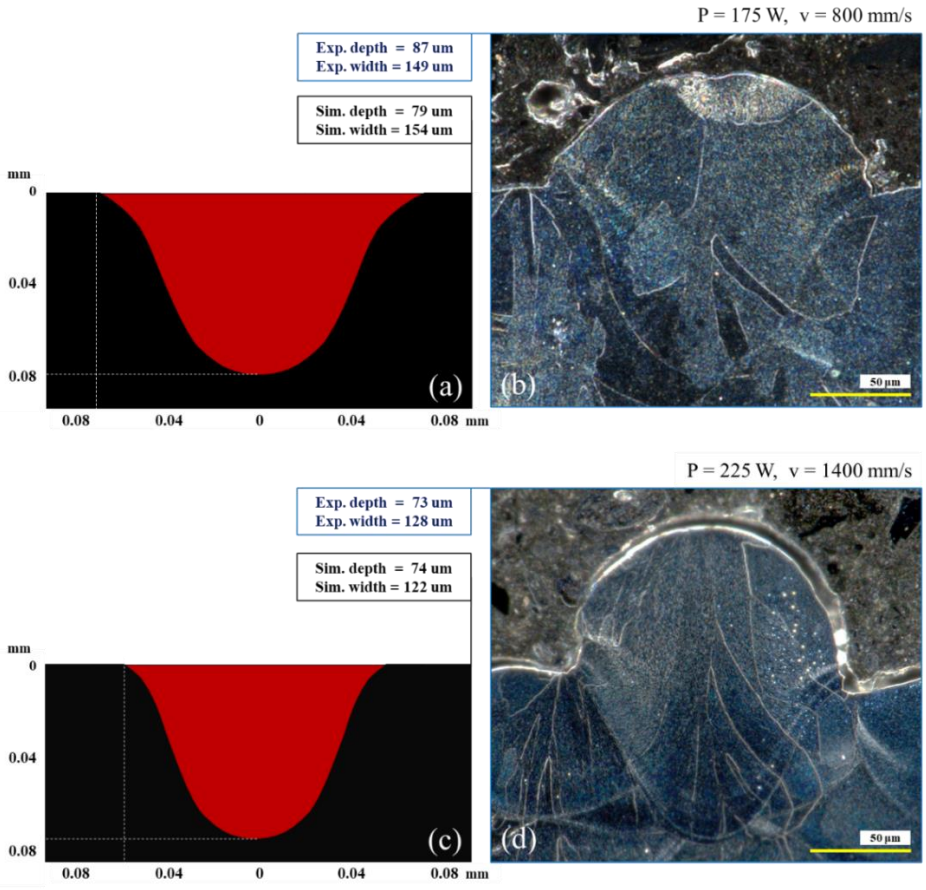

Figure 5-7: Numerically and experimentally measured melt pool dimensions, at (a)(b) P = 175 W, v = 800 mm/s and (c)(d) P = 225 W, v = 1400 mm/s.

5.4.2 Temperature distribution

The temperature distribution in the melt pool and its effect on microstructure can be discussed by the extracted results from the developed model. Fig. 5-8 illustrates the temperature history of a melt pool with process parameters of P = 175 W and v = 600 mm/s, at 5 different points. These 5 points (probes) have been shown in the simulated melt pool, in the top right-hand corner of the figure. They were set in the z-direction (in the direction of melt pool depth) from the depth of 50 µm towards the bottom of the melt pool, at 10 µm intervals. The melt pool figure has been captured at t = 8.8 $\times 10^{-4}$ s when all the points have their highest temperature. As expected, at this time, the temperature peak decreases from the center to the bottom of the melt pool. Based on this fact and the temperature contours in the simulated melt pool, the hottest region is in the centre of the melt pool. This region, because of its highest temperature, will be the last point of solidification. This matter is reported experimentally in the literature [13].

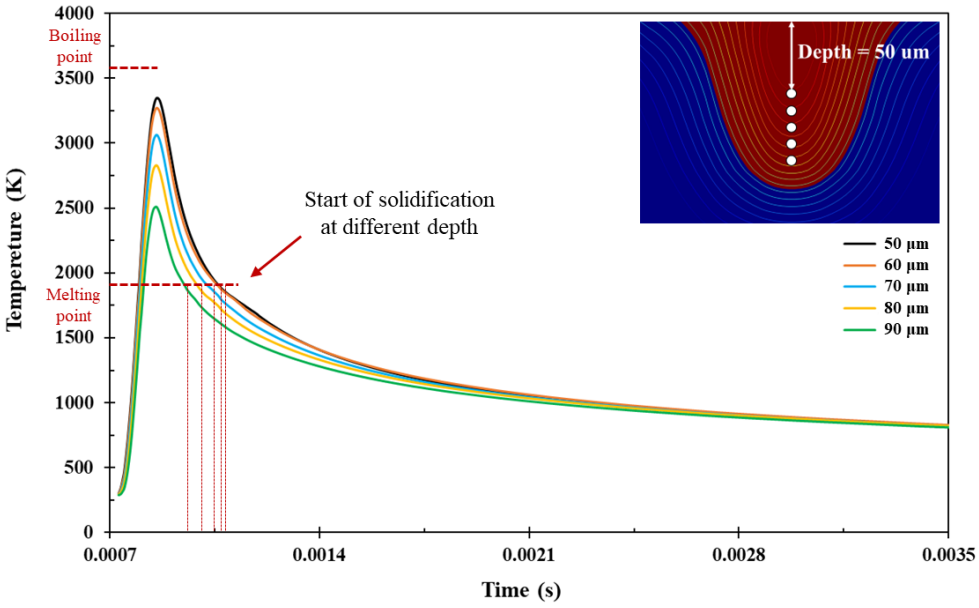

Figure 5-8: Temperature history at 5 different locations (depth) of the melt pool region. During the cooling period, the melting point is the start of solidification at different depths. The process parameter is P = 175 W and v = 600 mm/s.

In Fig. 5-8, the boiling temperature line shows that the maximum temperature of the melt pool is lower than the boiling point. So, for this process parameter (175 W, 600 mm/s), notable metal evaporation and keyhole defect formation are not expected.

By comparing the temperature history diagram and CCT diagram of an alloy, the solid-state phase transformations can be inferred. The modelling of the LPBF process for Ti-5553 alloy shows the temperature of the hottest point of the melt pool decreased from melting point to room temperature in less than 1 second. Since the solid-state phase transformation of β to β + α during a continuous cooling from the melting point needs at least about 10 seconds, the solidified melt pool of LPBF-made Ti-5553 has just a β phase. The experimental EBSD phase detection and literature XRD confirm that the β phase is the dominant phase of the as-printed Ti-5553 [4,55].

To investigate the solidification process of a melt pool, the extraction of thermal variables such as temperature gradient, cooling rate, and solidification rate is essential. As shown in Fig. 5-8, the temperature decreases after its peak. So, this point can be stated as the cooling start. To have a more reliable solidification study, the thermal diagrams should be extracted from the starting point of the solidification. As mentioned in section 5.3.3, the liquidus-solidus rage of this alloy is as low as 50 K. Hence, instead of liquidus-solidus rage, a specific temperature (melting point) was considered for the starting point of the solidification. In Fig. 5-8, it can be seen at the melting point, the solidification in the bottom of the melt pool (Green line) begins sooner than the centre of that (Black line). In this work, since the thermal variables of the melt pool have been extracted from the moving solidification front (solid-liquid interface), these variables will be presented in the form of some consecutive steps, from the beginning of solidification to the end (Fig. 5-8).

5.4.3 Temperature gradient (G) and solidification rate (R)

During solidification, the formed microstructure is governed by thermal variables including temperature gradient G and solidification rate R. For instance, G/R determines the morphology of the solidification structure and G.R (cooling rate or $\dot{T}$) determines the size of the solidification structure [19,20]. Therefore, the estimation and prediction of these critical variables are vital to investigate the correlation between LPBF process parameters and formed microstructure.

In Fig. 5-9, the solidification process of a melt pool (175 W, 600 mm/s) is shown in four consecutive steps in which the melt pool geometry and thermal variables are demonstrated at each

time step. The temperature gradient in the melt pool region is illustrated by the rainbow colour map. In general, in high-temperature zones, the temperature gradient is lower than that in the other zones. In addition, the average melt pool temperature gradient follows a decade trend during the solidification.

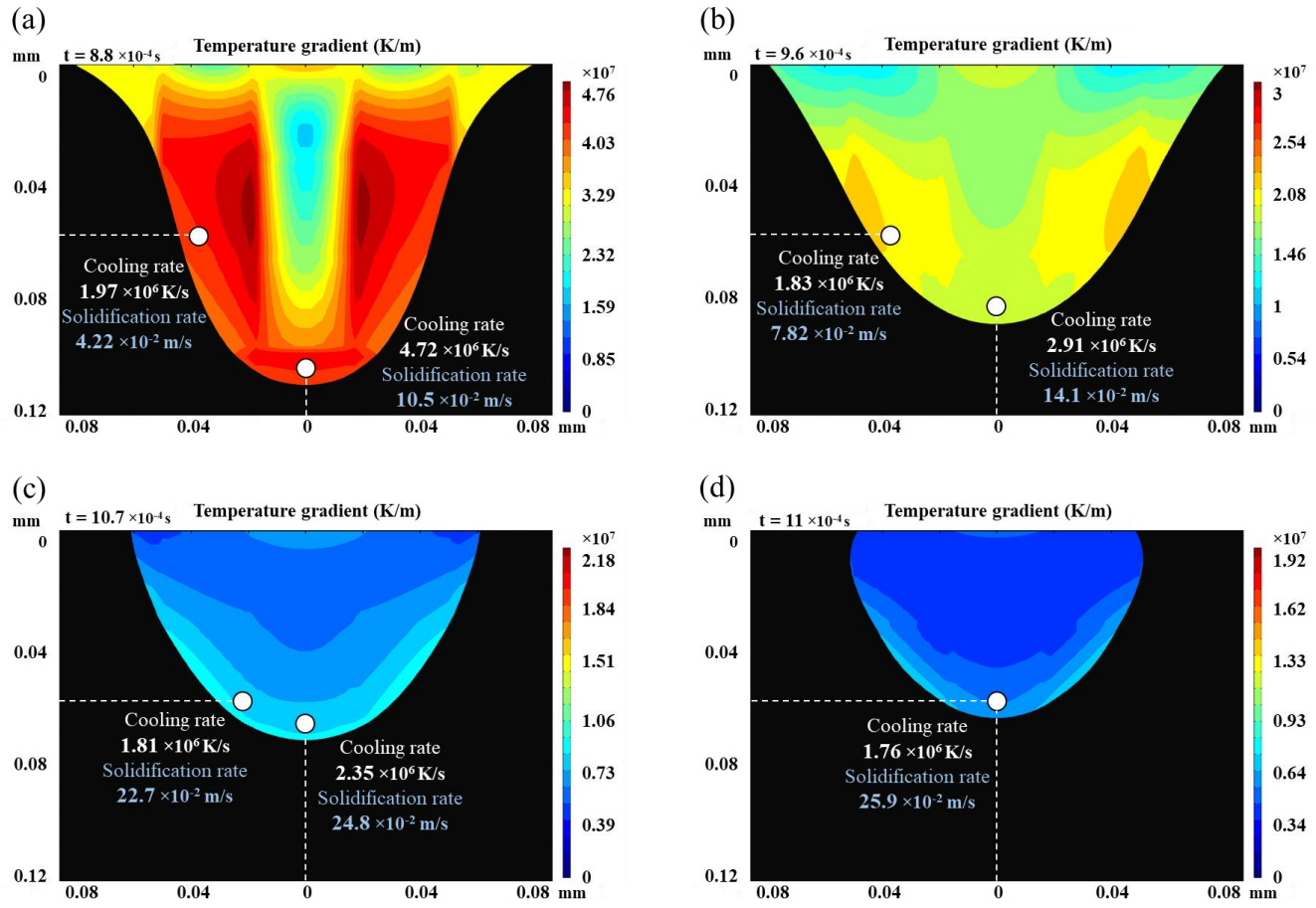

Figure 5-9: Temperature gradient, cooling rate, and solidification rate at the solidification front, during the solidification of a melt pool (P = 175 W, v = 600 mm/s). They are plotted in 4 consecutive steps, from the beginning (a) to the almost end (d).

The front side of the crystallization area shifts towards the center of the melt pool. The temperature histories of several probes, in both *z* and *y*-direction, were used to find the cooling rate and solidification rate of the solidification front. Therefore, probes are designed to keep track of the melt pool variables (such as the cooling rate and solidification rate) along with *y* and *z* directions.

z-direction probes are located in the middle of the melt pool width (where $y = 0$ um), while *y*-direction probes are located in the middle of the melt pool depth ($z = 50$ um). To calculate cooling rates, the first derivative of temperature histories can be used at the solidification starts (Fig. 5-8). Furthermore, the solidification rate can be determined from the temperature gradient and calculated cooling rate.

During the melt pool solidification, the cooling rate, and the solidification rate along with *z*-direction (from the bottom to the center of the melt pool) decreased from 4.72×10^6 K/s to 1.76×10^6 K/s and increased from 10.5×10^{-2} m/s to 25.9×10^{-2} m/s, respectively. Therefore, the solidified microstructure of the bottom of the melt pool experienced a higher cooling rate and a lower solidification rate in comparison with the formed microstructure of the center.

Compared to *z*-direction solidification data, Fig. 5-9 also reveals the same solidification trends along with *y*-direction (from sides to the center of the melt pool). From the start of solidification to the (almost) finish, the cooling rate and the solidification rate decreased from 1.97×10^6 K/s to 1.76×10^6 K/s and increased from 4.22×10^{-2} m/s to 25.9×10^{-2} m/s, respectively. It should be noted that the estimated G and R can help the interpretation of grain morphology and subgrain structure formation.

5.4.4 Grain morphology prediction

To investigate the effect of key thermal variables on grain morphology, combined parameters such as G/R and G.R are selected to predict the solidification mode and subgrain feature size. Solidification parameters (G, R, G.R, and G/R) at the solid/liquid moving boundary of the melt pool (175 W, 600 mm/s) are plotted in Fig. 5-10a and Fig. 5-10b, as a function of time. Fig. 5-10c shows the solidification map for a comparable Ti alloy (Ti-64), which is the closest available solidification map for Ti-5553 [152]. This map can be utilized to illustrate the grain morphology of the solidified melt pool. Depending on the melt pool thermal condition, the growth mechanism can be limited to epitaxial growth or extended to some level of equiaxed grain growth. A higher level of homogeneous/heterogeneous nucleation leads to a higher number of solidified crystals and results in a fully/partially equiaxed structure. In this regard, the grain morphology can be predicted well based on the solidification rate and temperature gradient [152,163].

In Fig. 5-10c, the simulated G and R of each step were employed to predict the grain morphology of a selected single-track. It shows among three possible solidification morphologies (columnar, equiaxed, and mixed columnar/equiaxed structures), the grain morphology at all four melt pool locations would be fully columnar. In the same processing condition, the actual grain structure of the corresponding melt pool shows a fully columnar morphology too (Fig. 5-11a).

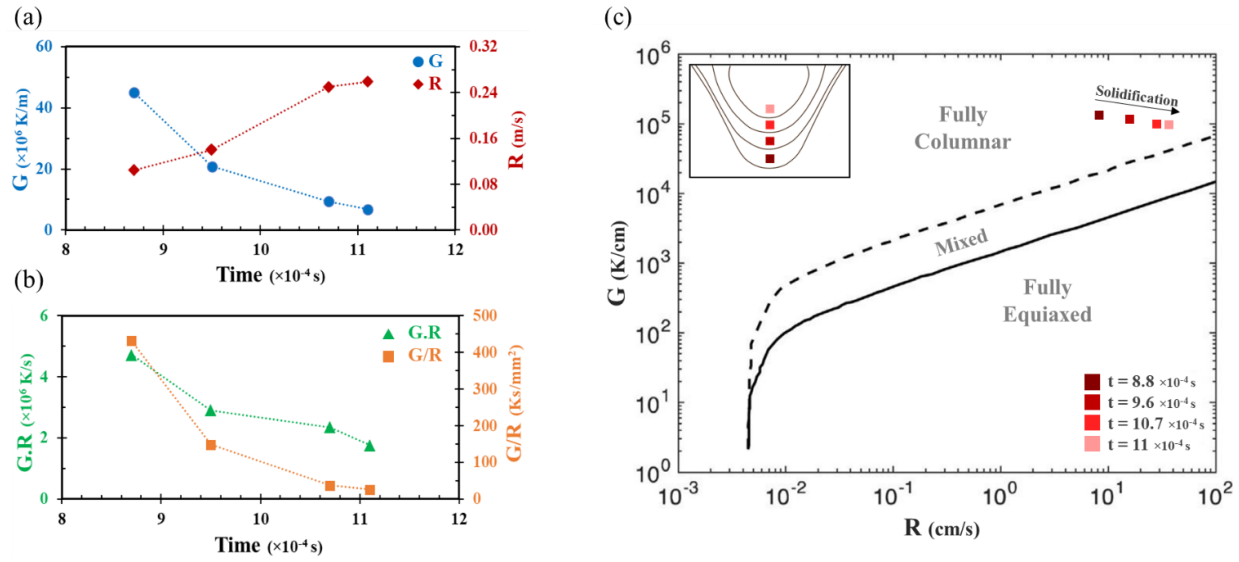

Figure 5-10: (a) Predicted temperature gradient G and solidification rate R, and (b) G.R and G/R values, during the solidification of a melt pool (P = 175 W - v = 600 mm/s). (c) Prediction of grain morphology, based on simulated thermal variables and solidification map [152,163].

As shown in Fig. 5-10c, in the solidification map, since the early-stage solidification condition is far away from the mixed region (at $t = 8.8 \times 10^{-4}$ s), the grain structure of the outer melt pool region is expected to be strongly columnar. However, during solidification, moving toward the center of the melt pool experiences a condition closer to a columnar/equiaxed mixed behaviour (at $t = 11 \times 10^{-2}$ s), which implies having a higher nucleation rate compared to the outer regions. In other words, for a melt pool that has a mixed columnar/equiaxed structure, the probability of equiaxed grain formation in the center of the melt pool is higher than in the other regions of the melt pool. This fact has been reported in the experimental result of a previous study by Liu et al. [86]. In addition, Fig. 5-10b shows the G/R trend is decreasing and the value of the last point is lower than

the others while the formation of an equiaxed grain morphology is expected in locations with lower G/R values [131,164].

It is important to investigate the heat flow of the melt pool, as epitaxial grains grow along with the heat flow direction. In this regard, the heat flow directions of the liquid metal are shown in Fig. 5-11b with red-coloured arrows, and the grain morphology of the melt pool is depicted in Fig. 5-11a. Comparing the depth to the side of the melt pool a gradual transition in heat flow direction is simulated when vertical heat flows (at the bottom of the melt pool) are tilting toward the center of the melt pool (at the sides of the melt pool), Fig. 5-11b. The simulated heat flow results fall in good agreement with the actual solidification direction.

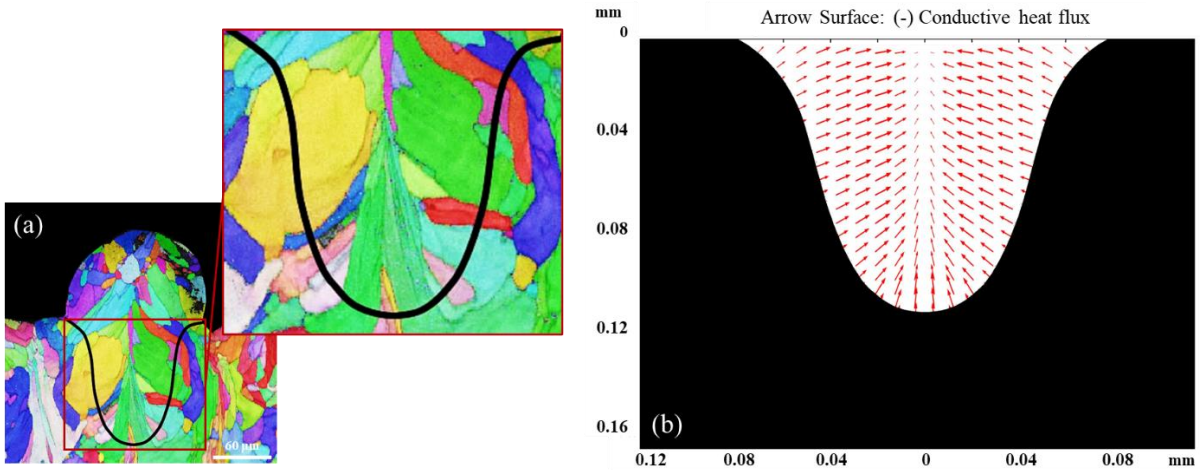

Figure 5-11: (a) EBSD image shows columnar grains and their growth direction in the melt pool. (b) Simulated heat (loss) flow directions in red-coloured arrows. The process parameter is P = 175 W and v = 600 mm/s.

In addition to the grain morphology, the other microstructure features such as primary dendrite arm spacing (PDAS) affect the mechanical behaviour of materials. PDAS is the distance between two neighbouring dendrite centers [145]. In recent years, several research studies have been done on the connection between the solidification behaviour in metal AM and the PDAS. One of the common topics in this area is finding the relationship between PDAS and cooling rate, qualitative or quantitative by using the developed equations for the casting solidification of different materials [165–167].

Fig. 5-12b and Fig. 5-12c compare the experimental and numerical results of subgrain size measurement. Based on the schematic solidification map (Fig. 5-12a), in the columnar dendritic region, higher cooling rates in the solidification front cause a smaller feature size or lower PDAS. Fig. 5-12b shows the extracted cooling rate in the solidification front of a simulated melt pool. It demonstrates the cooling rates varied. From the bottom to the top of the melt pool, at first, the cooling rate decreased, then increased. The lowest cooling rate has been signed by a yellow rectangular in Fig. 5-12b. On the other hand, Fig. 5-12c shows an experimental microscopic image of the same melt pool. It is observed that the dendrite size of the region which has a lower cooling rate is larger than the regions above or below this location. This also indicates an agreement between the model and the experimental result.

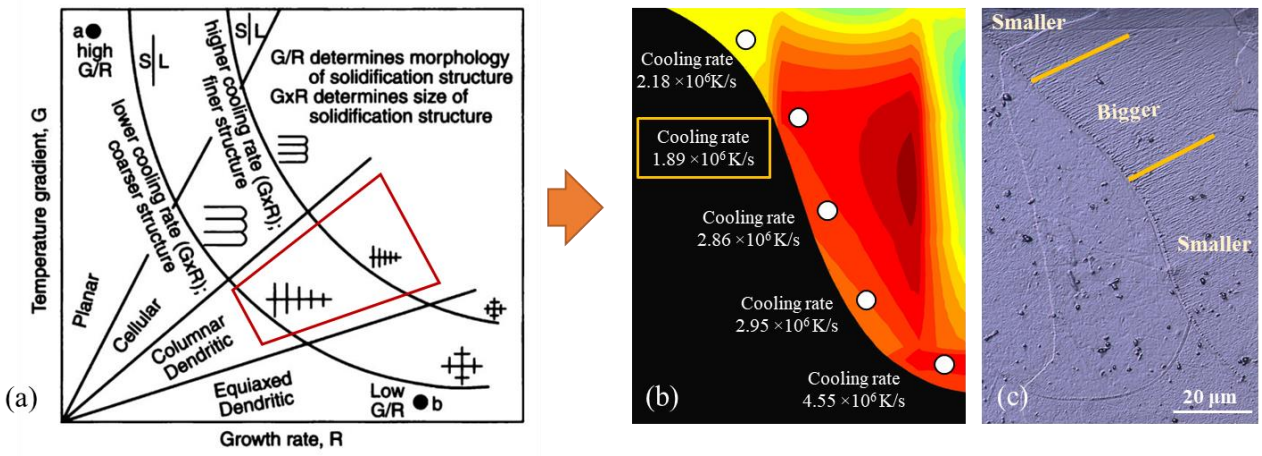

Figure 5-12: (a) The schematic solidification map [131]. (b) Modelled cooling rate and (c) microscopic image of dendrites in the solidification front of a melt pool (P = 175 W - v = 600 mm/s). As expected, the dendrite size in the region with a lower cooling rate is bigger.

As the earlier paragraph compared the results (cooling rates and PDAS) qualitatively, here, the comparison is done more in a quantitative method. The empirical equations in the literature demonstrate the relation between PDAS and cooling rate. The general form of these equations is shown in Eq. 5-11:

$$\lambda_1 = A\dot{T}^{-n} \tag{5-11}$$

where λ_1 is primary dendrite arm spacing, $\dot{T}$ is the cooling rate, and A and n are constant values while constants are estimated to be $A = 49.038$ and $n = 0.324$ for the Ti-alloys [165].

To assess the quality of the developed model, another melt pool condition (with laser power of 225 W and scanning speed of 600 mm/s) was selected to compare the estimated cooling rate (obtained from the empirical Eq. 5-11) to the simulated cooling rate. The simulated thermal variables and measured PDAS are shown in Fig. 5-13a and Fig. 5-13b, respectively. Since thermal variables vary along with the melt pool boundary, the same location (in both simulated and actual melt pools) is selected to compare the cooling rate from numerical and experimental measurements. With the average measured PDAS of 0.51 μm (Fig. 5-13b), the cooling rate was calculated ~1.32×10^6 K/s (Eq. 5-11). On the other hand, a close cooling rate value (~1.48×10^6 K/s) is obtained from the simulation result.

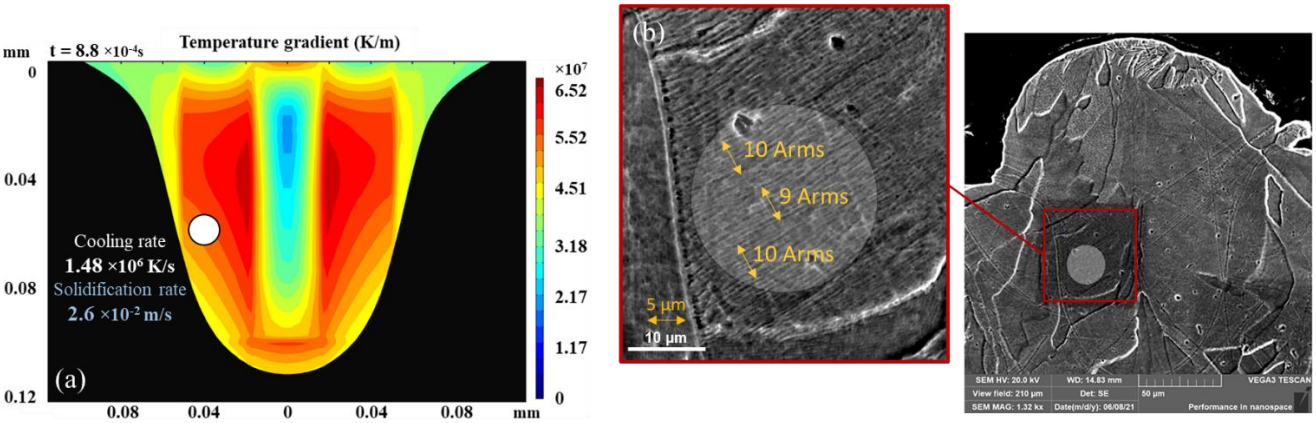

Figure 5-13: (a) Simulated thermal variables and (b) experimentally measured primary dendrite arm spacing in a melt pool with the same process parameters (P = 225 W, v = 600 mm/s).

5.4.5 Effect of process parameters on thermal variables

It is shown that the current model can be quite useful in terms of predicting thermal variables, grain growth or heat flow direction, grain morphology, and subgrain feature size. Changing key process parameters in the simulation (laser power and scanning speed) and calculating thermal variables can help to tune the process condition through a simulation process without any tedious

experimental measurement. In this matter, the developed model is employed to have an in-depth understanding of the effect of process parameters on the heat distribution.

The thermal analysis was done for melt pools with different scanning speeds changing from 800 mm/s to 1200 mm/s (fixed laser power of 225 W) and for melt pools with different laser powers changing from 125 W to 225 W (fixed scanning speed of 800 mm/s). Simulated G, R, G.R, and G/R were extracted from the mentioned melt pools and reported in Fig. 5-14. These thermal variables were measured at the beginning of solidification where the probes were located at the bottom of the melt pools.

At a fixed laser scanning speed (800 mm/s), both G and R values show a downward trend when laser power increases from 125 W to 225 W (Fig. 5-14a). On the other hand, with a fixed laser power (225 W), G and R values show an upward trend when the scanning speed increases from 800 mm/s to 1200 mm/s (Fig. 5-14b). In general, it is observed that a higher energy input reduces G and R values when either laser power or scanning speed is set to be a fixed value.

Increasing laser power (125W-225W) results in lower G and R values by 12.2% and 6.5%, respectively (Fig. 5-14a). In addition, changing scanning speed (from 800 mm/s to 1200 mm/s) shows an increase in G and R by 39.7% and 37.3%, respectively (Fig. 5-14b). It is shown that G and R criteria are highly dependent on the scanning speed parameter while changing laser power has a minor effect on the G and R variations.

Fig. 5-14c and Fig. 5-14d demonstrate the effect of process parameters on G.R and G/R variables. At a fixed scanning speed, increasing laser power causes a lower G.R (18.2%) and G/R (5.7%). On the other hand, at a fixed laser power, an increase in scanning speed results in higher G.R (92.8%) and G/R (1.2%).

Since a similar trend in R and G values is observed (Fig. 5-14a and Fig. 5-14b), a constructive effect and a destructive effect are expected in G.R and G/R combined parameters, respectively. As a result, the G.R variation seems to be significant when it is compared to the G/R variation. It is noteworthy to mention that once again the scanning speed has a stronger influence on G.R values (92.8%) compared to laser power (18.2%). This is due to the simultaneous effect of scanning speed on G and R variables.

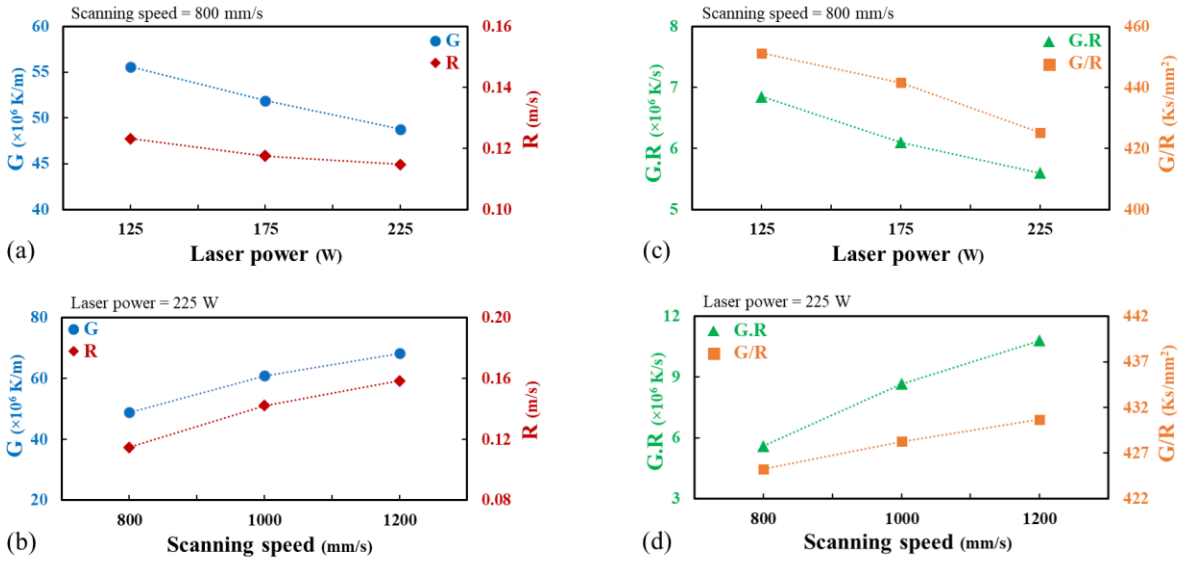

Figure 5-14: Simulated G and R at (a) fixed scanning speed and varied laser powers, and at (b) fixed laser power and different scanning speed. G.R and G/R at (c) fixed scanning speed and varied laser powers, and at (d) fixed laser power and different scanning speed. These thermal variables were measured at the beginning of solidification, from the bottom of the melt pools.

The aforementioned analysis can be utilized in microstructure prediction when a desired mechanical or physical property is aimed to be optimized. For example, if an equiaxed grain structure is desired, a low G/R ratio is required to create a columnar to equiaxed transition, when a high laser power and low scanning speed can fulfill such a solidification environment. In addition, if a fine subgrain structure is aimed to reach, a higher G.R (cooling rate) is achievable with a high scanning speed and a low laser power.

5.5 Conclusions

In this study, a new hybrid (triple-cone) heat source model, was developed to simulate the heat distribution and solidification behaviour of LPBF-made Ti-5553. In addition to the melt pool geometry and temperature history, solidification parameters such as temperature gradient and solidification rate were extracted from the developed model. These parameters (G, R, G.R, and G/R) were calculated at the solid/liquid moving boundary of the melt pool, during solidification (from start to finish) and used for microstructure prediction. The simulated results were compared

with various experimental results. According to the integrated numerical and experimental measurements, the main conclusions can be summarized as follows:

1) A new hybrid heat source model was developed, which provides very low modelling error and can predict the melt pool shape and dimensions accurately. The average percentage difference between numerical and experimental results for the melt pool depth was 8.8% and for the melt pool width was 4.5%.

2) Simulation results show a variety of predicted G and R values across the melt pool. The consecutive solidification simulation of the melt pool shows a high-temperature zone at the center of the melt pool, while a low-temperature gradient always appears in the melt pool central region. During the melt pool solidification, the cooling rate (G.R) and the solidification rate along with *z*-direction (from the bottom to the center of the melt pool) decreased from 4.72×10^6 K/s to 1.76×10^6 K/s and increased from 10.5×10^{-2} m/s to 25.9×10^{-2} m/s, respectively. Along with the *y*-direction (from the sides to the center of the melt pool) trend is the same. The cooling rate decreased from 1.97×10^6 K/s to 1.76×10^6 K/s and the solidification rate increased from 4.22×10^{-2} m/s to 25.9×10^{-2} m/s.

3) For a melt pool that has a mixed columnar/equiaxed structure, the probability of nucleation and equiaxed grain formation in the center of the melt pool is higher than in the other regions of the melt pool. The G/R value at the center of the melt pool is about 10% of the G/R at the melt pool boundary.

4) Results reveal that the model is capable of subgrain size prediction when the relationship between the simulated cooling rate and measured PDAS was investigated. The calculated cooling rate based on PDAS measurement was ~1.32×10^6 K/s, while the simulated cooling rate value for the same melt pool and location was ~1.48×10^6 K/s. As a result, the percentage error was around 12 % which indicates that the results are quite comparable.

5) It is observed that a higher energy input reduces G and R values at the bottom of the melt pool when either laser power or scanning speed is set to be a fixed value. Increasing laser power (from 125W to 225W) results in lower G and R values by 12.2% and 6.5%, respectively. In addition, changing the scanning speed (from 1200 mm/s to 800 mm/s) led to a decrease in G and R by 28.9.7% and 27.2%, respectively.

6) The modelled heat flow direction which can stand as the direction of epitaxial grain growth, at the bottom of the melt pool is fully vertical. Moving from the bottom to the side of the melt pool, a tilt towards the center is seen in the simulated heat flow direction.

Chapter 6

6 In-situ Microstructure Control by Laser Post-exposure Treatment during LPBF Process

6.1 Introduction

Laser Powder Bed Fusion (LPBF), the most popular metal Additive Manufacturing (AM) technology, has enabled the fabrication of metallic parts with tailored mechanical properties [1,7,59,143,168]. These properties immensely depend on the microstructural evolution during the LPBF process [169,170]. Hence, modification of the microstructural features during AM has generated a great deal of interest recently [91,98]. An engineered microstructure can provide enhanced anisotropic mechanical and physical behaviours, e.g., higher strength, lower Young's modulus, higher creep resistance, and higher conductivity [27,30,97,171,172].

The characteristics of the microstructure can be attributed to the LPBF process parameters, particularly laser power (P), scanning speed (v), scanning strategy, and interlayer rotation giving rise to different thermal histories and solidification conditions [13,14,173]. Therefore, achieving the desired microstructure necessitates correlating the process parameters with solidification parameters such as temperature gradient, solidification rate, heat flow direction, and melt pool geometry [95,102,103,120,129,169]. Suzuki et al. [95] investigated the microstructure of LPBF-made AlSi12 specimens under various laser powers and scanning speeds and found that the higher laser power and lower scanning speed led to the formation of coarser grains and higher volume fraction of <001> oriented grains. Ishimoto et al. [97] evaluated the microstructure of a beta-type titanium alloy manufactured by the stripe scanning strategy without rotation (X-scan), and with a rotation of 90° between the layers (XY-scan). They inferred that the microstructure obtained from the XY-scan strategy resulted in anisotropy, with a lower Young's modulus along the build direction of the printed specimens. Other scanning strategies such as stripe and chessboard with 67° random rotation in each layer, along with X-scan and XY-scan, were also investigated by Keshavarzkermani et al. [94]. They proposed that different solidification patterns resulting from variations in scanning strategy can significantly influence the grain size, grain aspect ratio, Taylor factor, and crystallographic orientation of grains, which in turn, affect the mechanical properties

of the LPBF-made Hastelloy X specimens. Attard et al. [91] developed a graded microstructure in additively manufactured Ni-based Inconel 718 superalloy through the manipulation of chessboard strategy parameters, such as island size, shift, and overlap, to achieve a dual microstructure in a fabricated turbine blade. In addition to the mentioned parameters, laser beam shaping has been recently considered as a new approach to modify the microstructure of the printed parts [93,174,175]. Roehling et al. [101] investigated the effect of Gaussian and elliptical laser intensity profiles on the microstructure of the LPBF-made 316 L stainless steel. They found that elliptical beams resulted in a finer equiaxed grain morphology, higher Taylor factor, and improved mechanical properties.

In this research, a novel method is used to control the formation of microstructure during the LPBF process of Ti-5Al-5Mo-5V-3Cr (Ti5553) alloy, which is an alloy of wide application in the aircraft industry [16,36]. This method represents an in-situ heat treatment in which laser post-exposure (PE) scanning plays a key role. Since the remelting of the solidified layers can decrease the nucleation barrier for solidification, it has been hypothesized that a secondary shallow melt pool on top of the initial (main) melt pool may affect grain formation [26]. Employing the secondary laser scanning of much lower energy input, immediately after the initial laser scanning, provides a thin remelting layer on the solidified layer. This thin layer forms a more uniform solidification pattern and causes elongated grains formation, along the building direction. The LPBF-made parts treated with the laser post-exposure are comparable with directionally solidified products, which have enhanced anisotropic properties like good creep resistance [28,29]. It should be mentioned that the current research is the first scientific attempt to control the grain structure in this alloy using in-situ laser treatment during the LPBF process.

6.2 Material and methods

Plasma-atomized Ti-5553 alloy powder (produced by AP&C) was used for printing the specimens. The powder material was spherical in shape, with a D10, D50 and D90 of 22 μm, 35 μm, and 46 μm, respectively. The EOS M290 machine equipped with a 400W Ytterbium continuous fibre laser with a wavelength of 1060 - 1100 nm was employed to fabricate the specimens. The laser spot diameter was 100 μm and the process was carried out under a high-purity argon (purity 99.99%) gas atmosphere.

To examine the microstructure of the specimens, conventional cutting and metallography steps were done followed by etching of the mirror-like surfaces of the polished specimens using Keller's reagent. The Keyence VHX-7000 optical microscope (OM) was used at 6000X magnification to observe the melt pool boundaries at high resolution. Scanning electron microscopy (SEM) and Electron backscatter diffraction (EBSD) analyses were performed by TESCAN VEGA3 SEM equipped with a BRUKER e$^-$Flash^{FS} detector. For the electron microscopy investigations, metallography steps were completed by vibratory polishing in the Buehler VibroMet2 machine for about 5 hours.

6.2.1 Simulation

A single-track scanning was modelled and the commercial software COMSOL Multiphysics® was used to predict the temperature distribution on top of the substrate. For the geometry, a bulk domain of 1000×500×500 μm was considered as the substrate and an extremely fine hexahedron mesh was implemented in that. For a three-dimensional heat transfer, the conservation of energy was used as the governing equation. The convective and the radiative heat loss from the top surface were considered as the boundary conditions and expressed based on Newton's law and the Stefan-Boltzmann law, respectively.

The thermophysical properties of Ti-5553 at room temperature and melting point were assigned to the bulk domain. Thermal conductivity, density, and specific heat values were set to 5 W/m.K (298K) – 29 W/m.K (1923K), 4.3 g/cm^3 (298K) – 3.4 g/cm^3 (1923K), and 0.53 J/g.K (298K) – 0.75 J/g.K (1923K), respectively. The moving surface heat source model with Gaussian distribution can be expressed as:

$$Q_s\,(x,y,t) = \alpha I_0 \exp\left[-2\,\frac{(x-x_c)^2+(y-y_c)^2}{{r_b}^2}\right]$$

$$I_0 = \frac{2P}{\pi r^2} \tag{6-1}$$

where α, I_0, P, r_b, x_c, and y_c are the material absorptivity, the maximum beam intensity, laser power, the radius of the beam, and the positions of the beam center in the x and y directions, respectively [84]. In this study, β was assumed to be constant with a value of 0.5, and r was equal

to the laser spot radius. The numerical modelling was used to mainly help determine the parameters to avoid the melting temperature, as explained in the following section.

6.2.2 First-round fabrication (PE on the top surface)

To perform the first step of the current research, a rectangular block (30×10×5 mm) was designed as the substrate (Fig. 6-1a). Later substrates based on this design were fabricated using the optimized printing parameters, including a laser power of 275 W and a scanning speed of 1000 mm/s. A stripe scanning strategy was applied with a 67° random rotation in each layer, and the layer thickness and hatch distance were 45 µm and 100 µm, respectively. Post-exposure (PE) was applied to the top surface of the substrate, immediately after printing the last layer, where there were no powder particles. The PE scanning was done parallel to the length of the substrates using the stripe strategy (Fig. 6-1a), with a hatch distance of 80 µm.

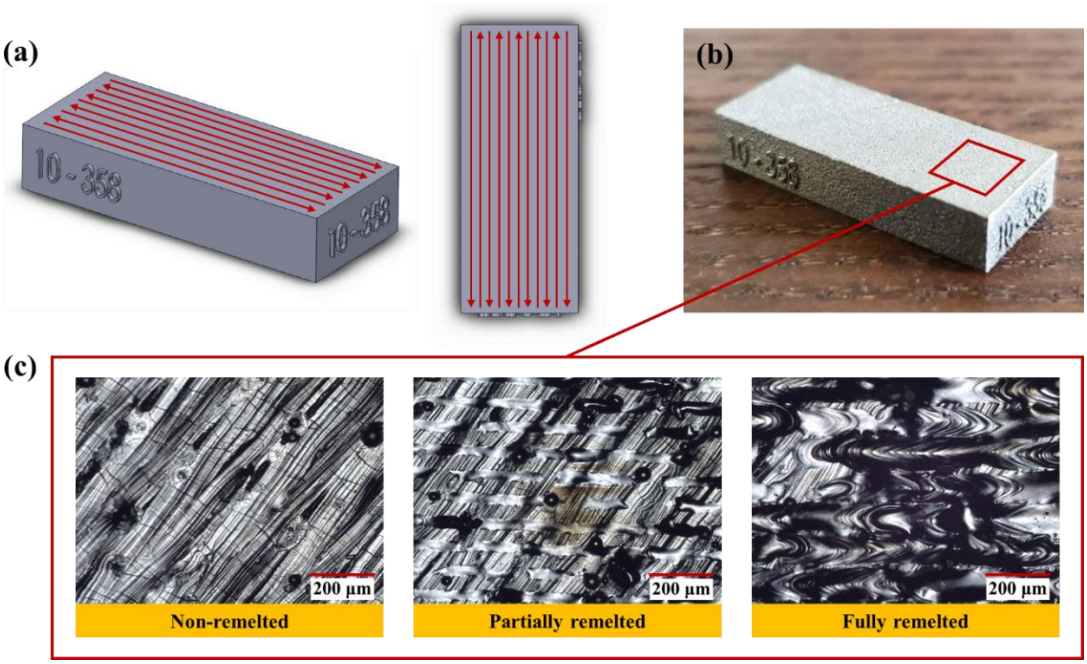

Figure 6-1: (a) Designed PE sample, (b) printed PE sample, and (c) 3 possible effects of PE on the top surface of the samples.

Different PE parameters (a combination of laser power and scanning speed) result in 3 types of effects on the top surface of the substrate. When PE parameters provide low input energy, a partially remelted or non-remelted top surface is obtained, whereas the PE parameters with high

input energy form a fully remelted top surface (Fig. 6-1b and Fig. 6-1c). In the non-remelted samples, the PE treatment may not affect the microstructure of the substrate. However, in the fully remelted samples, the melt pools are too large, and their appearance and influence on the microstructure are similar to the initial melt pools. Therefore, the focus of this research is on the PE parameters which produce partially remelted tracks (Fig. 6-1c).

In the first round, to find a proper window for the PE parameters, 23 sets of process parameters were compared. The variation of scanning speed and laser power is as follows: scanning speeds of 800, 400, 200, 100, and 50 mm/s and laser powers of 1, 5, 10, 15, 20, 25, 30, 35, and 40 W. These process parameters are divided into 6 groups and are listed in Table 6-1.

Table 6-1: Process parameters of the first-round PE samples

#	Scanning speed (mm/s)	Power (W)	VED (J/mm3)	Simulated Max. Temp. [K]	Name
1	800	5	0.139	768	Group 800
2		10	0.278	963	
3		15	0.417	1207	
4		20	0.556	1408	
5		25	0.694	1595	
6		30	0.833	1764	
7		35	0.972	1832	
8		40	1.111	1916	
9	400	5	0.278	779	Group 400
10		10	0.556	1093	
11		15	0.833	1359	
12		20	1.111	1587	
13	200	1	0.111	414	Group 200
14		5	0.556	856	
15		10	1.111	1208	
16		15	1.667	1488	
17	100	1	0.222	467	Group 100
18		5	1.111	915	
19		10	2.222	1288	
20	50	1	0.444	493	Group 50
21		5	2.222	961	
22		10	4.444	1343	
23	0	0	0	0	Reference

Considering the fact that full remelting is not of interest during the PE treatment, numerical modelling was employed to help determine the parameters to avoid the melting temperature (1923 K). Based on the developed model, the simulated maximum temperature for all the PE process parameters is lower than the Ti-5553 melting point (Table 6-1). It should be mentioned that one sample was designed without PE, as a reference sample.

6.2.3 Second-round fabrication (PE on each layer)

As the initial step of the investigation, the effects of PE on the top surface of substrates are assessed. The results and the corresponding discussion will be presented in the following sections. Based on these results, some PE parameters from groups 800, 400, and 200, which provide partial remelting, were selected for next-round printing. These PE parameters are as follows: P=30 W and v=800 mm/s, P=20 W and v=400 mm/s, and P=15 W and v=200 mm/s. In the second round, 5 substrates were printed with the process parameters of the first-round substrates. Of these samples, 1 sample was used as a reference (without PE), 3 were used for test repetition (PE was applied to their top surfaces), and the last sample was chosen to study the effects of PE on each layer during manufacturing.

For the last sample, the PE parameter of P= 20W and v= 400mm/s was immediately applied after the printing of each layer. It should be noted that the PE hatch distance in the second round was set to be lower than 50 μm, and the scanning strategy was changed to XY-scanning (stripe strategy, with 90° rotation in each layer). For mechanical behaviour investigation, uniaxial tensile specimens with five replications were also printed with the same process parameters as the last sample (PE on each layer). The geometry and dimensions of the tensile test specimen can be seen in Fig. 3-1c, in Chapter 3.

6.3 Result and discussion

6.3.1 Remelting and new shallow melt pools

As mentioned in Table 6-1, the PE treatment with laser powers ranging from 5 to 40 W, and scanning speed values ranging from 50 to 800 mm/s were applied to the top surface of the printed substrate. The top surface morphology of the PE samples was investigated through microscopic images. Fig. 2 shows the effect of post-exposure treatment on the top surface of some samples. As

shown in Fig. 6-2a, for group 800, the PE process parameter window achieves the desired partially remelted surface morphology. There is almost no effect on the top surface of the first sample with the lowest input energy (P=5 W), whereas the top surface of the last sample with the highest input energy (P=40 W) is nearly fully remelted. In this group, the PE parameters with moderate input energy (P=20, 25, and 30 W) provided partially remelted tracks. Since partial remelting was assumed as the mode of interest in this research, one of these PE parameters (e.g., P=30 W and v=800 mm/s) could be selected from group 800 for the second-round fabrication.

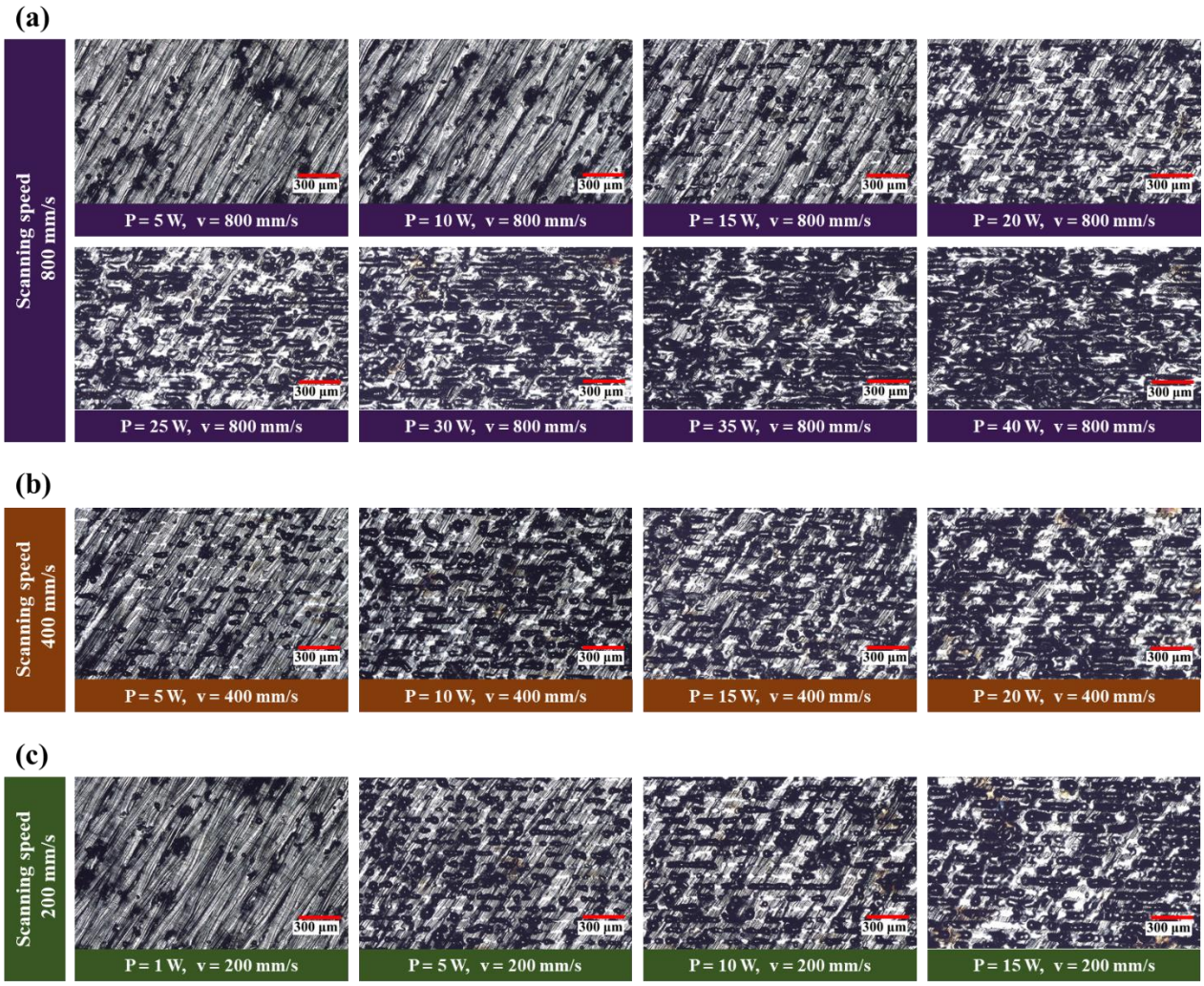

Figure 6-2: Microscopic images of the first-round PE samples (top surface), at different PE parameters. The images show the effect of PE treatment on the top surface of (a) group 800, group 400, and (c) group 200 samples.

Fig. 6-2b illustrates that the lowest laser power (P=5 W) results in some indistinct remelted tracks; however, the other laser powers provide rather clearer partially remelted tracks. Therefore, P=20 W and v=400 mm/s PE parameters were considered potential candidates for the second-round fabrication. In Fig. 6-2c, again there is a range of effects, from almost no remelting to partial remelting. Based on the microscopic images, the P=15 W and v=200 mm/s PE parameter set was selected from group 200 to be used in the second-round fabrication. It should be noted that the remelting condition for groups 100 and 50 was similar to that of the other groups.

In the next step, to study the new remelted tracks and melt pools, all the samples were sectioned and investigated by microscope. Fig. 6-3 shows the micrographs of the cross-section (perpendicular to the PE tracks) from the first-round samples. As shown in Fig. 6-3a, there is no trace of the PE treatment on the top surface of the reference sample. However, in Fig. 6-3b and Fig. 6-3c, the PE melt pools and beads can be seen clearly (marked by a yellow rectangle). The dimensions of these melt pools are significantly smaller than those of the initial melt pools.

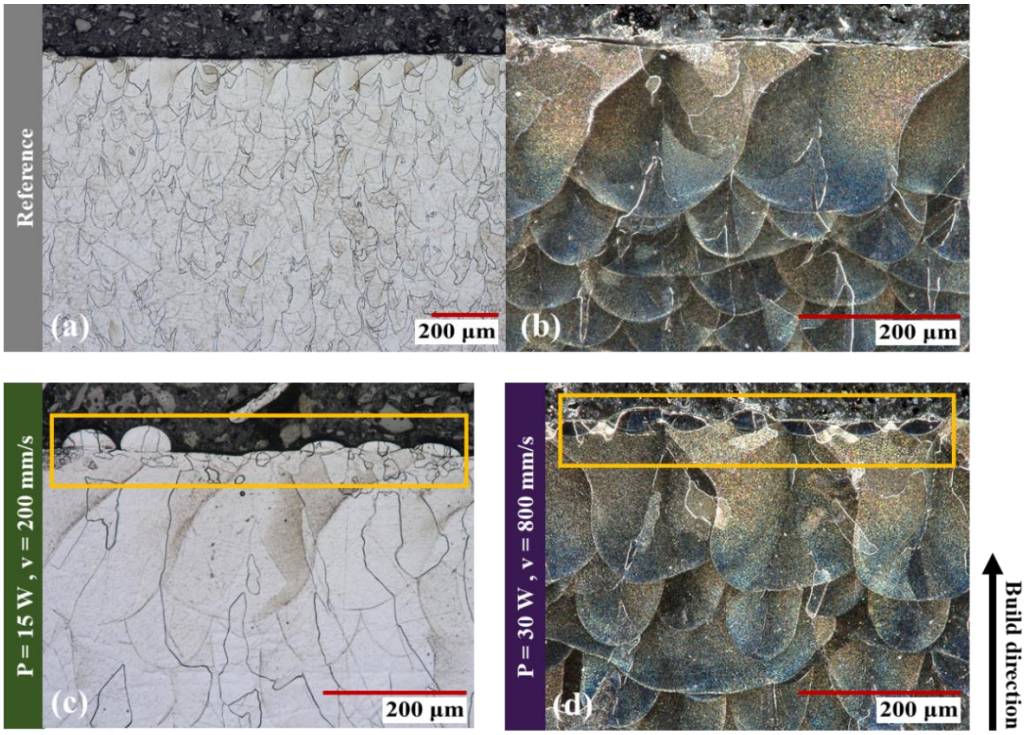

Figure 6-3: Microscopic images of the first-round PE samples (cross-section), at different PE parameters. (a)(b) The reference sample does not have any PE melt pool, but (c)(d) samples with PE on top, have some small melt pools on their surface. For (a) and (c), the full coaxial mode (Observation in the bright field) and for (b) and (d) the full ring mode (Observation in the dark field) of the OM microscope have been used.

Based on the microscopic investigation of the first-round samples, the second-round samples were designed. As mentioned above, P=30 W and v=800 mm/s, P=20 W and v=400 mm/s, and P=15 W and v=200 mm/s, which provided partial remelting for the second-round fabrication. Since the average width of the PE melt pools was about 70 μm, in the second-round fabrication, the PE hatch distance was adjusted to a lower value of 50 μm to ensure complete coverage of the top surface of the last layer. In addition, to have a symmetric and systematic melting and solidification, the scanning strategy was changed to XY-scanning (stripe, with 90° rotation for each layer).

6.3.2 Controlled microstructure

In the second-round fabrication, a PE parameter was applied to each layer during printing to determine the effects of PE treatment on the developed microstructure. To gain a deeper scientific understanding of the effect of PE on microstructure, the results were compared with the microstructure of the reference sample (without PE). Fig. 6-4 shows the EBSD maps and grain size analysis of the reference sample and the PE-treated sample. Moreover, this figure schematically shows the laser track path sequences during the PE treatment were applied immediately after the printing of each layer. The grain sizes of the columnar grains were measured based on the misorientation distribution along the vertical direction of the columnar grains (white dashed line). Since a misorientation larger than 15º can be considered a grain boundary, the length of selected grains in Fig. 6-4a and Fig. 6-4b can be found by the measurement of the distance between each peak > 15º (red dashed line).

Fig. 6-4b illustrates that the PE-treated sample has more uniform and uninterrupted columnar grains with fewer high-angle grain boundaries detected in the vertical growth direction. When the average linear intercept length between high-angle grain boundaries across seven vertical lines is measured for the reference sample, the average grain length is calculated as 321 μm, while for the PE-treated sample, the average intercept length is 845 μm. Furthermore, the grain morphology of the reference sample is more irregular, and the long columnar grains are interrupted by some smaller grains (Fig. 6-4a).

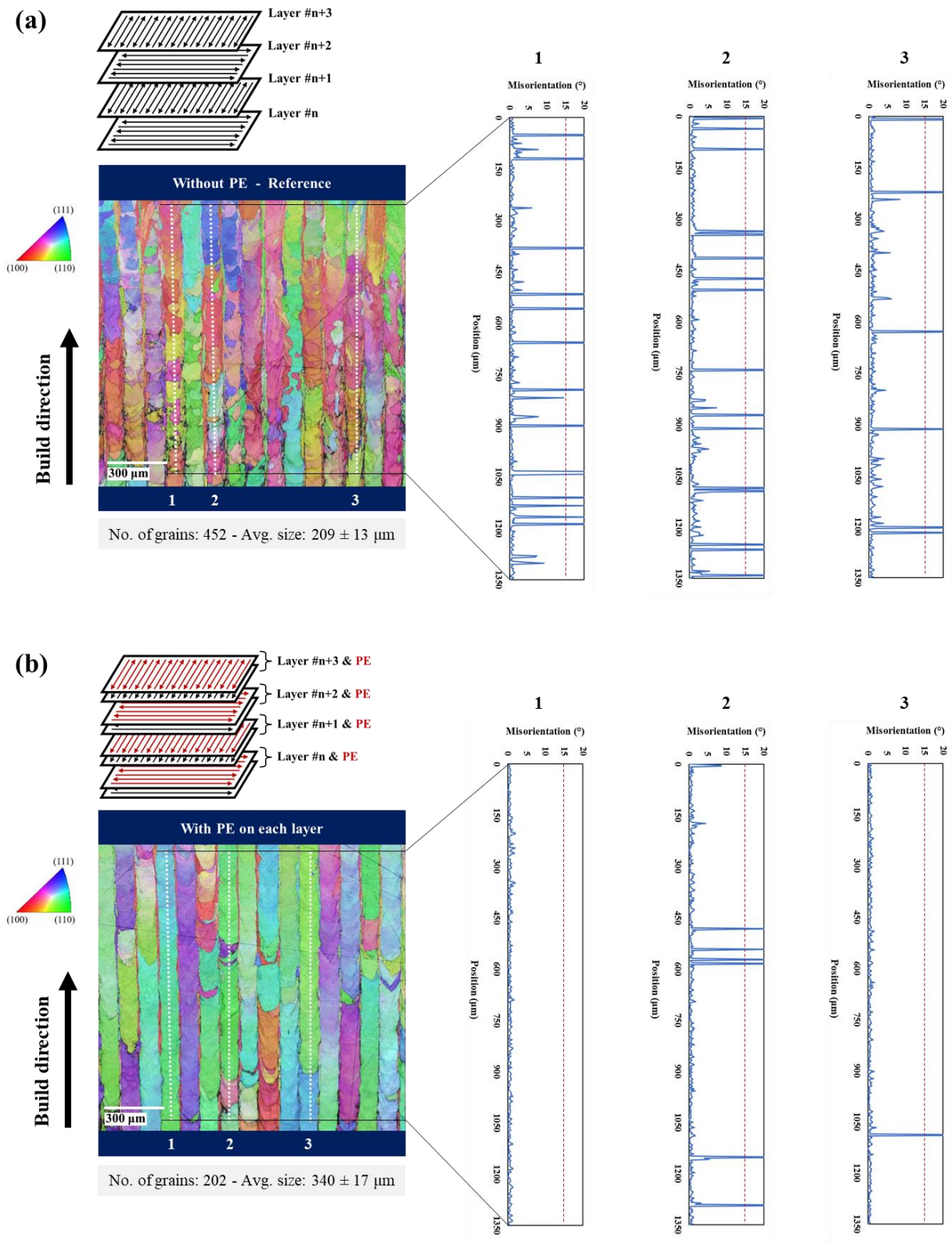

Figure 6-4: EBSD maps and grain size analysis of (a) the reference sample and (b) the PE-treated sample (post-exposure on each layer: P=20 W and v=400 mm/s). The scanning strategy of each one was drawn schematically.

In addition to the mentioned data, the number and the average size of the detected grains are reported in Fig. 6-4. As shown in Fig. 6-4b, for the PE-treated sample, the number of detected grains is 202 μm and the average size of grains is 340 ± 17 μm. In contrast, Fig. 6-4a reveals a higher number of grains (452) and a lower average grain size (209 ± 13 μm) for the reference sample. While in an LPBF-made part with the XY-scanning strategy, the rotation of two consecutive layers breaks the epitaxial grain growth and causes the formation of finer grains, PE treatment results in the growth of longer and uninterrupted grains [176]. A more detailed investigation into the microstructural evolution mechanism(s) and the mechanical behaviour of the alloy is the subject of ongoing research by the authors. In the following section, the near-surface area of these two samples will be investigated for an in-depth understanding of the PE mechanism.

6.3.3 Post-exposure mechanism

To explain the microstructural mechanism behind the PE treatment, the last printed layer was investigated. To this end, the near-surface area of the reference and the PE-treated samples were explored by OM and SEM-EBSD microscopes. Fig. 6-5 illustrates the large initial melt pools and the shallow (secondary) PE melt pools, which are located in the near-surface region of the PE-treated sample.

The direction of the maximum thermal gradient (heat flow direction) reveals the solidification direction and grain growth directions of each of the melted regions [12,71,129,167]. This direction, which is almost normal to the melt pool boundary, is represented with blue arrows in Fig. 6-5b and Fig. 6-5c, schematically. The goblet-like shape of the initial melt pool (Fig. 6-5a) is an indicator of a laser keyhole or near-keyhole melting mode. In this type of melt pool, the grain growth direction in the side part of the melt pool is almost horizontal (orange area in Fig. 6-5c) and the formation of horizontal grains in this near-surface region is expected.

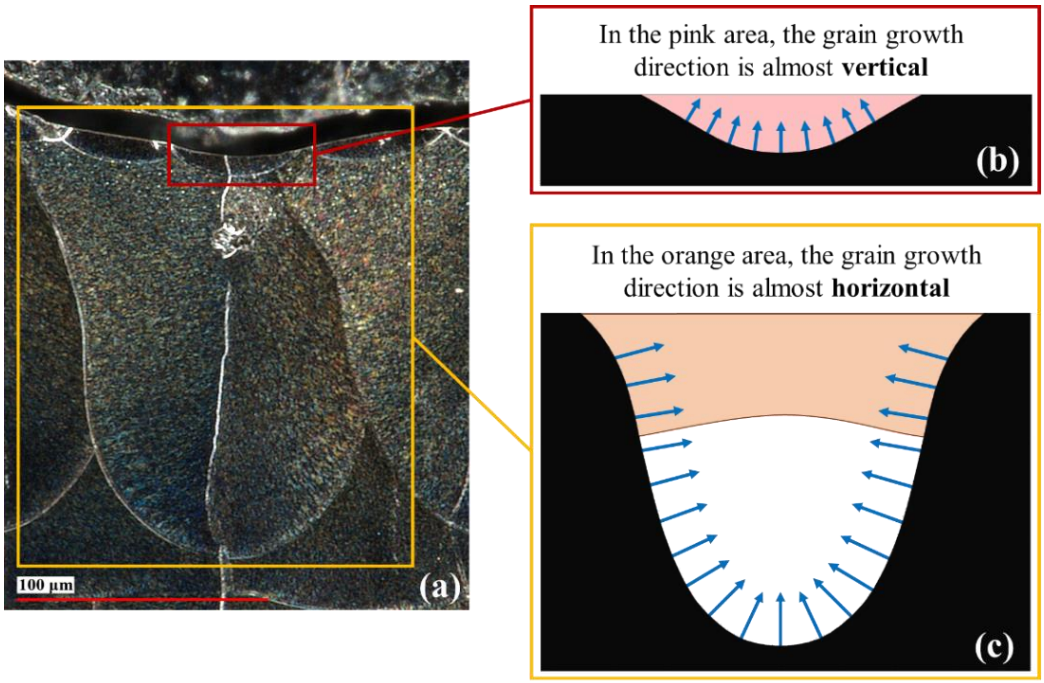

Figure 6-5: (a) Large initial melt pools and shallow PE melt pools, in the microscopic image of the PE-treated sample. (b) The grain growth direction in a shallow (secondary) PE melt pool is almost vertical, while (c) the grain growth direction in the top section of the large initial melt pool is almost horizontal.

The formation of a layer of fine horizontal grains near the top of the initial melt pool can be noted in Fig. 6-6a, where the region within approximately 50 µm of the surface region contains multiple nucleated grains. The size of these near-surface grains is within the range of 30 to 50 µm, which is much finer than the large columnar grains of nearly 300 µm in length throughout the bulk structure. It can be noted that in Fig. 6-6a, the columnar grains are discontinuous, with many low and high-angle boundaries along the vertical build direction.

As discussed previously, the formation of horizontal grains is expected near the surface of the keyhole or near-keyhole melt pools. When these near-surface horizontal grains are not fully remelted during the melting process of the subsequent layer, they can provide additional randomly oriented nucleation sites for grains to disrupt columnar growth. When the PE treatment is applied to the previously solidified layer, the near-surface nucleated grains observed within 50 µm of the surface become fully or partially remelted. However, since the amount of heat is reduced during the PE treatment, the molten layer is much thinner and less of an opportunity available for surface-stimulated nucleation. As a result, the near-surface horizontal grains are restricted to a much lower

layer depth, and much fewer of these surface grains contain high-angle boundaries with differing orientations from the columnar grain below the surface (see Fig. 6-6b).

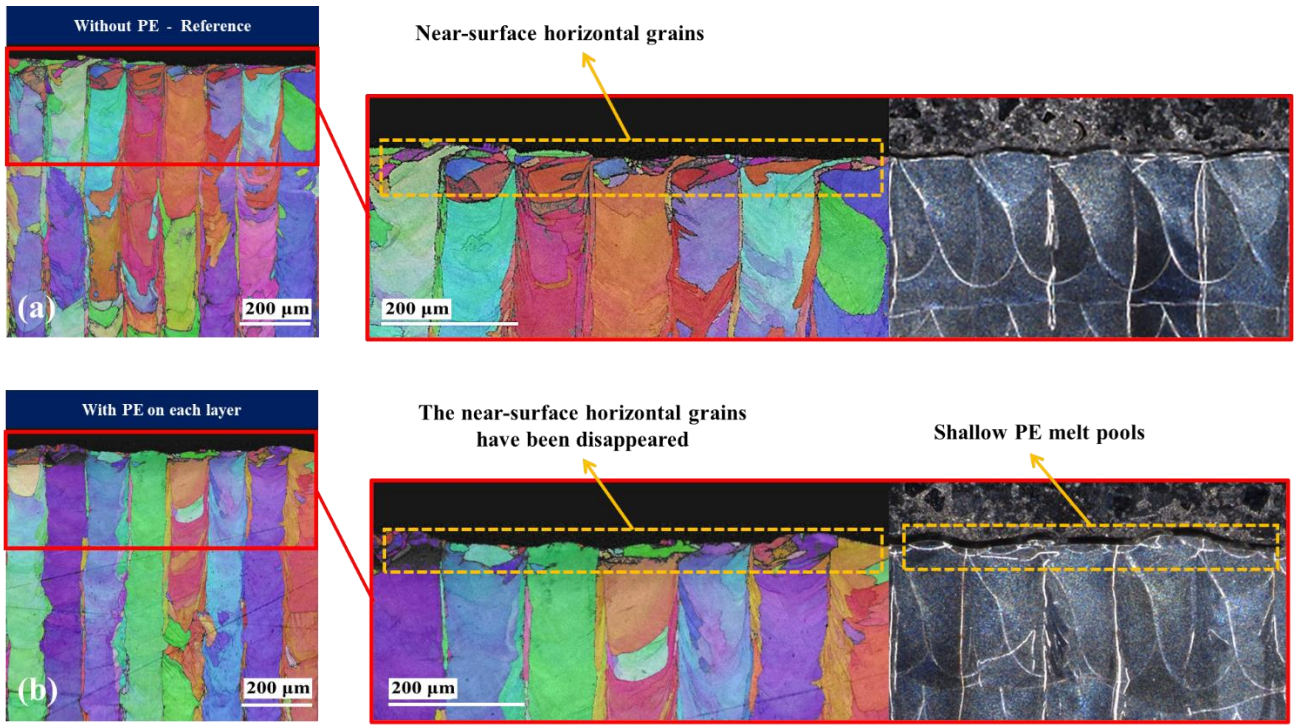

Figure 6-6: EBSD maps and OM images of (a) the reference sample and (b) the post-exposure treated sample. The near-surface equiaxed fine grains of the reference sample disappeared after post-exposure treatment.

It should be noted that the effect of the PE melt pools will play an outstanding role in the solidification history, while the solidified grains in a PE melt pool are remelted via the next layer melting process. In Fig. 6-6, it is shown that the PE melt pools reduce the number of existing grains at the very last solidified layer. This will decrease the number of nucleation sites for the next layer during the epitaxial growth process. As a result, the probability of the existence of new grains in the final microstructure is much less low in with PE condition compared to the regular (without PE) condition. Consequently, the PE process provides a mechanism for suppressing new grain nucleation and may facilitate more uniform growth of elongated and uninterrupted columnar grains, perpendicular to the substrate.

6.4 Conclusions

In this research, the laser post-exposure treatment (a secondary laser scanning with significantly lower energy) has been proposed for the first time as a novel method for the in-situ microstructure control during the LPBF process. The investigation of PE-treated samples reveals that the PE treatment can effectively control the microstructure. The PE treatment creates even and shallow PE melt pools on top of each layer and suppresses the lateral (horizontal) grain growth from the sides of the initial (main) melt pools. The extra heat input of low-energy PE scanning causes a more uniform solidification pattern and creates a uniform and uninterrupted grain structure. The average length of the elongated grains is 845 μm and the grains are arranged in an organized manner, while the grain morphology of the same sample without the PE treatment is more irregular and interrupted, and the average length of the columnar grains is 321 μm. The formed elongated columnar grains by the PE treatment can anisotropically enhance some mechanical properties (e.g., creep and fatigue resistance), similar to what directionally solidified microstructure provides in conventionally manufactured parts.

Chapter 7

7 Conclusions and Future Work

7.1 Conclusions

This work involves LPBF process optimization and simulation for the recently developed Ti-5553 alloy, along with microstructure and properties characterization of the LPBF-made parts. A fundamental study has been done on the melt pool solidification process through the single-track to multi-layer method. The gained knowledge from the investigation of track morphology, melt pool geometry and melt pool microstructure was integrated with the observed microscopic examinations and CT-scan measurement to create a reliable process map for LPBF of Ti-5553. Given that, each set of process parameters within the optimal process window exhibits unique properties and characteristics, supplementary examinations, including microstructure evaluation and mechanical behaviour testing, were also carried out. These observations significantly helped to comprehend the effects of the significant process parameters on the formed microstructure and properties of the printed parts. While the single-track to multi-layer study offers valuable insights into melt pool solidification, it is important to note that certain aspects of the solidification process cannot be measured experimentally.

To achieve an in-depth understanding of melt pool solidification, numerical modelling can provide an efficient solution for studying the correlation between the process parameters and the geometrical and thermal conditions of the LPBF-made melt pool. Hence, a new hybrid heat source model is developed to numerically simulate the LPBF process of Ti-5553 for the first time. This model, with a very low modelling error, can predict melt pool geometry and thermal variables including G and R, at different locations and time steps during melt pool solidification to estimate many important aspects of the microstructure such as grain morphology, subgrain size, and grain growth direction.

The insights acquired through experimental and numerical analyses of melt pool solidification at different process conditions are used to propose laser post-exposure treatment as an inventive approach for in-situ microstructure control during the LPBF process. The post-exposure treatment provides a more uniform solidification pattern and consequently causes elongated grain formation.

The microstructures formed are comparable to the directional solidification (DS) microstructures which can anisotropically enhance some mechanical properties such as strength and creep resistance. This is the first scientific attempt to control the grain structure via in-situ laser post-exposure. The following conclusions can be drawn from the current thesis:

1) Raising the energy input from 23.1 J/mm^3 to 120.4 J/mm^3 leads to a significantly accelerated growth rate in the depth of the molten pool, approximately 2.6 times greater than its width. This occurs because the Gaussian distribution of the laser beam causes the powder particles at the central region of the beam to be more sensitive to energy variations in comparison to those located at the edges.

2) The melt pool depth exhibits a higher level of sensitivity to laser power (53.7%) compared to its sensitivity to scanning speed (37.9%), while the influence of laser power and scanning speed on melt pool width is approximately equal, with values of 46.2% and 48.6%, respectively.

3) Using process conditions near the conduction-keyhole threshold is sometimes preferred over the conduction mode. This transitional mode, with its capacity for facilitating deeper laser penetration, enabling multiple reflections within the keyhole channel, and enhancing energy transfer efficiency. Under this condition, pores may not form or, if they do, they are small and can be eliminated during subsequent layers.

4) In the sample created by high *VED* parameters, which are marked by deeper and hotter melt pools, the α phase content is elevated, leading to greater strength and hardness while reducing ductility.

5) The trade-off for attaining greater strength is a reduction in ductility. In the comparison between the high *VED* (72 J/mm^3) sample and the moderate *VED* (~50 J/mm^3) samples, a decrease in strength of only around 1.5% and 3.5%, respectively, leads to a substantial enhancement in their ductility, with improvements of roughly 45% and 65%, respectively.

6) The differences in properties observed in two samples sharing the same *VED* highlight that *VED* alone is insufficient as a design parameter. It underscores the importance of separately considering the primary process parameters, such as laser power and scanning speed.

7) The simulated thermal variables exhibit that during the solidification of the melt pool, the cooling rate (G.R) decreased from 4.72×10^6 K/s to 1.76×10^6 K/s in the z-direction (from the bottom to the center of the melt pool). In contrast, in the same z-direction, the solidification rate (R) increased from 10.5×10^{-2} m/s to 25.9×10^{-2} m/s. Similarly, in the y-direction (from the sides to the center of the melt pool), the cooling rate decreased from 1.97×10^6 K/s to 1.76×10^6 K/s, while the solidification rate increased from 4.22×10^{-2} m/s to 25.9×10^{-2} m/s.

8) In a melt pool characterized by a mixed columnar/equiaxed structure, the likelihood of nucleation and the formation of equiaxed grains in the center of the melt pool surpasses that in other areas of the melt pool. The G/R value at the center of the melt pool is about 10% of the G/R at the melt pool boundary.

9) The simulated heat flow direction, representing the direction of solidification, is vertical at the bottom of the melt pool. Moving from the bottom to the side of the melt pool, a tilt towards the center is seen in the simulated heat flow direction.

10) During post-exposure treatment, the secondary shallow melt pools on top of the initial (main) melt pools eliminate horizontal near-surface grains and decrease the grain nucleation sites. Furthermore, the grain growth direction in this shallow melt pool is almost vertical, aligned with the elongated grains.

11) The average length of the elongated grains is 845 μm and the grains are arranged in an organized manner, while the grain morphology of the same sample without the PE treatment is more irregular and interrupted, and the average length of the columnar grains is 321 μm.

12) The post-exposure treatment forms elongated columnar grains microstructure, similar to directionally solidified microstructure in conventional manufacturing, which has the potential to provide anisotropy to enhance mechanical and physical properties along selected orientations (build direction).

7.2 Recommendations and future work

The research presented in this thesis was intended to investigate the impact of LPBF processing conditions on the characteristics of printed parts and apply the insights gained to enable customized manufacturing. To this end, after establishing an optimized processing window, the microstructure and properties of LPBF-made components were examined. The experimental and numerical analyses of solidification during the LPBF process were combined with the above-mentioned examinations, and then the laser post-exposure treatment as an in-situ microstructure control method was proposed.

Based on the results and discussions detailed in the preceding sections, the primary objectives of this research have been successfully achieved. However, it is realized that various aspects of the project offer potential for enhancement and further exploration. Hence, some recommended future work has been proposed in this section as follows:

- In the present research, the feasibility of in-situ microstructure control using an innovative method was discussed. The next critical investigation should focus on how the obtained DS-like microstructure affects the mechanical properties of the printed part. It is anticipated that the printed DS-like microstructure will offer consistent strength over a wider temperature range and improved resistance to creep and fatigue, similar to the conventional DS microstructures.

- Given the use of Ni-base alloys in the manufacturing of components exposed to thermo-mechanical stress, such as turbine blades, the investigation of microstructure control in these alloys using the post-exposure treatment method is of utmost importance. Since this method is designed based on melt pool geometry engineering, and the melt pool's

geometrical behaviour in Ni-base alloys closely resembles that of Ti-alloys, the post-exposure treatment should also be effective for Ni-base alloys.

- The new generation of LPBF machines, equipped with multiple lasers or laser beam shaping capabilities, offers enhanced opportunities for controlling microstructures. For example, a larger laser beam diameter with even intensity distribution may result in the formation of thicker elongated grains, and a quad-laser machine can expedite the secondary post-exposure scanning process. Furthermore, with recently developed machines and in-situ supplementary processing, even may be possible to achieve a printed single-crystal.

- Since the heat treatability of Ti-5553 alloy is notably high and the α phase formation is very sensitive to the process energy input (discussed in the section "4.2.2 Tensile strength"), the effect of post-exposure treatment on the α phase formation should be taken into account and investigated with high-tech examination methods like transmission electron microscopy (TEM).

- The primary objectives of modelling in this research have been successfully achieved. Nevertheless, expanding from single-track modelling to multi-layer modelling can yield invaluable insights into the thermal conditions during LPBF of the 3D parts. This modelling approach can be employed in the industry, as it offers a high level of accuracy (in comparison to analytical modelling) and speed (in comparison to numerical modelling involving fluid dynamics).

Letter of Copyright Permission

ELSEVIER LICENSE
TERMS AND CONDITIONS

Jan 29, 2024

This Agreement between Mr. Mahyar Hasanabadi ("You") and Elsevier ("Elsevier") consists of your license details and the terms and conditions provided by Elsevier and Copyright Clearance Center.

License Number	5718320189912
License date	Jan 29, 2024
Licensed Content Publisher	Elsevier
Licensed Content Publication	Materials Science and Engineering: A
Licensed Content Title	Effect of non-lamellar α precipitate morphology on the mechanical properties of Ti5553 parts made by laser powder-bed fusion at high laser scan speeds
Licensed Content Author	Nivas Ramachandiran,Hamed Asgari,Francis Dibia,Roger Eybel,Adrian Gerlich,Ehsan Toyserkani
Licensed Content Date	Apr 28, 2022
Licensed Content Volume	841
Licensed Content Issue	n/a
Licensed Content Pages	1
Start Page	143039
End Page	0
Type of Use	reuse in a thesis/dissertation

ELSEVIER LICENSE
TERMS AND CONDITIONS

Jan 29, 2024

This Agreement between Mr. Mahyar Hasanabadi ("You") and Elsevier ("Elsevier") consists of your license details and the terms and conditions provided by Elsevier and Copyright Clearance Center.

License Number	5718320356258
License date	Jan 29, 2024
Licensed Content Publisher	Elsevier
Licensed Content Publication	Materials & Design
Licensed Content Title	Microstructure and mechanical properties of the near-beta titanium alloy Ti-5553 processed by selective laser melting
Licensed Content Author	H. Schwab,F. Palm,U. Kühn,J. Eckert
Licensed Content Date	Sep 5, 2016
Licensed Content Volume	105
Licensed Content Issue	n/a
Licensed Content Pages	6
Start Page	75
End Page	80
Type of Use	reuse in a thesis/dissertation

SPRINGER NATURE LICENSE TERMS AND CONDITIONS

Jan 29, 2024

This Agreement between Mr. Mahyar Hasanabadi ("You") and Springer Nature ("Springer Nature") consists of your license details and the terms and conditions provided by Springer Nature and Copyright Clearance Center.

License Number	5718270577450
License date	Jan 29, 2024
Licensed Content Publisher	Springer Nature
Licensed Content Publication	The International Journal of Advanced Manufacturing Technology
Licensed Content Title	Laser powder bed fusion of the steels used in the plastic injection mould industry: a review of the influence of processing parameters on the final properties
Licensed Content Author	Ângela Cunha et al
Licensed Content Date	Jul 7, 2022
Type of Use	Thesis/Dissertation
Requestor type	non-commercial (non-profit)
Format	electronic
Portion	figures/tables/illustrations
Number of figures/tables/illustrations	1
Will you be translating?	no
Circulation/distribution	500 - 999
Author of this Springer Nature content	no
Title of new work	Process Optimization, Numerical Modelling, and Microstructure Control in Laser Powder Bed Fusion of Ti-5553 Parts
Institution name	University of Waterloo
Expected presentation date	Mar 2024
Portions	Fig. 3 Schematic diagram of the main processing parameters of the LPBF process (adapted from [7])

ELSEVIER LICENSE
TERMS AND CONDITIONS

Jan 29, 2024

This Agreement between Mr. Mahyar Hasanabadi ("You") and Elsevier ("Elsevier") consists of your license details and the terms and conditions provided by Elsevier and Copyright Clearance Center.

License Number	5718340172472
License date	Jan 29, 2024
Licensed Content Publisher	Elsevier
Licensed Content Publication	Journal of Alloys and Compounds
Licensed Content Title	Effect of microstructure on tensile properties of Ti–5Al–5Mo–5V–3Cr–1Zr alloy
Licensed Content Author	Chaowen Huang,Yongqing Zhao,Shewei Xin,Wei Zhou,Qian Li,Weidong Zeng
Licensed Content Date	Feb 5, 2017
Licensed Content Volume	693
Licensed Content Issue	n/a
Licensed Content Pages	10
Start Page	582
End Page	591
Type of Use	reuse in a thesis/dissertation

CCC Marketplace

Order Number: 1444984
Order Date: 30 Jan 2024

Payment Information

Mahyar Hasanabadi
mahyar.hasanabadi@uwaterloo.ca
Payment method: Invoice

Billing Address:
Mr. Mahyar Hasanabadi
200 University Ave W
Waterloo, ON N2L 3G1
Canada

mahyar.hasanabadi@uwaterloo.ca

Customer Location:
Mr. Mahyar Hasanabadi
200 University Ave W
Waterloo, ON N2L 3G1
Canada

Order Details

1. Titanium : A Technical Guide

Billing Status: Open

Order License ID	1444984-1	**Type of Use**	Republish in a thesis/dissertation
Order detail status	Completed		
ISBN-13	978-1-62708-269-3	**Publisher**	ASM International
		Portion	Image/photo/illustration

0.00 CAD
Republication Permission

LICENSED CONTENT

Publication Title	Titanium : A Technical Guide	**Country**	United States of America
Author/Editor	Donachie, Matthew J., Jr.	**Rightsholder**	ASM International
Date	01/01/2000	**Publication Type**	e-Book
Language	English		

REQUEST DETAILS

Portion Type	Image/photo/illustration	**Distribution**	Worldwide
Number of Images / Photos / Illustrations	2	**Translation**	Original language of publication
Format (select all that apply)	Electronic	**Copies for the Disabled?**	No
		Minor Editing Privileges?	Yes
Who Will Republish the Content?	Academic institution	**Incidental Promotional Use?**	No
		Currency	CAD
Duration of Use	Life of current edition		
Lifetime Unit Quantity	Up to 999		
Rights Requested	Main product		

NEW WORK DETAILS

Title	Process Optimization, Numerical Modelling, and Microstructure Control in Laser Powder Bed Fusion of Ti-5553 Parts	**Institution Name**	University of Waterloo
		Expected Presentation Date	2024-02-29
Instructor Name	Mahyar Hasanabadi		

ELSEVIER LICENSE
TERMS AND CONDITIONS

Jan 29, 2024

This Agreement between Mr. Mahyar Hasanabadi ("You") and Elsevier ("Elsevier") consists of your license details and the terms and conditions provided by Elsevier and Copyright Clearance Center.

License Number	5718311439785
License date	Jan 29, 2024
Licensed Content Publisher	Elsevier
Licensed Content Publication	Materials & Design
Licensed Content Title	Processing of Ti-5553 with improved mechanical properties via an in-situ heat treatment combining selective laser melting and substrate plate heating
Licensed Content Author	Holger Schwab,Matthias Bönisch,Lars Giebeler,Tobias Gustmann,Jürgen Eckert,Uta Kühn
Licensed Content Date	Sep 15, 2017
Licensed Content Volume	130
Licensed Content Issue	n/a
Licensed Content Pages	7
Start Page	83
End Page	89
Type of Use	reuse in a thesis/dissertation

ELSEVIER LICENSE
TERMS AND CONDITIONS

Jan 29, 2024

This Agreement between Mr. Mahyar Hasanabadi ("You") and Elsevier ("Elsevier") consists of your license details and the terms and conditions provided by Elsevier and Copyright Clearance Center.

License Number	5718320719122
License date	Jan 29, 2024
Licensed Content Publisher	Elsevier
Licensed Content Publication	Additive Manufacturing
Licensed Content Title	Melt pool microstructure and morphology from single exposures in laser powder bed fusion of 316L stainless steel
Licensed Content Author	F.L. Vecchiato,H. de Winton,P.A. Hooper,M.R. Wenman
Licensed Content Date	Dec 1, 2020
Licensed Content Volume	36
Licensed Content Issue	n/a
Licensed Content Pages	1
Start Page	101401
End Page	0
Type of Use	reuse in a thesis/dissertation

ELSEVIER LICENSE
TERMS AND CONDITIONS

Jan 29, 2024

This Agreement between Mr. Mahyar Hasanabadi ("You") and Elsevier ("Elsevier") consists of your license details and the terms and conditions provided by Elsevier and Copyright Clearance Center.

License Number	5718320873864
License date	Jan 29, 2024
Licensed Content Publisher	Elsevier
Licensed Content Publication	Additive Manufacturing
Licensed Content Title	A novel heat source model for analysis of melt Pool evolution in selective laser melting process
Licensed Content Author	Kang-Hyun. Lee,Gun Jin Yun
Licensed Content Date	Dec 1, 2020
Licensed Content Volume	36
Licensed Content Issue	n/a
Licensed Content Pages	1
Start Page	101497
End Page	0
Type of Use	reuse in a thesis/dissertation
Portion	figures/tables/illustrations

ELSEVIER LICENSE
TERMS AND CONDITIONS

Feb 21, 2024

This Agreement between Mr. Mahyar Hasanabadi ("You") and Elsevier ("Elsevier") consists of your license details and the terms and conditions provided by Elsevier and Copyright Clearance Center.

License Number	5733871058718
License date	Feb 21, 2024
Licensed Content Publisher	Elsevier
Licensed Content Publication	Additive Manufacturing
Licensed Content Title	Design of laser parameters for selectively laser melted maraging steel based on deposited energy density
Licensed Content Author	Asuka Suzuki,Ryoya Nishida,Naoki Takata,Makoto Kobashi,Masaki Kato
Licensed Content Date	Aug 1, 2019
Licensed Content Volume	28
Licensed Content Issue	n/a
Licensed Content Pages	9
Start Page	160
End Page	168

ELSEVIER LICENSE
TERMS AND CONDITIONS

Jan 29, 2024

This Agreement between Mr. Mahyar Hasanabadi ("You") and Elsevier ("Elsevier") consists of your license details and the terms and conditions provided by Elsevier and Copyright Clearance Center.

License Number	5718321144457
License date	Jan 29, 2024
Licensed Content Publisher	Elsevier
Licensed Content Publication	Materials & Design
Licensed Content Title	Microstructure prediction of selective laser melting AlSi10Mg using finite element analysis
Licensed Content Author	Shiwen Liu,Haihong Zhu,Gangyong Peng,Jie Yin,Xiaoyan Zeng
Licensed Content Date	Mar 15, 2018
Licensed Content Volume	142
Licensed Content Issue	n/a
Licensed Content Pages	10
Start Page	319
End Page	328
Type of Use	reuse in a thesis/dissertation

ELSEVIER LICENSE
TERMS AND CONDITIONS

Jan 29, 2024

This Agreement between Mr. Mahyar Hasanabadi ("You") and Elsevier ("Elsevier") consists of your license details and the terms and conditions provided by Elsevier and Copyright Clearance Center.

License Number	5718320984520
License date	Jan 29, 2024
Licensed Content Publisher	Elsevier
Licensed Content Publication	Computational Materials Science
Licensed Content Title	Probing a novel heat source model and adaptive remeshing technique to simulate laser powder bed fusion with experimental validation
Licensed Content Author	Kajal Khan,Gunther Mohr,Kai Hilgenberg,A. De
Licensed Content Date	Aug 1, 2020
Licensed Content Volume	181
Licensed Content Issue	n/a
Licensed Content Pages	1
Start Page	109752
End Page	0
Type of Use	reuse in a thesis/dissertation

References

[1] E. Toyserkani, D. Sarker, O. Obehi Ibhadode, F. Liravi, P. Russo, K. Taherkhani, Metal Additive Manufacturing, 1st ed., John Wiley & Sons Ltd, New Jersey, 2021.

[2] S. Cooke, K. Ahmadi, S. Willerth, R. Herring, Metal additive manufacturing: Technology, metallurgy and modelling, J. Manuf. Process. 57 (2020) 978–1003. https://doi.org/10.1016/j.jmapro.2020.07.025.

[3] C.Y. Yap, C.K. Chua, Z.L. Dong, Z.H. Liu, D.Q. Zhang, L.E. Loh, S.L. Sing, Review of selective laser melting: Materials and applications, Appl. Phys. Rev. 2 (2015). https://doi.org/10.1063/1.4935926.

[4] H. Schwab, F. Palm, U. Kühn, J. Eckert, Microstructure and mechanical properties of the near-beta titanium alloy Ti-5553 processed by selective laser melting, Mater. Des. 105 (2016) 75–80. https://doi.org/10.1016/j.matdes.2016.04.103.

[5] N. Ramachandiran, H. Asgari, F. Dibia, R. Eybel, A. Gerlich, E. Toyserkani, Effect of non-lamellar α precipitate morphology on the mechanical properties of Ti5553 parts made by laser powder-bed fusion at high laser scan speeds, Mater. Sci. Eng. A. 841 (2022) 143039. https://doi.org/10.1016/j.msea.2022.143039.

[6] C. Peters, M. Leyens, Titanium and Titanium Alloys, Wiley, 2003. https://doi.org/10.1002/3527602119.

[7] T. DebRoy, H.L. Wei, J.S. Zuback, T. Mukherjee, J.W. Elmer, J.O. Milewski, A.M. Beese, A. Wilson-Heid, A. De, W. Zhang, Additive manufacturing of metallic components – Process, structure and properties, Prog. Mater. Sci. 92 (2018) 112–224. https://doi.org/10.1016/j.pmatsci.2017.10.001.

[8] N. Ahmed, I. Barsoum, G. Haidemenopoulos, R.K.A. Al-Rub, Process parameter selection and optimization of laser powder bed fusion for 316L stainless steel: A review, J. Manuf. Process. 75 (2022) 415–434. https://doi.org/10.1016/j.jmapro.2021.12.064.

[9] M. Hasanabadi, A. Keshavarzkermai, H. Asgari, N. Azizi, A. Gerlich, E. Toyserkani, In-situ microstructure control by laser post-exposure treatment during laser powder-bed fusion,

Addit. Manuf. Lett. 4 (2023) 100110. https://doi.org/10.1016/j.addlet.2022.100110.

[10] I. Yadroitsev, A. Gusarov, I. Yadroitsava, I. Smurov, Single track formation in selective laser melting of metal powders, J. Mater. Process. Technol. 210 (2010) 1624–1631. https://doi.org/10.1016/j.jmatprotec.2010.05.010.

[11] Y. Tian, D. Tomus, P. Rometsch, X. Wu, Influences of processing parameters on surface roughness of Hastelloy X produced by selective laser melting, Addit. Manuf. 13 (2017) 103–112. https://doi.org/10.1016/j.addma.2016.10.010.

[12] X. Ding, Y. Koizumi, D. Wei, A. Chiba, Effect of process parameters on melt pool geometry and microstructure development for electron beam melting of IN718: A systematic single bead analysis study, Addit. Manuf. 26 (2019) 215–226. https://doi.org/10.1016/j.addma.2018.12.018.

[13] D. Sun, D. Gu, K. Lin, J. Ma, W. Chen, J. Huang, X. Sun, M. Chu, Selective laser melting of titanium parts: Influence of laser process parameters on macro- and microstructures and tensile property, Powder Technol. 342 (2019) 371–379. https://doi.org/10.1016/j.powtec.2018.09.090.

[14] G. Kasperovich, J. Haubrich, J. Gussone, G. Requena, Correlation between porosity and processing parameters in TiAl6V4 produced by selective laser melting, Mater. Des. 105 (2016) 160–170. https://doi.org/10.1016/j.matdes.2016.05.070.

[15] N.G. Jones, R.J. Dashwood, D. Dye, M. Jackson, Thermomechanical processing of Ti-5Al-5Mo-5V-3Cr, Mater. Sci. Eng. A. 490 (2008) 369–377. https://doi.org/10.1016/j.msea.2008.01.055.

[16] P. Singh, H. Pungotra, N.S. Kalsi, On the characteristics of titanium alloys for the aircraft applications, Mater. Today Proc. 4 (2017) 8971–8982. https://doi.org/10.1016/j.matpr.2017.07.249.

[17] H. Schwab, F. Palm, U. Kühn, J. Eckert, Microstructure and mechanical properties of the near-beta titanium alloy Ti-5553 processed by selective laser melting, Mater. Des. 105 (2016) 75–80. https://doi.org/10.1016/j.matdes.2016.04.103.

[18] S. hang XU, Y. LIU, B. LIU, X. WANG, Z. xing CHEN, Microstructural evolution and mechanical properties of Ti–5Al–5Mo–5V–3Cr alloy by heat treatment with continuous temperature gradient, Trans. Nonferrous Met. Soc. China (English Ed. 28 (2018) 273–281. https://doi.org/10.1016/S1003-6326(18)64660-6.

[19] P. Promoppatum, S.C. Yao, P.C. Pistorius, A.D. Rollett, P.J. Coutts, F. Lia, R. Martukanitz, Numerical modeling and experimental validation of thermal history and microstructure for additive manufacturing of an Inconel 718 product, Prog. Addit. Manuf. 3 (2018) 15–32. https://doi.org/10.1007/s40964-018-0039-1.

[20] P. Promoppatum, S.C. Yao, P.C. Pistorius, A.D. Rollett, A Comprehensive Comparison of the Analytical and Numerical Prediction of the Thermal History and Solidification Microstructure of Inconel 718 Products Made by Laser Powder-Bed Fusion, Engineering. 3 (2017) 685–694. https://doi.org/10.1016/J.ENG.2017.05.023.

[21] G.L. Knapp, N. Raghavan, A. Plotkowski, T. DebRoy, Experiments and simulations on solidification microstructure for Inconel 718 in powder bed fusion electron beam additive manufacturing, Addit. Manuf. 25 (2019) 511–521. https://doi.org/10.1016/j.addma.2018.12.001.

[22] T. Mukherjee, T. DebRoy, Mitigation of lack of fusion defects in powder bed fusion additive manufacturing, J. Manuf. Process. 36 (2018) 442–449. https://doi.org/10.1016/j.jmapro.2018.10.028.

[23] S.I. Shahabad, Z. Zhang, A. Keshavarzkermani, U. Ali, Y. Mahmoodkhani, R. Esmaeilizadeh, A. Bonakdar, E. Toyserkani, Heat source model calibration for thermal analysis of laser powder-bed fusion, Int. J. Adv. Manuf. Technol. 106 (2020) 3367–3379. https://doi.org/10.1007/s00170-019-04908-3.

[24] A.M. Kamara, W. Wang, S. Marimuthu, L. Li, Modelling of the melt pool geometry in the laser deposition of nickel alloys using the anisotropic enhanced thermal conductivity approach, Proc. Inst. Mech. Eng. Part B J. Eng. Manuf. 225 (2011) 87–99. https://doi.org/10.1177/09544054JEM2129.

[25] N. Ramachandiran, H. Asgari, F. Dibia, R. Eybel, A. Keshavarzkermani, A. Gerlich, E.

Toyserkani, Anisotropic tensile behavior of laser powder-bed fusion made Ti5553 parts, Mater. Sci. Eng. A. 865 (2023) 144633. https://doi.org/10.1016/j.msea.2023.144633.

[26] L. Thijs, M.L. Montero Sistiaga, R. Wauthle, Q. Xie, J.P. Kruth, J. Van Humbeeck, Strong morphological and crystallographic texture and resulting yield strength anisotropy in selective laser melted tantalum, Acta Mater. 61 (2013) 4657–4668. https://doi.org/10.1016/j.actamat.2013.04.036.

[27] H.Y. Wan, Z.J. Zhou, C.P. Li, G.F. Chen, G.P. Zhang, Effect of scanning strategy on grain structure and crystallographic texture of Inconel 718 processed by selective laser melting, J. Mater. Sci. Technol. 34 (2018) 1799–1804. https://doi.org/10.1016/j.jmst.2018.02.002.

[28] S. Gu, H. Gao, Z. Wen, H. Pei, Z. Li, Y. Zhao, Z. Yue, Creep characteristics of directionally solidified turbine blades based on the difference in original casting characteristics, J. Alloys Compd. 884 (2021) 161055. https://doi.org/10.1016/j.jallcom.2021.161055.

[29] R.J. Kashinga, L.G. Zhao, V. V. Silberschmidt, F. Farukh, N.C. Barnard, M.T. Whittaker, D. Proprentner, B. Shollock, G. McColvin, Low cycle fatigue of a directionally solidified nickel-based superalloy: Testing, characterisation and modelling, Mater. Sci. Eng. A. 708 (2017) 503–513. https://doi.org/10.1016/j.msea.2017.10.024.

[30] Y. Zhou, X. Zeng, Z. Yang, H. Wu, Effect of crystallographic textures on thermal anisotropy of selective laser melted Cu-2.4Ni-0.7Si alloy, J. Alloys Compd. 743 (2018) 258–261. https://doi.org/10.1016/j.jallcom.2018.01.335.

[31] J.S. Zuback, T. DebRoy, The hardness of additively manufactured alloys, Materials (Basel). 11 (2018). https://doi.org/10.3390/ma11112070.

[32] Â. Cunha, A. Marques, M.R. Silva, F. Bartolomeu, F.S. Silva, M. Gasik, B. Trindade, Ó. Carvalho, Laser powder bed fusion of the steels used in the plastic injection mould industry: a review of the influence of processing parameters on the final properties, Springer London, 2022. https://doi.org/10.1007/s00170-022-09588-0.

[33] A. Gaikwad, R.J. Williams, H. de Winton, B.D. Bevans, Z. Smoqi, P. Rao, P.A. Hooper, Multi phenomena melt pool sensor data fusion for enhanced process monitoring of laser powder bed fusion additive manufacturing, Mater. Des. 221 (2022) 110919.

https://doi.org/10.1016/j.matdes.2022.110919.

[34] B. AlMangour, D. Grzesiak, J.M. Yang, Scanning strategies for texture and anisotropy tailoring during selective laser melting of TiC/316L stainless steel nanocomposites, J. Alloys Compd. 728 (2017) 424–435. https://doi.org/10.1016/j.jallcom.2017.08.022.

[35] J.R. Davis, C.E. Cross, M. Marietta, A. Group, Selection and Weldability of Conventional Titanium Alloys, Welding, Brazing Solder. 6 (1993) 507–523. https://doi.org/10.31399/asm.hb.v06.a0001415.

[36] R.R. Boyer, R.D. Briggs, The use of β titanium alloys in the aerospace industry, J. Mater. Eng. Perform. 14 (2005) 681–685. https://doi.org/10.1361/105994905X75448.

[37] A. Deshpande, P. Manda, C. Vanitha, A.K. Singh, Microstructural Characterization of Metastable Beta Titanium Alloys in Hot Rolled and Solution Treated condition, Mater. Today Proc. 5 (2018) 3657–3663. https://doi.org/10.1016/j.matpr.2017.11.616.

[38] M. Niinomi, Mechanical biocompatibilities of titanium alloys for biomedical applications, J. Mech. Behav. Biomed. Mater. 1 (2008) 30–42. https://doi.org/10.1016/j.jmbbm.2007.07.001.

[39] F.H. Froes, Titanium: Physical Metallurgy, Processing, and Applications, ASM International, 2015.

[40] D. Doraiswamy, S. Ankem, The effect of grain size and stability on ambient temperature tensile and creep deformation in metastable beta titanium alloys, Acta Mater. 51 (2003) 1607–1619. https://doi.org/10.1016/S1359-6454(02)00561-X.

[41] R.P. Kolli, A. Devaraj, A review of metastable beta titanium alloys, Metals (Basel). 8 (2018) 1–41. https://doi.org/10.3390/met8070506.

[42] P.J. Arrazola, A. Garay, L.M. Iriarte, M. Armendia, S. Marya, F. Le Maître, Machinability of titanium alloys (Ti6Al4V and Ti555.3), J. Mater. Process. Technol. 209 (2009) 2223–2230. https://doi.org/10.1016/j.jmatprotec.2008.06.020.

[43] J. Donachie, J. Matthew, Titanium - A Technical Guide (2nd Edition), 2000. https://doi.org/10.31399/asm.tb.ttg2.t61120001.

[44] J.C. Sabol, T. Pasang, W.Z. Misiolek, J.C. Williams, Localized tensile strain distribution and metallurgy of electron beam welded Ti-5Al-5V-5Mo-3Cr titanium alloys, J. Mater. Process. Technol. 212 (2012) 2380–2385. https://doi.org/10.1016/j.jmatprotec.2012.06.023.

[45] C. Zopp, S. Blümer, F. Schubert, L. Kroll, Processing of a metastable titanium alloy (Ti-5553) by selective laser melting, Ain Shams Eng. J. 8 (2017) 475–479. https://doi.org/10.1016/j.asej.2016.11.004.

[46] N. Clément, A. Lenain, P.J. Jacques, Mechanical property optimization via microstructural control of new metastable beta titanium alloys, Jom. 59 (2007) 50–53. https://doi.org/10.1007/s11837-007-0010-y.

[47] J.D. Cotton, R.D. Briggs, R.R. Boyer, S. Tamirisakandala, P. Russo, N. Shchetnikov, J.C. Fanning, State of the Art in Beta Titanium Alloys for Airframe Applications, JOM. 67 (2015) 1281–1303. https://doi.org/10.1007/s11837-015-1442-4.

[48] A. Ghosh, S. Sivaprasad, A. Bhattacharjee, S.K. Kar, Microstructure-fracture toughness correlation in an aircraft structural component alloy Ti-5Al-5V-5Mo-3Cr, Mater. Sci. Eng. A. 568 (2013) 61–67. https://doi.org/10.1016/j.msea.2013.01.017.

[49] S.K. Kar, A. Ghosh, N. Fulzele, A. Bhattacharjee, Quantitative microstructural characterization of a near beta Ti alloy, Ti-5553 under different processing conditions, Mater. Charact. 81 (2013) 37–48. https://doi.org/10.1016/j.matchar.2013.03.016.

[50] R. Panza-Gios, The Effect of Heat Treatment on the Microstructure Evolution and Mechanical Properties of Ti-5Al-5V-5Mo-3Cr, and Its Potential Application in Landing Gears., 2009.

[51] F.H. Froes, Titanium - Physical Metallurgy, Processing and Applications, ASM Int. (2015) 51–74.

[52] A. Dehghan-Manshadi, R.J. Dippenaar, Development of α-phase morphologies during low temperature isothermal heat treatment of a Ti-5Al-5Mo-5V-3Cr alloy, Mater. Sci. Eng. A. 528 (2011) 1833–1839. https://doi.org/10.1016/j.msea.2010.09.061.

[53] C. Huang, Y. Zhao, S. Xin, W. Zhou, Q. Li, W. Zeng, Effect of microstructure on tensile properties of Ti–5Al–5Mo–5V–3Cr–1Zr alloy, J. Alloys Compd. 693 (2017) 582–591. https://doi.org/10.1016/j.jallcom.2016.09.233.

[54] H. Deng, L. Chen, W. Qiu, Z. Zheng, Y. Tang, Z. Hu, Y. Wei, Z. Xia, G. Le, J. Tang, X. Cui, Microstructure and mechanical properties of as-deposited and heat treated Ti–5Al–5Mo–5V–3Cr–1Zr (Ti-55531) alloy fabricated by laser melting deposition, J. Alloys Compd. 810 (2019) 151792. https://doi.org/10.1016/j.jallcom.2019.151792.

[55] H. Schwab, M. Bönisch, L. Giebeler, T. Gustmann, J. Eckert, U. Kühn, Processing of Ti-5553 with improved mechanical properties via an in-situ heat treatment combining selective laser melting and substrate plate heating, Mater. Des. 130 (2017) 83–89. https://doi.org/10.1016/j.matdes.2017.05.010.

[56] M. Sadowski, L. Ladani, W. Brindley, J. Romano, Optimizing quality of additively manufactured Inconel 718 using powder bed laser melting process, Addit. Manuf. 11 (2016) 60–70. https://doi.org/10.1016/j.addma.2016.03.006.

[57] S. Bakhshivash, H. Asgari, P. Russo, C.F. Dibia, M. Ansari, A.P. Gerlich, E. Toyserkani, Printability and microstructural evolution of Ti-5553 alloy fabricated by modulated laser powder bed fusion, Int. J. Adv. Manuf. Technol. 103 (2019) 4399–4409. https://doi.org/10.1007/s00170-019-03847-3.

[58] H. Fayazfar, M. Salarian, A. Rogalsky, D. Sarker, P. Russo, V. Paserin, E. Toyserkani, A critical review of powder-based additive manufacturing of ferrous alloys: Process parameters, microstructure and mechanical properties, Mater. Des. 144 (2018) 98–128. https://doi.org/10.1016/j.matdes.2018.02.018.

[59] A. Keshavarzkermani, E. Marzbanrad, R. Esmaeilizadeh, Y. Mahmoodkhani, U. Ali, P.D. Enrique, N.Y. Zhou, A. Bonakdar, E. Toyserkani, An investigation into the effect of process parameters on melt pool geometry, cell spacing, and grain refinement during laser powder bed fusion, Opt. Laser Technol. 116 (2019) 83–91. https://doi.org/10.1016/j.optlastec.2019.03.012.

[60] L. Thijs, F. Verhaeghe, T. Craeghs, J. Van Humbeeck, J.P. Kruth, A study of the

microstructural evolution during selective laser melting of Ti-6Al-4V, Acta Mater. 58 (2010) 3303–3312. https://doi.org/10.1016/j.actamat.2010.02.004.

[61] N. Read, W. Wang, K. Essa, M.M. Attallah, Selective laser melting of AlSi10Mg alloy: Process optimisation and mechanical properties development, Mater. Des. 65 (2015) 417–424. https://doi.org/10.1016/j.matdes.2014.09.044.

[62] D. Qin, Y. Lu, Q. Liu, L. Zheng, L. Zhou, Transgranular shearing introduced brittlement of Ti-5Al-5V-5Mo-3Cr alloy with full lamellar structure at room temperature, Mater. Sci. Eng. A. 572 (2013) 19–24. https://doi.org/10.1016/j.msea.2013.02.029.

[63] R. Esmaeilizadeh, A. Keshavarzkermani, U. Ali, Y. Mahmoodkhani, B. Behravesh, H. Jahed, A. Bonakdar, E. Toyserkani, Customizing mechanical properties of additively manufactured Hastelloy X parts by adjusting laser scanning speed, J. Alloys Compd. 812 (2020) 152097. https://doi.org/10.1016/j.jallcom.2019.152097.

[64] C. Tenbrock, F.G. Fischer, K. Wissenbach, J.H. Schleifenbaum, P. Wagenblast, W. Meiners, J. Wagner, Influence of keyhole and conduction mode melting for top-hat shaped beam profiles in laser powder bed fusion, J. Mater. Process. Technol. 278 (2020) 116514. https://doi.org/10.1016/j.jmatprotec.2019.116514.

[65] E. Toyserkani, A. Khajepour, S. Corbin, Application of experimental-based modeling to laser cladding, J. Laser Appl. 14 (2002) 165–173. https://doi.org/10.2351/1.1494079.

[66] J. Yang, J. Han, H. Yu, J. Yin, M. Gao, Z. Wang, X. Zeng, Role of molten pool mode on formability, microstructure and mechanical properties of selective laser melted Ti-6Al-4V alloy, Mater. Des. 110 (2016) 558–570. https://doi.org/10.1016/j.matdes.2016.08.036.

[67] J.J.S. Dilip, S. Zhang, C. Teng, K. Zeng, C. Robinson, D. Pal, B. Stucker, Influence of processing parameters on the evolution of melt pool, porosity, and microstructures in Ti-6Al-4V alloy parts fabricated by selective laser melting, Prog. Addit. Manuf. 2 (2017) 157–167. https://doi.org/10.1007/s40964-017-0030-2.

[68] C. Guo, Z. Xu, Y. Zhou, S. Shi, G. Li, H. Lu, Q. Zhu, R.M. Ward, Single-track investigation of IN738LC superalloy fabricated by laser powder bed fusion: Track morphology, bead characteristics and part quality, J. Mater. Process. Technol. 290 (2021) 117000.

https://doi.org/10.1016/j.jmatprotec.2020.117000.

[69] Y. Huang, M.B. Khamesee, E. Toyserkani, A new physics-based model for laser directed energy deposition (powder-fed additive manufacturing): From single-track to multi-track and multi-layer, Opt. Laser Technol. 109 (2019) 584–599. https://doi.org/10.1016/j.optlastec.2018.08.015.

[70] Y. He, M. Zhong, J. Beuth, B. Webler, A study of microstructure and cracking behavior of H13 tool steel produced by laser powder bed fusion using single-tracks, multi-track pads, and 3D cubes, J. Mater. Process. Technol. 286 (2020) 116802. https://doi.org/10.1016/j.jmatprotec.2020.116802.

[71] F.L. Vecchiato, H. de Winton, P.A. Hooper, M.R. Wenman, Melt pool microstructure and morphology from single exposures in laser powder bed fusion of 316L stainless steel, Addit. Manuf. 36 (2020) 101401. https://doi.org/10.1016/j.addma.2020.101401.

[72] S.M. Hashemi, S. Parvizi, H. Baghbanijavid, T. Alvin, L. Tan, M. Nematollahi, A. Ramazani, N.X. Fang, Computational modelling of process – structure – property – performance relationships in metal additive manufacturing : a review, Int. Mater. Rev. 0 (2021) 1–46. https://doi.org/10.1080/09506608.2020.1868889.

[73] Z. Li, S. Yang, B. Liu, W. Liu, Z. Kuai, Y. Nie, Simulation of temperature field and stress field of selective laser melting of multi-layer metal powder, Opt. Laser Technol. 140 (2021) 106782. https://doi.org/10.1016/j.optlastec.2020.106782.

[74] G. Vastola, Q.X. Pei, Y.W. Zhang, Predictive model for porosity in powder-bed fusion additive manufacturing at high beam energy regime, Addit. Manuf. 22 (2018) 817–822. https://doi.org/10.1016/j.addma.2018.05.042.

[75] W. Huang, Y. Zhang, Finite element simulation of thermal behavior in single-track multiple-layers thin wall without-support during selective laser melting, J. Manuf. Process. 42 (2019) 139–148. https://doi.org/10.1016/j.jmapro.2019.04.019.

[76] Y.M. Arısoy, L.E. Criales, T. Özel, Modeling and simulation of thermal field and solidification in laser powder bed fusion of nickel alloy IN625, Opt. Laser Technol. 109 (2019) 278–292. https://doi.org/10.1016/j.optlastec.2018.08.016.

[77] C. Bruna-Rosso, A.G. Demir, B. Previtali, Selective laser melting finite element modeling: Validation with high-speed imaging and lack of fusion defects prediction, Mater. Des. 156 (2018) 143–153. https://doi.org/10.1016/j.matdes.2018.06.037.

[78] W. Ge, J.Y.H. Fuh, S.J. Na, Numerical modelling of keyhole formation in selective laser melting of Ti6Al4V, J. Manuf. Process. 62 (2021) 646–654. https://doi.org/10.1016/j.jmapro.2021.01.005.

[79] M. Bayat, A. Thanki, S. Mohanty, A. Witvrouw, S. Yang, J. Thorborg, N.S. Tiedje, J.H. Hattel, Keyhole-induced porosities in Laser-based Powder Bed Fusion (L-PBF) of Ti6Al4V: High-fidelity modelling and experimental validation, Addit. Manuf. 30 (2019) 100835. https://doi.org/10.1016/j.addma.2019.100835.

[80] S.A. Khairallah, A.T. Anderson, A. Rubenchik, W.E. King, Laser powder-bed fusion additive manufacturing: Physics of complex melt flow and formation mechanisms of pores, spatter, and denudation zones, Acta Mater. 108 (2016) 36–45. https://doi.org/10.1016/j.actamat.2016.02.014.

[81] Z. Zhang, Y. Huang, A. Rani Kasinathan, S. Imani Shahabad, U. Ali, Y. Mahmoodkhani, E. Toyserkani, 3-Dimensional heat transfer modeling for laser powder-bed fusion additive manufacturing with volumetric heat sources based on varied thermal conductivity and absorptivity, Opt. Laser Technol. 109 (2019) 297–312. https://doi.org/10.1016/j.optlastec.2018.08.012.

[82] S. Waqar, K. Guo, J. Sun, FEM analysis of thermal and residual stress profile in selective laser melting of 316L stainless steel, J. Manuf. Process. 66 (2021) 81–100. https://doi.org/10.1016/j.jmapro.2021.03.040.

[83] S. Liu, J. Zhu, H. Zhu, J. Yin, C. Chen, X. Zeng, Effect of the track length and track number on the evolution of the molten pool characteristics of SLMed Al alloy: Numerical and experimental study, Opt. Laser Technol. 123 (2020) 105924. https://doi.org/10.1016/j.optlastec.2019.105924.

[84] K.H. Lee, G.J. Yun, A novel heat source model for analysis of melt Pool evolution in selective laser melting process, Addit. Manuf. 36 (2020) 101497.

https://doi.org/10.1016/j.addma.2020.101497.

[85] E. Kundakcıoğlu, I. Lazoglu, Ö. Poyraz, E. Yasa, N. Cizicioğlu, Thermal and molten pool model in selective laser melting process of Inconel 625, Int. J. Adv. Manuf. Technol. 95 (2018) 3977–3984. https://doi.org/10.1007/s00170-017-1489-1.

[86] S. Liu, H. Zhu, G. Peng, J. Yin, X. Zeng, Microstructure prediction of selective laser melting AlSi10Mg using finite element analysis, Mater. Des. 142 (2018) 319–328. https://doi.org/10.1016/j.matdes.2018.01.022.

[87] Z. Zhang, Y. Huang, A. Rani Kasinathan, S. Imani Shahabad, U. Ali, Y. Mahmoodkhani, E. Toyserkani, 3-Dimensional heat transfer modeling for laser powder-bed fusion additive manufacturing with volumetric heat sources based on varied thermal conductivity and absorptivity, Opt. Laser Technol. 109 (2019) 297–312. https://doi.org/10.1016/j.optlastec.2018.08.012.

[88] K. Khan, G. Mohr, K. Hilgenberg, A. De, Probing a novel heat source model and adaptive remeshing technique to simulate laser powder bed fusion with experimental validation, Comput. Mater. Sci. 181 (2020). https://doi.org/10.1016/j.commatsci.2020.109752.

[89] A. Zakirov, S. Belousov, M. Bogdanova, B. Korneev, A. Stepanov, A. Perepelkina, V. Levchenko, A. Meshkov, B. Potapkin, Predictive modeling of laser and electron beam powder bed fusion additive manufacturing of metals at the mesoscale, Addit. Manuf. 35 (2020) 101236. https://doi.org/10.1016/j.addma.2020.101236.

[90] X. Zhang, B. Mao, L. Mushongera, J. Kundin, Y. Liao, Laser powder bed fusion of titanium aluminides: An investigation on site-specific microstructure evolution mechanism, Mater. Des. 201 (2021) 109501. https://doi.org/10.1016/j.matdes.2021.109501.

[91] B. Attard, S. Cruchley, C. Beetz, M. Megahed, Y.L. Chiu, M.M. Attallah, Microstructural control during laser powder fusion to create graded microstructure Ni-superalloy components, Addit. Manuf. 36 (2020) 101432. https://doi.org/10.1016/j.addma.2020.101432.

[92] O. Andreau, I. Koutiri, P. Peyre, J.D. Penot, N. Saintier, E. Pessard, T. De Terris, C. Dupuy, T. Baudin, Texture control of 316L parts by modulation of the melt pool morphology in

selective laser melting, J. Mater. Process. Technol. 264 (2019) 21–31. https://doi.org/10.1016/j.jmatprotec.2018.08.049.

[93] T.U. Tumkur, T. Voisin, R. Shi, P.J. Depond, T.T. Roehling, S. Wu, M.F. Crumb, J.D. Roehling, G. Guss, S.A. Khairallah, M.J. Matthews, Nondiffractive beam shaping for enhanced optothermal control in metal additive manufacturing, Sci. Adv. 7 (2021) 1–12. https://doi.org/10.1126/sciadv.abg9358.

[94] A. Keshavarzkermani, R. Esmaeilizadeh, U. Ali, P.D. Enrique, Y. Mahmoodkhani, N.Y. Zhou, A. Bonakdar, E. Toyserkani, Controlling mechanical properties of additively manufactured hastelloy X by altering solidification pattern during laser powder-bed fusion, Mater. Sci. Eng. A. 762 (2019) 138081. https://doi.org/10.1016/j.msea.2019.138081.

[95] A. Suzuki, T. Miyasaka, N. Takata, M. Kobashi, M. Kato, Control of microstructural characteristics and mechanical properties of AlSi12 alloy by processing conditions of laser powder bed fusion, Addit. Manuf. 48 (2021) 102383. https://doi.org/10.1016/j.addma.2021.102383.

[96] T. Ishimoto, K. Hagihara, K. Hisamoto, T. Nakano, Stability of crystallographic texture in laser powder bed fusion: Understanding the competition of crystal growth using a single crystalline seed, Addit. Manuf. 43 (2021) 102004. https://doi.org/10.1016/j.addma.2021.102004.

[97] T. Ishimoto, K. Hagihara, K. Hisamoto, S.H. Sun, T. Nakano, Crystallographic texture control of beta-type Ti–15Mo–5Zr–3Al alloy by selective laser melting for the development of novel implants with a biocompatible low Young's modulus, Scr. Mater. 132 (2017) 34–38. https://doi.org/10.1016/j.scriptamat.2016.12.038.

[98] J.J. Marattukalam, D. Karlsson, V. Pacheco, P. Beran, U. Wiklund, U. Jansson, B. Hjörvarsson, M. Sahlberg, The effect of laser scanning strategies on texture, mechanical properties, and site-specific grain orientation in selective laser melted 316L SS, Mater. Des. 193 (2020). https://doi.org/10.1016/j.matdes.2020.108852.

[99] T.T. Roehling, S.S.Q. Wu, S.A. Khairallah, J.D. Roehling, S.S. Soezeri, M.F. Crumb, M.J. Matthews, Modulating laser intensity profile ellipticity for microstructural control during

metal additive manufacturing, Acta Mater. 128 (2017) 197–206. https://doi.org/10.1016/j.actamat.2017.02.025.

[100] R. Shi, S.A. Khairallah, T.T. Roehling, T.W. Heo, J.T. McKeown, M.J. Matthews, Microstructural control in metal laser powder bed fusion additive manufacturing using laser beam shaping strategy, Acta Mater. 184 (2020) 284–305. https://doi.org/10.1016/j.actamat.2019.11.053.

[101] T.T. Roehling, R. Shi, S.A. Khairallah, J.D. Roehling, G.M. Guss, J.T. McKeown, M.J. Matthews, Controlling grain nucleation and morphology by laser beam shaping in metal additive manufacturing, Mater. Des. 195 (2020) 109071. https://doi.org/10.1016/j.matdes.2020.109071.

[102] M. Hasanabadi, A. Shamsipur, H.N. Sani, H. Omidvar, S. Sakhaei, Interfacial microstructure and mechanical properties of tungsten carbide brazed joints using Ag-Cu-Zn + Ni/Mn filler alloy, Trans. Nonferrous Met. Soc. China (English Ed. 27 (2017). https://doi.org/10.1016/S1003-6326(17)60292-9.

[103] M. Hasanabadi, H. Omidvar, A. Shamsipur, Effect of BAg1 Ni-Electroplating on microstructure and properties of WC-Co-brazed joints, Mater. Sci. Technol. (United Kingdom). 33 (2017) 2110–2119. https://doi.org/10.1080/02670836.2017.1352184.

[104] M.J. Matthews, G. Guss, S.A. Khairallah, A.M. Rubenchik, P.J. Depond, W.E. King, Denudation of metal powder layers in laser powder bed fusion processes, Acta Mater. 114 (2016) 33–42. https://doi.org/10.1016/j.actamat.2016.05.017.

[105] K. Mumtaz, N. Hopkinson, Top surface and side roughness of Inconel 625 parts processed using selective laser melting, Rapid Prototyp. J. 15 (2009) 96–103. https://doi.org/10.1108/13552540910943397.

[106] S. Shrestha, K. Chou, A study of transient and steady-state regions from single-track deposition in laser powder bed fusion, J. Manuf. Process. 61 (2021) 226–235. https://doi.org/10.1016/j.jmapro.2020.11.023.

[107] A. Gaikwad, B. Giera, G.M. Guss, J.B. Forien, M.J. Matthews, P. Rao, Heterogeneous sensing and scientific machine learning for quality assurance in laser powder bed fusion –

A single-track study, Addit. Manuf. 36 (2020) 101659. https://doi.org/10.1016/j.addma.2020.101659.

[108] R. Sebastian, S. Catchpole-Smith, M. Simonelli, A. Rushworth, H. Chen, A. Clare, 'Unit cell' type scan strategies for powder bed fusion: The Hilbert fractal, Addit. Manuf. 36 (2020) 101588. https://doi.org/10.1016/j.addma.2020.101588.

[109] W.E. King, H.D. Barth, V.M. Castillo, G.F. Gallegos, J.W. Gibbs, D.E. Hahn, C. Kamath, A.M. Rubenchik, Observation of keyhole-mode laser melting in laser powder-bed fusion additive manufacturing, J. Mater. Process. Technol. 214 (2014) 2915–2925. https://doi.org/10.1016/j.jmatprotec.2014.06.005.

[110] P. Bidare, I. Bitharas, R.M. Ward, M.M. Attallah, A.J. Moore, Fluid and particle dynamics in laser powder bed fusion, Acta Mater. 142 (2018) 107–120. https://doi.org/10.1016/j.actamat.2017.09.051.

[111] Y. Chen, S.J. Clark, C.L.A. Leung, L. Sinclair, S. Marussi, M.P. Olbinado, E. Boller, A. Rack, I. Todd, P.D. Lee, In-situ Synchrotron imaging of keyhole mode multi-layer laser powder bed fusion additive manufacturing, Appl. Mater. Today. 20 (2020) 100650. https://doi.org/10.1016/j.apmt.2020.100650.

[112] W. Ke, X. Bu, J.P. Oliveira, W.G. Xu, Z. Wang, Z. Zeng, Modeling and numerical study of keyhole-induced porosity formation in laser beam oscillating welding of 5A06 aluminum alloy, Opt. Laser Technol. 133 (2021) 106540. https://doi.org/10.1016/j.optlastec.2020.106540.

[113] R. Rai, J.W. Elmer, T.A. Palmer, T. Debroy, Heat transfer and fluid flow during keyhole mode laser welding of tantalum, Ti-6Al-4V, 304L stainless steel and vanadium, J. Phys. D. Appl. Phys. 40 (2007) 5753–5766. https://doi.org/10.1088/0022-3727/40/18/037.

[114] S. Lu, H. Fujii, H. Sugiyama, M. Tanaka, K. Nogi, Weld penetration and Marangoni convection with oxide fluxes in GTA welding, Mater. Trans. 43 (2002) 2926–2931. https://doi.org/10.2320/matertrans.43.2926.

[115] T.N. Le, Y.L. Lo, Effects of sulfur concentration and Marangoni convection on melt-pool formation in transition mode of selective laser melting process, Mater. Des. 179 (2019)

107866. https://doi.org/10.1016/j.matdes.2019.107866.

[116] C. Guo, S. Li, S. Shi, X. Li, X. Hu, Q. Zhu, R.M. Ward, Effect of processing parameters on surface roughness, porosity and cracking of as-built IN738LC parts fabricated by laser powder bed fusion, J. Mater. Process. Technol. 285 (2020) 116788. https://doi.org/10.1016/j.jmatprotec.2020.116788.

[117] H. Salem, L.N. Carter, M.M. Attallah, H.G. Salem, Influence of processing parameters on internal porosity and types of defects formed in Ti6Al4V lattice structure fabricated by selective laser melting, Mater. Sci. Eng. A. 767 (2019) 138387. https://doi.org/10.1016/j.msea.2019.138387.

[118] Y.H. Siao, C. Da Wen, Examination of molten pool with Marangoni flow and evaporation effect by simulation and experiment in selective laser melting, Int. Commun. Heat Mass Transf. 125 (2021) 105325. https://doi.org/10.1016/j.icheatmasstransfer.2021.105325.

[119] R. Rashid, S.H. Masood, D. Ruan, S. Palanisamy, R.A. Rahman Rashid, M. Brandt, Effect of scan strategy on density and metallurgical properties of 17-4PH parts printed by Selective Laser Melting (SLM), J. Mater. Process. Technol. 249 (2017) 502–511. https://doi.org/10.1016/j.jmatprotec.2017.06.023.

[120] H.L. Wei, G.L. Knapp, T. Mukherjee, T. DebRoy, Three-dimensional grain growth during multi-layer printing of a nickel-based alloy Inconel 718, Addit. Manuf. 25 (2019) 448–459. https://doi.org/10.1016/j.addma.2018.11.028.

[121] F. Calignano, Investigation of the accuracy and roughness in the laser powder bed fusion process, Virtual Phys. Prototyp. 13 (2018) 97–104. https://doi.org/10.1080/17452759.2018.1426368.

[122] S. Patel, M. Vlasea, Melting modes in laser powder bed fusion, Materialia. 9 (2020) 100591. https://doi.org/10.1016/j.mtla.2020.100591.

[123] M. Tang, P.C. Pistorius, J.L. Beuth, Prediction of lack-of-fusion porosity for powder bed fusion, Addit. Manuf. 14 (2017) 39–48. https://doi.org/10.1016/j.addma.2016.12.001.

[124] L.L. Parimi, G. Ravi, D. Clark, M.M. Attallah, Microstructural and texture development in

direct laser fabricated IN718, Mater. Charact. 89 (2014) 102–111. https://doi.org/10.1016/j.matchar.2013.12.012.

[125] P.K. Neghlani, SLM additive manufacturing of Alloy 718 Effect of process parameters on microstructure and properties, Master Thesis, Univ. West, Sweden. (2016). https://doi.org/10.13140/RG.2.2.25434.64963.

[126] D. Dai, D. Gu, Effect of metal vaporization behavior on keyhole-mode surface morphology of selective laser melted composites using different protective atmospheres, Appl. Surf. Sci. 355 (2015) 310–319. https://doi.org/10.1016/j.apsusc.2015.07.044.

[127] M. Froend, V. Ventzke, F. Dorn, N. Kashaev, B. Klusemann, J. Enz, Microstructure by design: An approach of grain refinement and isotropy improvement in multi-layer wire-based laser metal deposition, Mater. Sci. Eng. A. 772 (2020) 138635. https://doi.org/10.1016/j.msea.2019.138635.

[128] M.S. Pham, B. Dovgyy, P.A. Hooper, C.M. Gourlay, A. Piglione, The role of side-branching in microstructure development in laser powder-bed fusion, Nat. Commun. 11 (2020) 1–12. https://doi.org/10.1038/s41467-020-14453-3.

[129] M. Garibaldi, I. Ashcroft, M. Simonelli, R. Hague, Metallurgy of high-silicon steel parts produced using Selective Laser Melting, Acta Mater. 110 (2016) 207–216. https://doi.org/10.1016/j.actamat.2016.03.037.

[130] M. Hasanabadi, S. Imani Shahabad, A. Keshavarzkermani, R. Eybel, A. Gerlich, E. Toyserkani, A numerical modelling for laser Powder-bed fusion of Ti-alloy with a hybrid heat Source: An investigation on solidification and microstructure formation, Opt. Laser Technol. 174 (2024) 110647. https://doi.org/10.1016/j.optlastec.2024.110647.

[131] S. Kou, Welding Metallurgy, John Wiley & Sons, Inc., Hoboken, NJ, USA, 2002. https://doi.org/10.1002/0471434027.

[132] A. Basak, S. Das, Epitaxy and Microstructure Evolution in Metal Additive Manufacturing, Annu. Rev. Mater. Res. 46 (2016) 125–149. https://doi.org/10.1146/annurev-matsci-070115-031728.

[133] H. Schwab, M. Bönisch, L. Giebeler, T. Gustmann, J. Eckert, U. Kühn, Processing of Ti-5553 with improved mechanical properties via an in-situ heat treatment combining selective laser melting and substrate plate heating, Mater. Des. 130 (2017) 83–89. https://doi.org/10.1016/j.matdes.2017.05.010.

[134] N. Ramachandiran, H. Asgari, F. Dibia, R. Eybel, W. Muhammad, A. Gerlich, E. Toyserkani, Effects of post heat treatment on microstructure and mechanical properties of Ti5553 parts made by laser powder bed fusion, J. Alloys Compd. 938 (2023) 168616. https://doi.org/10.1016/j.jallcom.2022.168616.

[135] W. Zhu, J. Lei, C. Tan, Q. Sun, W. Chen, L. Xiao, J. Sun, A novel high-strength β-Ti alloy with hierarchical distribution of α-phase: The superior combination of strength and ductility, Mater. Des. 168 (2019) 107640. https://doi.org/10.1016/j.matdes.2019.107640.

[136] M. Sen, S. Suman, T. Banerjee, A. Bhattacharjee, S.K. Kar, Tensile deformation mechanism and failure mode of different microstructures in Ti–5Al–5Mo–5V–3Cr alloy, Mater. Sci. Eng. A. 753 (2019) 156–167. https://doi.org/10.1016/j.msea.2019.03.003.

[137] X. Zhou, X. Liu, D. Zhang, Z. Shen, W. Liu, Balling phenomena in selective laser melted tungsten, J. Mater. Process. Technol. 222 (2015) 33–42. https://doi.org/10.1016/j.jmatprotec.2015.02.032.

[138] C. Li, Y.B. Guo, J.B. Zhao, Interfacial phenomena and characteristics between the deposited material and substrate in selective laser melting Inconel 625, J. Mater. Process. Technol. 243 (2017) 269–281. https://doi.org/10.1016/j.jmatprotec.2016.12.033.

[139] I. Yadroitsev, P. Bertrand, I. Smurov, Parametric analysis of the selective laser melting process, Appl. Surf. Sci. 253 (2007) 8064–8069. https://doi.org/10.1016/j.apsusc.2007.02.088.

[140] T.N. Le, Y.L. Lo, K.Y. Chen, W. Hung, Numerical and experimental investigation into powder entrainment and denudation phenomena in laser powder bed fusion process, Powder Technol. 410 (2022) 117907. https://doi.org/10.1016/j.powtec.2022.117907.

[141] M. Amiri, E.J. Payton, An analytical model for prediction of denudation zone width in laser powder bed fusion additive manufacturing, Addit. Manuf. 48 (2021) 102461.

https://doi.org/10.1016/j.addma.2021.102461.

[142] U. Scipioni Bertoli, A.J. Wolfer, M.J. Matthews, J.P.R. Delplanque, J.M. Schoenung, On the limitations of Volumetric Energy Density as a design parameter for Selective Laser Melting, Mater. Des. 113 (2017) 331–340. https://doi.org/10.1016/j.matdes.2016.10.037.

[143] M. Bayat, S. Mohanty, J.H. Hattel, A systematic investigation of the effects of process parameters on heat and fluid flow and metallurgical conditions during laser-based powder bed fusion of Ti6Al4V alloy, Int. J. Heat Mass Transf. 139 (2019) 213–230. https://doi.org/10.1016/j.ijheatmasstransfer.2019.05.017.

[144] R. Acharya, J.A. Sharon, A. Staroselsky, Prediction of microstructure in laser powder bed fusion process, Acta Mater. 124 (2017) 360–371. https://doi.org/10.1016/j.actamat.2016.11.018.

[145] S.E. Atabay, O. Sanchez-Mata, J.A. Muñiz-Lerma, R. Gauvin, M. Brochu, Microstructure and mechanical properties of rene 41 alloy manufactured by laser powder bed fusion, Mater. Sci. Eng. A. 773 (2020). https://doi.org/10.1016/j.msea.2019.138849.

[146] S. Bakhshivash, Characterization of Ti-5553 parts printed by Selective Laser Melting (SLM), 2018.

[147] B.L. Chua, H.J. Lee, D.G. Ahn, Estimation of Effective Thermal Conductivity of Ti-6Al-4V Powders for a Powder Bed Fusion Process Using Finite Element Analysis, Int. J. Precis. Eng. Manuf. 19 (2018) 257–264. https://doi.org/10.1007/s12541-018-0030-2.

[148] K. Karayagiz, A. Elwany, G. Tapia, B. Franco, L. Johnson, J. Ma, I. Karaman, R. Arróyave, Numerical and experimental analysis of heat distribution in the laser powder bed fusion of Ti-6Al-4V, IISE Trans. 51 (2019) 136–152. https://doi.org/10.1080/24725854.2018.1461964.

[149] P. Promoppatum, A.D. Rollett, Physics-based and phenomenological plasticity models for thermomechanical simulation in laser powder bed fusion additive manufacturing: A comprehensive numerical comparison, Mater. Des. 204 (2021) 109658. https://doi.org/10.1016/j.matdes.2021.109658.

[150] M. Ansari, A. Martinez-Marchese, Y. Huang, E. Toyserkani, A mathematical model of laser directed energy deposition for process mapping and geometry prediction of Ti-5553 single-tracks, Elsevier B.V., 2020. https://doi.org/10.1016/j.mtla.2020.100710.

[151] K. Zyguła, M. Wojtaszek, T. Śleboda, S. Lech, O. Lypchanskyi, G. Korpała, U. Prahl, The Influence of Induction Sintering on Microstructure and Deformation Behavior of Ti-5Al-5Mo-5V-3Cr Alloy, Metall. Mater. Trans. A Phys. Metall. Mater. Sci. 52 (2021). https://doi.org/10.1007/s11661-021-06179-8.

[152] P. Promoppatum, R. Onler, S.C. Yao, Numerical and experimental investigations of micro and macro characteristics of direct metal laser sintered Ti-6Al-4V products, J. Mater. Process. Technol. 240 (2017) 262–273. https://doi.org/10.1016/j.jmatprotec.2016.10.005.

[153] B. Cheng, S. Shrestha, K. Chou, Stress and deformation evaluations of scanning strategy effect in selective laser melting, Addit. Manuf. 12 (2016) 240–251. https://doi.org/10.1016/j.addma.2016.05.007.

[154] S. Imani, U. Ali, Z. Zhang, A. Keshavarzkermani, R. Esmaeilizadeh, A. Bonakdar, E. Toyserkani, On the effect of thin-wall thickness on melt pool dimensions in laser powder-bed fusion of Hastelloy X : Numerical modeling and experimental validation, J. Manuf. Process. 75 (2022) 435–449. https://doi.org/10.1016/j.jmapro.2022.01.029.

[155] Z.D. Zhang, S. Imani Shahabad, O. Ibhadode, C.F. Dibia, A. Bonakdar, E. Toyserkani, 3-Dimensional heat transfer modeling for laser powder bed fusion additive manufacturing using parallel computing and adaptive mesh, Opt. Laser Technol. 158 (2023) 108839. https://doi.org/10.1016/j.optlastec.2022.108839.

[156] F. Farrokhi, B. Endelt, M. Kristiansen, A numerical model for full and partial penetration hybrid laser welding of thick-section steels, Opt. Laser Technol. 111 (2019) 671–686. https://doi.org/10.1016/j.optlastec.2018.08.059.

[157] P. Petrov, M. Tongov, Numerical modelling of heat source during electron beam welding, Vacuum. 171 (2020) 108991. https://doi.org/10.1016/j.vacuum.2019.108991.

[158] R.W. McVey, R.M. Melnychuk, J.A. Todd, R.P. Martukanitz, Absorption of laser irradiation in a porous powder layer, J. Laser Appl. 19 (2007) 214–224.

https://doi.org/10.2351/1.2756854.

[159] J. Zhang, D. Gu, Y. Yang, H. Zhang, H. Chen, D. Dai, K. Lin, Influence of Particle Size on Laser Absorption and Scanning Track Formation Mechanisms of Pure Tungsten Powder During Selective Laser Melting, Engineering. 5 (2019) 736–745. https://doi.org/10.1016/j.eng.2019.07.003.

[160] C.D. Boley, S.C. Mitchell, A.M. Rubenchik, S.S.Q. Wu, Metal powder absorptivity: modeling and experiment, Appl. Opt. 55 (2016) 6496. https://doi.org/10.1364/ao.55.006496.

[161] C.D. Boley, S.A. Khairallah, A.M. Rubenchik, Calculation of laser absorption by metal powders in additive manufacturing, Appl. Opt. 54 (2015) 507–517. https://doi.org/10.1201/9781315119106.

[162] A. Suzuki, R. Nishida, N. Takata, M. Kobashi, M. Kato, Design of laser parameters for selectively laser melted maraging steel based on deposited energy density, Addit. Manuf. 28 (2019) 160–168. https://doi.org/10.1016/j.addma.2019.04.018.

[163] P.. Kobryn, S.. Semiatin, Microstructure and texture evolution during solidification processing of Ti–6Al–4V, J. Mater. Process. Technol. 135 (2003) 330–339. https://doi.org/10.1016/S0924-0136(02)00865-8.

[164] H.L. Wei, J.W. Elmer, T. Debroy, Origin of grain orientation during solidification of an aluminum alloy, Acta Mater. 115 (2016) 123–131. https://doi.org/10.1016/j.actamat.2016.05.057.

[165] D. SARTOR, The Relationship Between Secondary Dendrite Arm Spacing and Cooling Rate for Titanium Alloys, THE UNIVERSITY OF QUEENSLAND, 2018.

[166] N.J. Harrison, I. Todd, K. Mumtaz, Reduction of micro-cracking in nickel superalloys processed by Selective Laser Melting: A fundamental alloy design approach, Acta Mater. 94 (2015) 59–68. https://doi.org/10.1016/j.actamat.2015.04.035.

[167] Y. Tian, J.A. Muñiz-Lerma, M. Brochu, Nickel-based superalloy microstructure obtained by pulsed laser powder bed fusion, Mater. Charact. 131 (2017) 306–315.

https://doi.org/10.1016/j.matchar.2017.07.024.

[168] F. Rivalta, L. Ceschini, A.E.W. Jarfors, R. Stolt, Effect of scanning strategy in the SLM process of 18Ni300 maraging steel, Mater. Des. (2021) 109608. https://doi.org/10.1016/j.matdes.2021.109608.

[169] H.L. Wei, J.W. Elmer, T. DebRoy, Three-dimensional modeling of grain structure evolution during welding of an aluminum alloy, Acta Mater. 126 (2017) 413–425. https://doi.org/10.1016/j.actamat.2016.12.073.

[170] W.J. Sames, F.A. List, S. Pannala, R.R. Dehoff, S.S. Babu, The metallurgy and processing science of metal additive manufacturing, Int. Mater. Rev. 61 (2016) 315–360. https://doi.org/10.1080/09506608.2015.1116649.

[171] S. Sanchez, C.J. Hyde, A.T. Clare, I. Ashcroft, G.A. Ravi, Multi laser scan strategies for enhancing creep performance in LPBF, 41 (2021). https://doi.org/10.1016/j.addma.2021.101948.

[172] S.H. Sun, T. Ishimoto, K. Hagihara, Y. Tsutsumi, T. Hanawa, T. Nakano, Excellent mechanical and corrosion properties of austenitic stainless steel with a unique crystallographic lamellar microstructure via selective laser melting, Scr. Mater. 159 (2019) 89–93. https://doi.org/10.1016/j.scriptamat.2018.09.017.

[173] X. Liang, W. Dong, Q. Chen, A.C. To, On incorporating scanning strategy effects into the modified inherent strain modeling framework for laser powder bed fusion, Addit. Manuf. 37 (2021) 101648. https://doi.org/10.1016/j.addma.2020.101648.

[174] R. Shi, S.A. Khairallah, T.T. Roehling, T.W. Heo, J.T. McKeown, M.J. Matthews, Microstructural control in metal laser powder bed fusion additive manufacturing using laser beam shaping strategy, Acta Mater. 184 (2020) 284–305. https://doi.org/10.1016/j.actamat.2019.11.053.

[175] S.N. Grigoriev, A. V. Gusarov, A.S. Metel, T. V. Tarasova, M.A. Volosova, A.A. Okunkova, A.S. Gusev, Beam Shaping in Laser Powder Bed Fusion: Péclet Number and Dynamic Simulation, Metals (Basel). 12 (2022). https://doi.org/10.3390/met12050722.

[176] Y. Song, Q. Sun, K. Guo, X. Wang, J. Liu, J. Sun, Effect of scanning strategies on the microstructure and mechanical behavior of 316L stainless steel fabricated by selective laser melting, Mater. Sci. Eng. A. 793 (2020) 139879. https://doi.org/10.1016/j.msea.2020.139879.